

ELEMENTARY PARTICLES AND PLASMA IN THE FIRST
HOUR OF THE EARLY UNIVERSE

by

Cheng Tao Yang

Copyright © Cheng Tao Yang 2023

A Dissertation Submitted to the Faculty of the

DEPARTMENT OF PHYSICS

In Partial Fulfillment of the Requirements
For the Degree of

DOCTOR OF PHILOSOPHY

In the Graduate College

THE UNIVERSITY OF ARIZONA

2023

THE UNIVERSITY OF ARIZONA
GRADUATE COLLEGE

As members of the Dissertation Committee, we certify that we have read the dissertation prepared by Cheng Tao Yang, titled Elementary Particles and Plasma in the First Hour of the Early Universe and recommend that it be accepted as fulfilling the dissertation requirement for the Degree of Doctor of Philosophy.

Date: October 20th, 2023

Johann Rafelski

Date: October 20th, 2023

Shufang Su

Date: October 20th, 2023

Sean P Fleming

Date: October 20th, 2023

Shufeng Zhang

Date: October 20th, 2023

Erich W Varnes

Date: October 20th, 2023

Final approval and acceptance of this dissertation is contingent upon the candidate's submission of the final copies of the dissertation to the Graduate College.

I hereby certify that I have read this dissertation prepared under my direction and recommend that it be accepted as fulfilling the dissertation requirement.

Date: October 20th, 2023

Dissertation Director: Johann Rafelski

ACKNOWLEDGEMENTS

I would like to thank my adviser and mentor, Professor Johann Rafelski for his patience, encouragement, and dedication in helping me achieve this goal. This dissertation could not have happened without his great insight into so many areas of physics and kindly support. He stands as a remarkable role model in the science and life. His passion and tireless dedication to the field of physics, unwavering optimism, and professional working attitude have left an enduring mark on my approach to research and life attitude. I am grateful for all these invaluable lessons I have learned from him during my journey with him in Arizona. My gratitude also goes to his wife, Victoria Grossack, for hosting many memorable group meetings at their house throughout the years.

I would like to extend my thanks to the research colleagues and close collaborators in Prof. Rafelski's group: (in alphabetical order) Stefan Evans, Martin Formanek, Shelbi J Foster, Chris Grayson, Will Price, Andrew Steinmentz for many physics discussions and their friendship. I would like to thank Dr. Jeremiah Birrell for the physics discussions and help when I was in Taiwan and Arizona. I would like to express my gratitude to Rohit Singh for his generous assistance and support during my time as a Teaching Assistant.

I would like to thank my fiends from Taiwan and Tucson for their friendship and company for my life and PhD journey in Tucson (in alphabetical order): Maxwell Cui, Miwa Clucas, Lia Chen, Angelica Escoto, Jingwei Liu, Yang Liu, Yen-Wei Liu, Carl Dean Orfield, Chung-Yi Tasi, Wei-Leong Tee, Bianca Wang. Furthermore, I would like to express my gratitude to my sister and her family, Irene Yang, Jay Lee, and Summer Lee for their generous support and help.

Finally, I would like to express my thanks to my thesis committee for kindly accepting to take part, for reading this dissertation, and for providing me with helpful advice for improving its contents.

DEDICATION

*I dedicate this work to my parents for their invaluable support and encouragement,
which sustained me through the highs and lows of my journey.*

TABLE OF CONTENTS

LIST OF FIGURES	7
LIST OF TABLES	12
LIST OF PUBLICATIONS AND AUTHOR CONTRIBUTIONS	13
ABSTRACT	17
CHAPTER 1 Introductory topics: particles and plasma in the Universe . . .	19
1.1 Textbook review: the standard FLRW-Universe model	19
1.2 Approaching abundance equilibrium: Fermi/Bose distribution	21
1.3 Thermodynamics of the Early Universe	25
1.4 Cosmic plasma in early Universe $300 \text{ MeV} > T > 0.02 \text{ MeV}$	31
CHAPTER 2 Heavy quarks in cosmic plasma	34
2.1 Overview of heavy quarks in primordial QGP	34
2.2 Bottom and Charm quark near QGP hadronization	35
2.2.1 Reaction rate for quarks production and decay	37
2.2.2 Bottom quark abundance nonequilibrium	42
CHAPTER 3 Strangeness abundance in cosmic plasma	51
3.1 Chemical equilibrium in the hadronic Universe	51
3.2 Seeking strangeness freeze-out chemical nonequilibrium	55
3.2.1 Strangeness creation/annihilation rate in mesons	58
3.2.2 Strangeness production/ exchange rate in hyperons	62
CHAPTER 4 Neutrinos in cosmic plasma	65
4.1 Matrix element for neutrino coherent/ incoherent scattering	65
4.1.1 Long wavelength limit of neutrino-atom coherent scattering	66
4.1.2 Matrix elements of incoherent neutrino scattering	75
4.2 Neutrinos in the early Universe	79
4.2.1 Overview of neutrino freeze-out in the early Universe	79
4.2.2 Lepton number and effective number of neutrinos	82

TABLE OF CONTENTS – *Continued*

CHAPTER 5	Charged leptons in cosmic plasma	91
5.1	Overview of charge leptons in early Universe	91
5.2	Muon–antimuon in the early Universe	93
5.3	Electron-positron plasma in the early Universe	98
5.3.1	Electron chemical potential in the early Universe	98
5.3.2	Microscope damping rate of electron-positron plasma	101
5.3.3	Magnetization of the electron-positron plasma	105
CHAPTER 6	Outlook: research publications underway	115
6.1	Possibility of bottom-catalyzed low temperature baryogenesis	115
6.2	Population of Higgs in the early Universe	120
6.3	After neutrino freeze-out: Extra neutrinos from microscope processes	122
6.4	The e^\pm plasma relaxation rate: Self-consistence approach	127
CHAPTER 7	Summary and conclusion	132
APPENDIX A	Decomposition of Fermi gas into zero and finite temperature components	135
REFERENCES	141

LIST OF FIGURES

- 1.1 The entropy degrees of freedom as a function of T in the early Universe epoch after hadronization $10^{-2} \text{ MeV} \leq T \leq 150 \text{ MeV}$. When particle species becomes nonrelativistic $T \ll m_i$, the contribution to g_*^s becomes negligible, as a result creating the dependence $g_*^s(T)$. The vertical lines represents the mass of particles: $m_e = 0.511 \text{ MeV}$, $m_\mu = 105.6 \text{ MeV}$, and pion average mass $m_\pi \approx 138 \text{ MeV}$ 27
- 1.2 The time evolution of the early Universe as a function of temperature from $300 \text{ MeV} > T > 0.02 \text{ MeV}$ and different sequence of main events are shown with the temperature/time range in the evolution. 32
- 2.1 The quark number density normalized by entropy density, as a function of temperature in the early Universe with $\Upsilon = 1$. The b -quark mass parameters shown are $m_b = 4.2 \text{ GeV}$ (blue) dotted line, $m_b = 4.7 \text{ GeV}$ (black) solid line, and $m_b = 5.2 \text{ GeV}$ (red) dashed line. For c -quark $m_c = 0.93 \text{ GeV}$ (blue) dotted line, $m_c = 1.04 \text{ GeV}$ (black) solid line, and $m_c = 1.15 \text{ GeV}$ (red) dashed line. 36
- 2.2 Comparison of Hubble time $1/H$, quark lifespan τ_q , and characteristic time for production via quark-gluon pair fusion for (top figure) charm and (bottom figure) bottom quarks as a function of temperature. Both figures end at approximately the hadronization temperature of $T_H \approx 150 \text{ MeV}$. Three different masses $m_b = 4.2 \text{ GeV}$ (blue short dashes), 4.7 GeV , (solid black), 5.2 GeV (red long dashes) for bottom quarks are plotted to account for its decay width. 40
- 2.3 Production and decay characteristic times of bottom quark and the Hubble time $1/H$ within the temperature range of interest $0.3 \text{ GeV} > T > 0.15 \text{ MeV}$. Near the top of figure $1/H$ (brown solid line) and τ_T (brown dashed line); other horizontal lines are bottom-quark (in QGP) weak interaction lifetimes τ_b for the three different masses: $m_b = 4.2 \text{ GeV}$ (blue dotted line), $m_b = 4.7 \text{ GeV}$ (black solid line), $m_b = 5.2 \text{ GeV}$ (red dashed line), and the vacuum lifespan τ_B of the B_c meson (green solid line). The relaxation time for strong interaction bottom production $g + g, q + \bar{q} \rightarrow b + \bar{b}$ is shown with three different bottom masses and same type-color coding as weak interaction decay rate. At bottom of figure the in plasma formation process (dashed lines, purple) $b + c \rightarrow B_c + g$ with cross section range $\sigma = 0.1, 10 \text{ mb}$. 43

LIST OF FIGURES – *Continued*

2.4	The fugacity of free/ bounded bottom quark as a function of temperature in the early Universe for $m_b = 4.2 \text{ GeV}$ (blue), $m_b = 4.7 \text{ GeV}$ (black), and $m_b = 5.2 \text{ GeV}$ (red). The solid lines represent the case bottom quark bound into B_c mesons, and the dashed lines label the case of free bottom quark.	47
2.5	The effective relaxation time τ_{eff} as a function of temperature in the early Universe for bottom mass $m_b = 4.7 \text{ GeV}$. For comparison, we also plot the vacuum lifespan of B_c meson $\tau_{B_c}^{decay}$ (red dashed-line), the relaxation time for bottom production τ_{source}^b (blue dashed-line), Hubble expansion time $1/H$ (brown solid line) and relaxation time for temperature cooling τ_T (brown dashed-line).	48
2.6	The non-stationary fugacity Υ_{st}^{non} as a function of temperature in the Universe for different bottom mass $m_b = 4.2 \text{ GeV}$ (blue), $m_b = 4.7 \text{ GeV}$ (black), and $m_b = 5.2 \text{ GeV}$ (red) for the case bottom quarks bound into B_c mesons.	50
3.1	The chemical potential of baryon μ_B/T and strangeness μ_s/T as a function of temperature $150 \text{ MeV} > T > 10 \text{ MeV}$ in the early Universe; for comparison we show m_N/T with $m_N = 938.92 \text{ MeV}$, the average nucleon mass.	54
3.2	The baryon (blue solid line) and antibaryon (red solid line) number density as a function of temperature in the range $150 \text{ MeV} > T > 5 \text{ MeV}$. The green dashed line is the extrapolated value for baryon density. The temperature $T = 38.2 \text{ MeV}$ (black dashed vertical line) is denoted when the ratio $n_{\bar{B}}/(n_B - n_{\bar{B}}) = 1$ which defines the condition where antibaryons disappear from the Universe.	55
3.3	Ratios of hadronic particle number densities as a function of temperature $150 \text{ MeV} > T > 10 \text{ MeV}$ in the early Universe, with baryon B yields: pions π (brown line), kaons $K(q\bar{s})$ (blue), antibaryon \bar{B} (black), hyperon Y (red) and anti-hyperons \bar{Y} (dashed red). Also shown \bar{K}/Y (purple).	56
3.4	The strangeness abundance changing reactions in the primordial Universe. The red circles show strangeness carrying hadronic particles; red thick lines denote effectively instantaneous reactions. Black thick lines show relatively strong hadronic reactions. The reaction rates required to describe strangeness time evolution are shown in [Rafelski and Yang (2022)].	57

LIST OF FIGURES – *Continued*

3.5	Hadronic relaxation reaction times, see Eq. (3.18), as a function of temperature T , are compared to Hubble time $1/H$ (black solid line). At bottom the horizontal black-dashed line is the natural (vacuum) lifespan of ρ	60
3.6	Thermal reaction rate R per volume and time for important hadronic strangeness production and exchange processes as a function of temperature $150 \text{ MeV} > T > 10 \text{ MeV}$ in the early Universe.	64
4.1	Freeze-out temperatures for electron neutrinos (left) and μ, τ neutrinos (right) for the three types of freeze-out processes adapted from paper [Birrell et al. (2014b)]. Top panels print temperature curves as a function of $\sin^2 \theta_W$ for $\eta = \eta_0$, the vertical dashed line is $\sin^2 \theta_W = 0.23$; bottom panels are printed as a function of relative change in interaction strength η/η_0 obtained for $\sin^2 \theta_W = 0.23$	81
4.2	The free-streaming neutrino chemical potential $ \mu_\nu /T_f$ as a function of the effective number of neutrinos N_ν^{eff} . The solid (blue) line is the exact solution and the (red) dashed line is the approximate solution neglecting the $(\mu_\nu/T_f)^4$ term; the maximum difference in the domain shown is about 2%.	85
4.3	The ratio $B/ L $ between the net baryon number and the net lepton number as a function of N_ν^{eff} : The solid blue line shows $B/ L $. The vertical (red) dotted lines represent the values $3.36 \leq N_\nu^{\text{eff}} \leq 3.62$, which correspond to $1.16 \times 10^{-9} \leq B/ L \leq 1.51 \times 10^{-9}$ (horizontal dashed lines).	88
5.1	We plot the thermal reaction rate per volume for different reactions as a function of temperature. We found that dominant reactions for μ^\pm production are $\gamma + \gamma \rightarrow \mu^+ + \mu^-$ and $e^+ + e^- \rightarrow \mu^+ + \mu^-$, and the total production rate crosses the decay rate of μ^\pm at temperature $T_{\text{disappear}} \approx 4.195 \text{ MeV}$	96
5.2	The density ratio between μ^\pm and baryons as a function of temperature. The density ratio at muon disappearance temperature is about $n_{\mu^\pm}/n_B(T_{\text{disappear}}) \approx 0.911$, and around the temperature $T \approx 4.212 \text{ MeV}$ the density ratio $n_{\mu^\pm}/n_B \approx 1$	97

LIST OF FIGURES – *Continued*

- 5.3 Left axis: The chemical potential of an electron as a function of photon temperature $T = T_\gamma$ with $X_p = 0.878$ and $n_B/n_\gamma = 6.05 \times 10^{-10}$. Right axis: the ratio of electron(positron) number density to baryon density as a function of temperature. The blue solid line is the electron density, the red dashed line is the positron density, and the green dotted line is the number density with $\mu_e = 0$. We found that when electron chemical potential $\mu_e \approx T = 0.02 \text{ MeV}$ the positron density decreases because of the annihilation. 101
- 5.4 The relaxation rate κ as a function of temperature in nonrelativistic electron-positron plasma. For comparison, we show reaction rates for Møller reaction $e^- + e^- \rightarrow e^- + e^-$ (blue line), Bhabha reaction $e^- + e^+ \rightarrow e^- + e^+$ (red line), and inverse Compton scattering $e^- + \gamma \rightarrow e^- + \gamma$ (green line) respectively. It shows that the dominant reactions during BBN are the Møller and Bhabha scatterings between electrons and positrons. The total relaxation rate Eq.(5.39) is shown in the black line. It shows that we have $\kappa = 10 \sim 12 \text{ keV}$ during the BBN temperature range. For comparison, the Debye mass $m_D = \omega_p \sqrt{m_e/T}$ (purple line) is shown as a function of temperature. 104
- 5.5 The chemical potential of electron as a function of temperature in the magnetic field b_0 with $X_p = 0.878$ and $n_B/n_\gamma = 6.05 \times 10^{-10}$. The red dashed line represents the magnetic field $b_0 = 1.1 \times 10^{-11}$ and blue line labels the magnetic field $b_0 = 5.5 \times 10^{-3}$ 111
- 5.6 The magnetization $\bar{\mathcal{M}} = \mathcal{M}/\mathcal{B}_C$, with $g = 2$, of the primordial e^+e^- plasma is plotted as a function of temperature. The lower (solid red) and upper (solid blue) bounds for cosmic magnetic scale b_0 are included. The external magnetic field strength $\mathcal{B}/\mathcal{B}_C$ is also plotted in for lower (dashed red) and upper (dashed blue) bounds. The spin fugacity is set to unity. 113
- 6.1 The density ratio between Higgs and baryon asymmetry as a function of temperature with condition $\Upsilon_H = 1$. It shows that the $n_H = (n_B - n_{\bar{B}})$ at temperature $T = 5.7 \text{ GeV}$ 121
- 6.2 The thermal reaction rate per volume as a function of temperature $2 \text{ MeV} > T > 0.05 \text{ MeV}$. The dominant reaction for the process $\gamma\gamma \rightarrow e^-e^+ \rightarrow \nu\bar{\nu}$ is the $e\bar{e} \rightarrow \nu\bar{\nu}$ and we have $R_{\gamma\rightarrow e\rightarrow\nu} = R_{e\bar{e}\rightarrow\nu\bar{\nu}}$ 123
- 6.3 The temperature ratio $T_\nu/T_{\gamma,e^\pm}$ (blue line), the rate ratio $R_{\nu\bar{\nu}\rightarrow e\bar{e}}/R_{e\bar{e}\rightarrow\nu\bar{\nu}}$ (red line) and $(R_{e\bar{e}\rightarrow\nu\bar{\nu}} - R_{\nu\bar{\nu}\rightarrow e\bar{e}})/R_{e\bar{e}\rightarrow\nu\bar{\nu}}$ (green line) as a function of temperature. It shows that the reaction $\nu\bar{\nu} \rightarrow e\bar{e}$ is small compare to the reaction $e\bar{e} \rightarrow \nu\bar{\nu}$ as temperature cooling down. 125

LIST OF FIGURES – *Continued*

- 6.4 the ratio between n_{extra}/n_{relic} as a function of temperature with different neutrino freezeout temperature T_f . It shows that the higher freezeout temperature T_f the higher number of extra neutrinos can be produced. 126
- 6.5 The relaxation rate $\kappa/2$ (blue line) as a function of temperature in nonrelativistic electron-positron plasma. For comparison, we show the plasma frequency ω_{pl} in the red line. It shows that for $T > 145.5$ MeV, the plasma frequency is larger than the collision rate $w_{pl} > \kappa/2$; for temperature $T < 145.5$ MeV, we have $\kappa/2 > w_{pl}$. For temperature $T < 20.3$ keV, the composition of plasma is changed to electron and proton, which is beyond our current study because of unequal numbers of electrons and positrons. 129
- 6.6 The relaxation rate κ that satisfies Eq.(6.24) as a function of temperature $50 \leq T \leq 86$ keV. It shows that for overdamping plasma, we have $m_\gamma^2 = \kappa^2$, and $\kappa = 1.832$ keV when $T = 86$ keV and $\kappa = 0.350$ keV when $T = 50$ keV. The minor fluctuations are a result of the restricted numerical precision. 130
- A.1 The exact Fermi-distribution (LHS of Eq. (A.1) with solid lines and novel form of Fermi-distribution (RHS of Eq. (A.1)) with dashed lines as a function of energy with different parameters. Top: we compare the RHS and LHS of Eq. (A.1) with different chemical potential: $\tilde{\mu} = 0, \pm 0.1, \pm 0.4 \pm 0.6$ MeV at temperature $T = 0.012$ MeV. Bottom: the Fermi distribution with different temperatures $T = 0.511, 0.0511, 0.012$ MeV for chemical potential $\tilde{\mu} = \pm 0.461$ MeV. . . . 138
- A.2 The zero and finite temperature components of the decomposition here considered for Fermi distribution as a function of energy with chemical potential $\tilde{\mu} = 0.461$ MeV at temperature $T = 0.02$ MeV and $T = 0.2$ MeV. The purple line represents the zero temperature component $f_{T=0}$, and blue and red lines represent the finite temperature components $f_{T \neq 0}$ and $\tilde{f}_{T \neq 0}$ respectively. 139

LIST OF TABLES

3.1	The characteristic strangeness reaction and their freeze-out temperature and temperature width in early Universe.	61
4.1	The coupling constants for neutrino scattering with proton, neutron, and electron.	70
4.2	The coefficients for transition amplitude and scattering probability of ν_e and $\nu_{\mu,\tau}$ coherent elastic scattering off different target atoms. The definition of atomic mass is $A = Z + N$, where Z and N are the number of protons and neutron respectively.	72
4.3	The transition amplitude for different annihilation and production processes. The definition of particle number is given by $1+2 \leftrightarrow 3+4$, where $l, l' = e, \mu, \tau (l \neq l')$	77
4.4	The transition amplitude for different elastic scattering processes. The definition of particle number is given by $1 + 2 \leftrightarrow 3 + 4$, where $l, l' = e, \mu, \tau (l \neq l')$	78

LIST OF PUBLICATIONS AND AUTHOR CONTRIBUTIONS

In the course of satisfying the University of Arizona Department of Physics's requirements for a Ph.D. doctoral dissertation, I listed the following publications and point out my contribution to each work which is described under each item.

- "A Short Survey of Matter-Antimatter Evolution in the Primordial Universe" by [Rafelski et al. (2023)] is a 50 page long review with many novel results describing the role of antimatter in the early universe. I collaborate with Andrew Steinmetz, Jeremiah Birrell, and Johann Rafelski the document creation, providing the numerical results/figures for the paper to help creating one coherent presentation. I acknowledge the help and consultation of Andrew Steinmetz, Jeremiah Birrell, and Johann Rafelski in research and computation.
- "Matter-antimatter origin of cosmic magnetism" by [Steinmetz et al. (2023b)] proposes a model of para-magnetization driven by the large matter-antimatter (electron-positron) content of the early universe. I collaborate with Andrew Steinmetz to carry out the computation , contribute key results and five technical figures for the paper. I acknowledge the help and consultation of Andrew Steinmetz, Martin Formanek, and Johann Rafelski in research and computation.
- "Electron-positron plasma in BBN: Damped-dynamic screening" by [Grayson et al. (2023)] use the linear response theory adapt by C. Grayson to describe the inter nuclear potential in electron/positron plasma. My contribution is the computation of the chemical potential and plasma damping rate which are important properties to implement into relativistic Boltzmann equation and linear response theory. I acknowledge the help and consultation of Christopher Grayson, Martin Formanek, and Johann Rafelski in research and computation.

- "Cosmological strangeness abundance" by [Yang and Rafelski (2022)] investigates the strange particle composition of the expanding early Universe and examine their freeze-out temperatures. I performed all computation, writing, and figure making for the paper. I acknowledge the help and consultation of Johann Rafelski in research, writing and editing.
- "The muon abundance in the primordial Universe" by [Rafelski and Yang (2021)] is a study of the muon abundance and its persistence temperature in early Universe. I performed all computation and writing in preparation of the first draft and approved the final draft before submission. I acknowledge the help and consultation of Johann Rafelski in research, writing and editing.
- "Reactions Governing Strangeness Abundance in Primordial Universe" by [Rafelski and Yang (2022)] is a conference proceeding paper for the 19th International Conference on Strangeness in Quark Matter (SQM 2021). It summarize our earlier work in strangeness reactions. I performed all computation and writing in preparation of the first draft and approved the final draft before submission. I acknowledge the help and consultation of Johann Rafelski in research, writing and editing.
- "Possibility of bottom-catalyzed matter genesis near to primordial QGP hadronization" by [Yang and Rafelski (2020)] is our fist study of the bottom flavor abundance and show the nonequilibrium behavior near to QGP hadronization. I performed all computation and writing in preparation of the paper. I acknowledge the help and consultation of Johann Rafelski in research, writing and editing.
- "Lepton Number and Expansion of the Universe" by [Yang et al. (2018a)] proposes a model of large lepton asymmetry and explore how this large cosmological lepton yield relates to the effective number of (Dirac) neutrinos. I performed all computation and writing in preparation of the paper. I acknowledge the help and consultation of Johann Rafelski in research, writing

and editing.

- "Temperature Dependence of the Neutron Lifespan" by [Yang et al. (2018b)] is a study of neutron lifespan in plasma with Fermi-blocking from electron and neutrino. I performed all computation and writing in preparation of the paper. I acknowledge the help and consultation of Johann Rafelski in research, writing and editing.
- "Strong fields and neutral particle magnetic moment dynamics" by [Formanek et al. (2018)] is an overview of our research group's efforts in studying neutral particle dynamics in electromagnetic fields. My contribution is on the neutrino section. I consulted and helped lead author Martin Formanek, and co-authors Stefan Evans, Andrew Steinmetz, and Johann Rafelski in editing and revising the manuscript.
- "Relic Neutrino Freeze-out: Dependence on Natural Constants" by [Birrell et al. (2014b)] is a study of neutrino freeze-out temperature as a function of standard model parameter and its application on the effective number of (Dirac) neutrinos. My contribution is the calculation of all the neutrino-matter weak interaction matrix elements required for the Boltzmann code. I acknowledge the help and consultation of Jeremiah Birrell and Johann Rafelski in research and computation.
- "Fugacity and Reheating of Primordial Neutrinos" by [Birrell et al. (2013)] is a study of neutrino fugacity as a function of neutrino kinetic freeze-out temperature. My contribution is the calculation of neutrino interaction matrix elements and helping the evaluation of neutrino relaxation time. I acknowledge the help and consultation of Jeremiah Birrell, Johann Rafelski, and Pisin Chen in research and computation.
- "Relic neutrinos: Physically consistent treatment of effective number of neutrinos and neutrino mass" by [Birrell et al. (2014a)] is a model independent study of the neutrino momentum distribution at freeze-out, treating the freeze-out

temperature as a free parameter. I collaborate with Jeremiah Birrell, Johann Rafelski, and Pisin Chen the document creation. I acknowledge the help and consultation of Jeremiah Birrell, Johann Rafelski, and Pisin Chen in research.

ABSTRACT

This work aims to deepen the understanding of the primordial composition of the Universe in the temperature range $300 \text{ MeV} > T > 0.02 \text{ MeV}$. In the following I exploit known properties of elementary particles and apply methods of kinetic theory and statistical physics to advance the understanding of the cosmic plasma. Within the Big Bang model the Universe began as a highly energetic fireball with an immensely high temperature and energy density. Consequently, an ultra-relativistic plasma was generated, exhibiting distinct properties as the Universe expanded and cooled. When the Universe is hot and dense, fundamental particles (such as quarks, leptons, and gauge bosons) play a crucial role in understanding the early Universe. These elementary particles were abundantly present once the temperature dropped below $T = 130 \text{ GeV}$. Their interactions governed the dynamics of the early Universe. Our research focuses on investigation of these fundamental particles during the epoch which transits from primordial quark-gluon degrees of freedom to the era of normal matter plasma (H^+ , He^+ , e^-). Our findings will offer valuable insights into the properties of the early Universe governing the properties of matter surrounding us today.

In chapter 1 the properties of the Universe during the ‘first hour’ are described. I do not discuss diverse ideas about the origin of the Universe or how it emerged in thermal state. I begin with primordial Quark Gluon Plasma (QGP), continue to address the evolution of formed hadrons, of leptons, and the decoupling of neutrinos. I consider as well the stage where the electron-positron plasma is dominant. Most of these results depend on ambient (photon) temperature only. The standard cosmological Friedmann-Lemaitre-Robertson-Walker (FLRW) model of the Universe is also introduced allowing the connection of the magnitude of temperature T to the age of the Universe t and the understanding of the speed of temperature change.

I address in particular bottom and charm quarks near to the QGP transformation to hadrons (hadronization temperature $T_H = 150 \text{ MeV}$) in chapter 2. I examine the

relaxation time for the production and decay of bottom/charm quarks as a function of temperature from $300 \text{ MeV} > T > 150 \text{ MeV}$. Of particular interest to me is that the bottom quarks are not in their chemical equilibrium.

In chapter 3, I examine the strange particle composition of the expanding early Universe in the hadron epoch $150 \text{ MeV} \geq T \geq 10 \text{ MeV}$, then investigate the freeze-out temperature for strangeness-producing by comparing the relevant reaction rates to the Hubble expansion rate and show that strangeness are kept in equilibrium via weak, electromagnetic, and strong interactions in the early Universe until $T \approx 13 \text{ MeV}$.

In chapter 4, the matrix elements for neutrino coherent/incoherent scattering with matter and their application in early Universe are studied in detail. An overview of neutrino freeze-out process in early Universe is presented. After neutrino freeze-out, I examine the relation between the effective number of neutrinos N_ν^{eff} and lepton asymmetry L in the Universe and its impact on Universe expansion.

In chapter 5, I examine the dynamical picture of charged leptons μ^\pm and e^\pm in the early Universe and show that the persistence temperature for μ^\pm in the early Universe is $T = 4.2 \text{ MeV}$, and the e^+ abundance can persist in the early Universe at relatively low value $T \approx 20 \text{ keV}$. Given the dense electron-positron plasma in the early Universe, I study the damping rate and investigate the magnetization process within dense electron-positron plasma in the early Universe.

In chapter 6, I address the ongoing and prospective research projects intended for future publication including: The application of nonequilibrium bottom quark; Population of Higgs in the early Universe; Extra neutrino from microscopic processes after freeze-out; Self-consistent relaxation rate for electron-positron plasma. Finally, we summarize our important results and outlook for future study in chapter 7.

CHAPTER 1

Introductory topics: particles and plasma in the Universe

In this chapter, we will introduce the fundamental concepts in cosmology for us to explore the properties of the Universe during the ‘first hour’. I will first present the standard cosmological Friedmann-Lemaitre-Robertson-Walker (FLRW) model, then introduce the general Fermi/Bose distribution with and its application in the early Universe. Finally I present an overview of Universe evolution from $300 \text{ MeV} > T > 0.02 \text{ MeV}$. The Natural unit $c = \hbar = k_B = 1$ is used throughout the thesis for discussion.

1.1 Textbook review: the standard FLRW-Universe model

The Friedmann-Lemaitre-Robertson-Walker (FLRW) Universe is a theoretical model used widely to describe the cosmological evolution of the Universe. It is based on the cosmological principles which assumes homogeneity and isotropy of the Universe on large scales. In general, the FLRW metric can be written as

$$ds^2 = c^2 dt^2 - a^2(t) \left[\frac{dr^2}{1 - kr^2} + r^2(d\theta^2 + \sin^2 \theta d\phi^2) \right]. \quad (1.1)$$

The metric is characterized by the scale factor $a(t)$ which measures the size of the Universe as a function of time t . The geometric parameter k identifies the Gaussian geometry of the spatial hyper-surfaces defined by co-moving observers. The metrics are qualitatively different depending on the value of k . We have $k = 1$ which correspond to the closed Universe, $k = 0$ correspond to flat Universe, and $k = -1$ for open geometries of the Universe. Current observation of cosmic microwave background (CMB) anisotropy preferred value $k = 0$ [Ade et al. (2014, 2016); Aghanim et al. (2020a)].

The cosmological equations that describe the evolution of the Universe are derived from the Einstein equations. In general, the Einstein equation with cosmological constant Λ can be written as:

$$G^{\mu\nu} = R^{\mu\nu} - \left(\frac{R}{2} + \Lambda \right) g^{\mu\nu} = 8\pi G_N T^{\mu\nu}, \quad R = g_{\mu\nu} R^{\mu\nu}. \quad (1.2)$$

where G_N is the Newtonian gravitational constant, and $T^{\mu\nu}$ is the stress-energy tensor. Given the homogeneous and isotropic symmetry conditions imply that the matter content of the Universe can be expressed as a perfect fluid. The stress-energy tensor T_{ν}^{μ} of perfect fluid can be written as

$$T_{\nu}^{\mu} = \text{diag}(\rho, -P, -P, -P). \quad (1.3)$$

where ρ is energy density and an P is the isotropic pressure.

Substituting the perfect fluid form of the stress-energy tensor into the Einstein equations, one can derive the cosmological equations that describe the evolution of the Universe. We then obtain Friedmann equations as follows:

$$H^2 \equiv \left(\frac{\dot{a}}{a} \right)^2 = \frac{8\pi G_N}{3} \rho - \frac{k}{a^2} + \frac{\Lambda}{3}, \quad (1.4)$$

$$qH^2 = \frac{4\pi G_N}{3} (\rho + 3P) - \frac{\Lambda}{3}, \quad q \equiv -\frac{a\ddot{a}}{\dot{a}^2}, \quad (1.5)$$

where H is the Hubble parameter, q is the deceleration parameter. These equations relate the dynamics of the scale factor $a(t)$ to the energy density and pressure of the cosmic plasma. On the other hand, considering the divergence freedom of the total stress-energy tensor $\nabla_{\nu} T^{\mu\nu} = 0$. For $\mu = 0$ component, we have

$$\nabla_{\nu} T^{0\nu} = \frac{d\rho}{dt} + 3H(\rho + P) = 0 \quad (1.6)$$

which provides dynamical evolution equation for $\rho(t)$ and $P(t)$. Solutions of Eq. (1.6) describes the time evolution of energy density and pressures in the Universe. Given the energy density and pressure as a function of time, we can illustrates how the Universe evolves according to the Friedmann equations Eq. (1.4) and Eq. (1.5). Solving these equations allows us to understand the dynamics and evolution of the Universe such as the Hubble expansion and the behavior of matter and energy over cosmic time.

1.2 Approaching abundance equilibrium: Fermi/Bose distribution

In the early Universe, the reaction rates of particles in the cosmic plasma were much greater than the Universe expansion rate H . Therefore, the local thermal equilibrium has been maintained. Assuming the particles are in thermal equilibrium, the dynamical information can be obtained from the single-particle distribution function. The general relativistic covariant Fermi/Bose momentum distribution can be written as

$$f_{F/B}(\Upsilon_i, p_i) = \frac{1}{\Upsilon_i^{-1} \exp[(u \cdot p_i - \mu_i)/T] \pm 1} \quad (1.7)$$

where the plus sign applies for fermions, and the minus sign for bosons. The Lorentz scalar $(u_i \cdot p_i)$ is a scalar product of the particle four momentum p_i^μ with the local four vector of velocity u^μ . In the absence of local matter flow, the local rest frame is the laboratory frame

$$u^\mu = (1, \vec{0}), \quad p_i^\mu = (E_i, \vec{p}_i). \quad (1.8)$$

The parameter Υ_i is the fugacity of a given particle which describes the pair density and it is the same for both particles and antiparticles. For $\Upsilon_i = 1$ the distribution maximizes the entropy content at a fixed particle energy. The parameter μ_i is the chemical potential for a given particle which is associated to the density difference between particles and antiparticles.

In general there are two types of chemical equilibriums associated with the chemical parameters Υ and μ . We have:

- Absolute chemical equilibrium:

The absolute chemical equilibrium is the level to which energy is shared into accessible degrees of freedom, e.g. the particles can be made as energy is converted into matter. The absolute equilibrium is reached when the phase space occupancy approaches unity $\Upsilon \rightarrow 1$.

- Relative chemical equilibrium:

The relative chemical equilibrium is associated with the chemical potential

μ which involves reactions that distribute a certain already existent element/property among different accessible compounds.

The dynamics of absolute chemical equilibrium, in which energy can be converted to and from particles and antiparticles, is especially important. The consequences for the energy conversion to from particles/antiparticle can be seen in the first law of thermodynamics by introducing the general chemical potential μ_N for particle and $\mu_{\bar{N}}$ for antiparticle as follows:

$$\mu_N \equiv \mu + T \ln \Upsilon, \quad \mu_{\bar{N}} \equiv -\mu + T \ln \Upsilon. \quad (1.9)$$

Then the first law of thermodynamics can be written as

$$dE = -PdV + TdS + \mu_N dN + \mu_{\bar{N}} d\bar{N} \quad (1.10)$$

$$= -PdV + TdS + \mu(dN - d\bar{N}) + T \ln \Upsilon (dN + d\bar{N}). \quad (1.11)$$

It shows that the chemical potential μ is the energy required to change the difference between particles and antiparticles, and the $T \ln \Upsilon$ is the energy required to change the total number of particle and antiparticle, and the fugacity Υ is the parameter to adjust the energy.

Boltzmann equation and particle freeze-out

The Boltzmann equation describes the evolution of distribution function f in phase space. The Boltzmann equation in the FLRW universe can be written as

$$\frac{\partial f}{\partial t} - \frac{(E^2 - m^2)}{E} H \frac{\partial f}{\partial E} = \frac{1}{E} \sum_q C_q[f], \quad (1.12)$$

where $H = \dot{a}/a$ is the Hubble parameter. Due to homogeneity and isotropy of the Universe, the distribution function depends on time t and energy $E = \sqrt{p^2 + m^2}$ only. The collision term $\sum_q C_q$ represents all elastic and inelastic interactions and q labels the corresponding physical process. In general, the collision term is proportional to the relaxation time for given collision as follows [Anderson and Witting

(1974)]

$$\frac{1}{E}C_q[f] \propto \frac{1}{\tau_{rel}} \quad (1.13)$$

where τ_{rel} is the relaxation time for the reaction, which is on the order of magnitude of time for the reaction to reach chemical equilibrium.

As the Universe expands, the collision term in the Boltzmann equation competes with the Hubble term. In general, a given particle freeze-out from the cosmic plasma when its interaction rate τ_{rel}^{-1} becomes smaller than the Hubble expansion rate

$$H \geq \tau_{rel}^{-1}. \quad (1.14)$$

When this happens, the particle's interactions are not rapid enough to maintain thermal distribution, either because the density of particles becomes so low that the chances of any two particles meeting each other becomes negligible, or because the particle energy becomes too low to interact. The freeze-out process can be categorized into three distinct stages based on the type of freeze-out interactions, we have [Birrell et al. (2014a); Rafelski et al. (2023)]:

- Chemical freeze-out :

As the Universe expands and the temperature drops, the rate of the inelastic scattering (e.g. production and annihilation reaction) that maintain the equilibrium density becomes smaller than the expansion rate. At this point, the inelastic scattering ceases, and a relic population of particles remain. Prior to the chemical freeze-out temperature, number changing processes are significant and keep the particle in thermal equilibrium, implying that the distribution function has the usual Fermi-Dirac form

$$f_{th}(t, E) = \frac{1}{\exp[(E - \mu)/T] + 1}, \quad \text{for } T(t) > T_{ch}. \quad (1.15)$$

where T_{ch} represents the chemical freeze-out temperature.

- Kinetic freeze-out:

After chemical freeze-out, particles still scatter elastically from other particles

and keep thermal equilibrium in the primordial plasma. As the temperature drops, the rate of elastic scattering reaction that maintain the thermal equilibrium become smaller than the expansion rate. At that time, elastic scattering processes cease, and the relic particles do not interact with other particles in the primordial plasma anymore. Before the kinetic freeze-out, the distribution function has the form

$$f_k(t, E) = \frac{1}{\Upsilon^{-1} \exp[(E - \mu)/T] + 1}, \quad \text{for } T_f < T(t) < T_{ch}, \quad (1.16)$$

where T_f represents the kinetic freeze-out temperature. The generalized fugacity $\Upsilon(t)$ controls the occupancy of phase space and is necessary once $T(t) < T_{ch}$ in order to conserve particle number.

- Free streaming:

After kinetic freeze-out, the particles have fully decoupled from the primordial plasma, and thereby ceased influencing the dynamics of the Universe and become free-streaming. The Einstein-Vlasov equation can be solved [Choquet-Bruhat (2008)] and the free-streaming momentum distribution can be written as [Birrell et al. (2014a)]

$$f_{fs}(t, E) = \frac{1}{\Upsilon^{-1} \exp \left[\sqrt{\frac{E^2 - m^2}{T_{fs}^2} + \frac{m^2}{T_f^2}} - \frac{\mu}{T_f} \right] + 1}, \quad T_{fs}(t) = \frac{T_f a(t_k)}{a(t)}, \quad (1.17)$$

where the free-streaming effective temperature T_{fs} is obtained by redshifting the temperature at kinetic freeze-out. If a massive particle (e.g. dark matter) freeze-out from cosmic plasma in the nonrelativistic regime, $m \gg T_f$. We can use the Boltzmann approximation, and the free-streaming distribution for nonrelativistic particle becomes

$$f_{fs}^B(t, p) = \Upsilon e^{-(m+\mu)/T_f} \exp \left[-\frac{1}{T_{eff}} \frac{p^2}{2m} \right], \quad T_{eff} = \left(\frac{a(t_f)}{a(t)} \right)^2 T_f, \quad (1.18)$$

where we define the effective temperature T_{eff} for massive free-streaming particle. In this scenario, the effective temperature for massive particles decreases

faster than the Universe temperature cools. It's worth emphasizing the different temperatures between cold free-streaming particles and hot cosmic plasma would affect the evolution of the early Universe and require more detailed study.

The division of the freeze-out process into these three regimes is a simplification. However, it is a very useful approximation in the study of cosmology [Mangano et al. (2005); Birrell et al. (2015)] . For detailed discussion, see [Birrell et al. (2014a); Rafelski et al. (2023)].

1.3 Thermodynamics of the Early Universe

In the case of local thermal equilibrium, the laws of thermodynamics can provide a framework for understanding the behavior of particle's energy density, pressure, number density and entropy in the early Universe.

Using the relativistic covariant Fermi/Bose momentum distribution, the corresponding energy density, pressure, and number densities for particle species i are given by

$$\rho_i = g_i \int \frac{d^3p}{(2\pi)^3} E f_{F/B} = \frac{g_i}{2\pi^2} \int_{m_i}^{\infty} dE \frac{E^2 (E^2 - m_i^2)^{1/2}}{\Upsilon_i^{-1} e^{(E-\mu_i)/T} \pm 1}, \quad (1.19)$$

$$P_i = g_i \int \frac{d^3p}{(2\pi)^3} \frac{p^2}{3E} f_{F/B} = \frac{g_i}{6\pi^2} \int_{m_i}^{\infty} dE \frac{(E^2 - m_i^2)^{3/2}}{\Upsilon_i^{-1} e^{(E-\mu_i)/T} \pm 1}, \quad (1.20)$$

$$n_i = g_i \int \frac{d^3p}{(2\pi)^3} f_{F/B} = \frac{g_i}{2\pi^2} \int_{m_i}^{\infty} dE \frac{E (E^2 - m_i^2)^{1/2}}{\Upsilon_i^{-1} e^{(E-\mu_i)/T} \pm 1} \quad (1.21)$$

where g_i is the degeneracy of the particle species. By including the fugacity parameter Υ_i allows us to characterize particle properties in nonchemical equilibrium situations. On the other hand, the corresponding free-streaming energy density,

pressure, and number densities can be written as

$$\rho_i = g_i \int \frac{d^3 p}{(2\pi)^3} E f_{fs} = \frac{g_i}{2\pi^2} \int_{m_i}^{\infty} dE \frac{E^2 (E^2 - m_i^2)^{1/2}}{\Upsilon_i^{-1} e^{\sqrt{p^2/T_{fs}^2 + m_i^2/T_f^2} - \mu_i/T_f} \pm 1}, \quad (1.22)$$

$$P_i = g_i \int \frac{d^3 p}{(2\pi)^3} \frac{p^2}{3E} f_{fs} = \frac{g_i}{6\pi^2} \int_{m_i}^{\infty} dE \frac{(E^2 - m_i^2)^{3/2}}{\Upsilon_i^{-1} e^{\sqrt{p^2/T_{fs}^2 + m_i^2/T_f^2} - \mu_i/T_f} \pm 1}, \quad (1.23)$$

$$n_i = g_i \int \frac{d^3 p}{(2\pi)^3} f_{fs} = \frac{g_i}{2\pi^2} \int_{m_i}^{\infty} dE \frac{E(E^2 - m_i^2)^{1/2}}{\Upsilon_i^{-1} e^{\sqrt{p^2/T_{fs}^2 + m_i^2/T_f^2} - \mu_i/T_f} \pm 1}, \quad (1.24)$$

which are different from the thermal equilibrium Eq. (1.19), Eq. (1.20), and Eq. (1.21), by replacing the mass by a time dependant effective mass $m T_{fs}(t)/T_f$ in the exponential.

Given the energy density, pressure, and number densities, the entropy density for particle species i can be written as

$$\sigma_i = \frac{S_i}{V} = \left(\frac{\rho_i + P_i}{T} - \frac{\mu_i}{T} n_i \right). \quad (1.25)$$

In general the chemical potential is associated with the baryon number. Since the net baryon number density relative to the photon number density is of order 10^{-9} . In this case, we can neglect the small chemical potential when calculating the total entropy density in the Universe. The total entropy density in the early Universe can be written as

$$\sigma = \sum_i \sigma_i = \frac{2\pi^2}{45} g_*^s T^3, \quad (1.26)$$

$$g_*^s = \sum_{i=\text{bosons}} g_i \left(\frac{T_i}{T_\gamma} \right)^3 B \left(\frac{m_i}{T_i} \right) + \frac{7}{8} \sum_{i=\text{fermions}} g_i \left(\frac{T_i}{T_\gamma} \right)^3 F \left(\frac{m_i}{T_i} \right), \quad (1.27)$$

where g_*^s counts the effective number of ‘entropy’ degrees of freedom. The functions $B(m_i/T)$ and $F(m_i/T)$ are defined as

$$B \left(\frac{m_i}{T} \right) = \frac{45}{12\pi^4} \int_{m_i/T}^{\infty} dx \sqrt{x^2 - \left(\frac{m_i}{T} \right)^2} \left[4x^2 - \left(\frac{m_i}{T} \right)^2 \right] \frac{1}{\Upsilon_i^{-1} e^x - 1}, \quad (1.28)$$

$$F \left(\frac{m_i}{T} \right) = \frac{45}{12\pi^4} \frac{8}{7} \int_{m_i/T}^{\infty} dx \sqrt{x^2 - \left(\frac{m_i}{T} \right)^2} \left[4x^2 - \left(\frac{m_i}{T} \right)^2 \right] \frac{1}{\Upsilon_i^{-1} e^x + 1}. \quad (1.29)$$

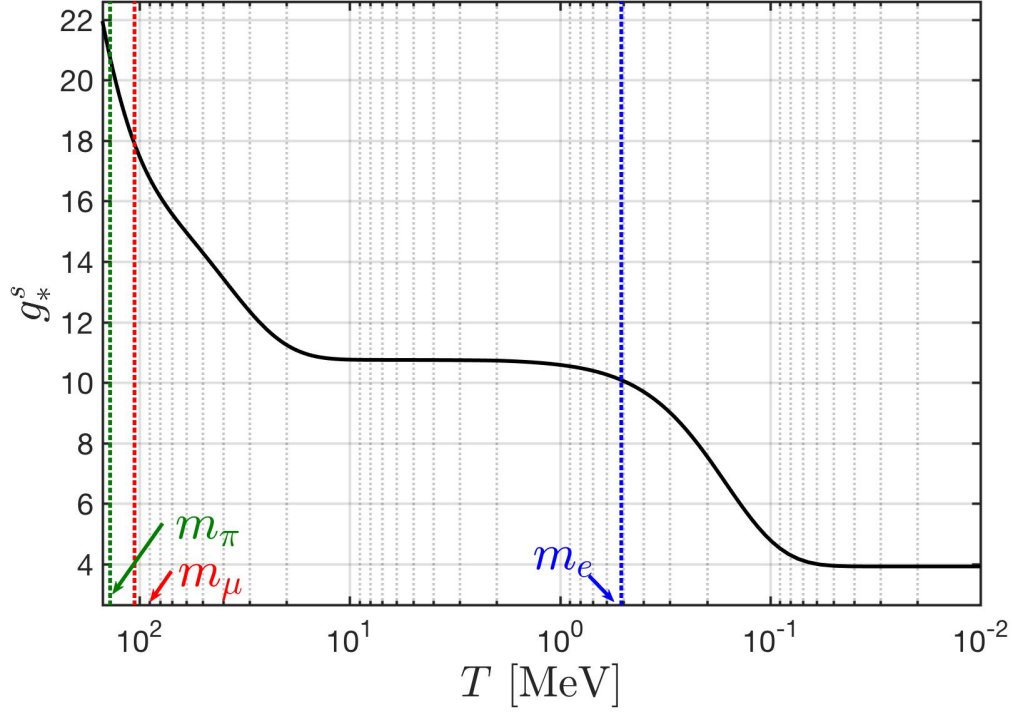


Figure 1.1: The entropy degrees of freedom as a function of T in the early Universe epoch after hadronization $10^{-2} \text{ MeV} \leq T \leq 150 \text{ MeV}$. When particle species becomes nonrelativistic $T \ll m_i$, the contribution to g_*^s becomes negligible, as a result creating the dependence $g_*^s(T)$. The vertical lines represent the mass of particles: $m_e = 0.511 \text{ MeV}$, $m_\mu = 105.6 \text{ MeV}$, and pion average mass $m_\pi \approx 138 \text{ MeV}$.

In Fig. 1.1 we plot the g_*^s as a function of temperature, the effect of particle mass threshold [Coc et al. (2006)] is considered in the calculation for all involved particles. When T decreases below the mass of particle $T \ll m_i$, this particle species becomes nonrelativistic and the contribution to g_*^s becomes negligible, creating the dependence on T seen in Fig. 1.1.

Relation between time and temperature

Considering the comoving entropy conservation, we have

$$S = \sigma V \propto g_*^s T^3 a^3 = \text{constant}, \quad (1.30)$$

where g_*^s is the entropy degree of freedom and a is the scale factor. Differentiating the entropy with respect to time t we obtain

$$\left[\frac{\dot{T}}{g_*^s} \frac{dg_*^s}{dT} + 3 \frac{\dot{T}}{T} + 3 \frac{\dot{a}}{a} \right] g_*^s T^3 a^3 = 0, \quad \dot{T} = \frac{dT}{dt}. \quad (1.31)$$

Solving dT/dt and taking the integral, the relation between time and temperature in early universe can be written as

$$t(T) = t_0 - \int_{T_0}^T dT \frac{1}{HT} \left[1 + \frac{T}{3g_*^s} \frac{dg_*^s}{dT} \right], \quad H^2 = \frac{8\pi G_N}{3} \rho_{tot} \quad (1.32)$$

where T_0 and t_0 represent the initial temperature and time respectively, H is the Hubble parameter and ρ_{tot} is the total energy density in early Universe. From Eq. (1.32) we see that the cosmic time depends on the entropy degrees of freedom g_*^s , which are characterized by the relativistic components in the early Universe. In the temperature range we consider $300 \text{ MeV} > T > 0.02 \text{ MeV}$ the Universe is radiation-dominated and Λ CDM model is not used in this epoch.

The baryon-per-entropy density ratio

An important assumption allowing us to explore the early Universe evolution is that following on the era of matter genesis both baryon and entropy content is conserved in the comoving volume. Both baryon and entropy density scale with the third power of the expansion parameter $a(t)$. Therefore the ratio of baryon number density to visible matter entropy density remains constant throughout the evolution of universe. We have

$$\frac{n_B - n_{\bar{B}}}{\sigma} = \frac{n_B - n_{\bar{B}}}{\sigma} \Big|_{t_0} = \text{Const}. \quad (1.33)$$

The subscript t_0 denotes the present day condition, and σ is the total entropy density. The observation gives the present baryon-to-photon ratio [Workman et al. (2022)] $5.8 \times 10^{-10} \leq (n_B - n_{\bar{B}})/n_\gamma \leq 6.5 \times 10^{-10}$. This small value quantifies the matter-antimatter asymmetry in the present day Universe, and allows the determination of

the present value of baryon per entropy ratio [Rafelski (2020); Fromerth and Rafelski (2002); Fromerth et al. (2012)]:

$$\left. \frac{n_B - n_{\bar{B}}}{\sigma} \right|_{t_0} = \eta \left(\frac{n_\gamma}{\sigma_\gamma + \sigma_\nu} \right)_{t_0} = (8.69 \pm 0.05) \times 10^{-11}, \quad \eta = \frac{(n_B - n_{\bar{B}})}{n_\gamma}, \quad (1.34)$$

where the $\eta = (6.12 \pm 0.04) \times 10^{-10}$ [Workman et al. (2022)] is used in calculation. To obtain the ratio, we consider that the Universe today is dominated by photons and free-streaming massless neutrinos [Birrell et al. (2014a)], and σ_γ and σ_ν are the entropy densities for photon and neutrino respectively. We have

$$\frac{\sigma_\nu}{\sigma_\gamma} = \frac{7}{8} \frac{g_\nu}{g_\gamma} \left(\frac{T_\nu}{T_\gamma} \right)^3 \quad \frac{T_\nu}{T_\gamma} = \left(\frac{4}{11} \right)^{1/3} \quad (1.35)$$

and the entropy-per-particle for massless bosons and fermions are given by [Fromerth et al. (2012)]

$$s/n|_{\text{boson}} \approx 3.60, \quad s/n|_{\text{fermion}} \approx 4.20. \quad (1.36)$$

However, from the neutrino oscillation experiment, we know that the the neutrinos are not massless particles. The mass differences between neutrino mass eigenstates are [Workman et al. (2022)]:

$$\Delta m_{21}^2 = 7.39_{-0.20}^{+0.21} \times 10^{-5} \text{ eV}^2, \quad (1.37)$$

$$\Delta m_{32}^2 = 2.45_{-0.03}^{+0.03} \times 10^{-3} \text{ eV}^2. \quad (1.38)$$

Neutrino mass eigenvalues can be ordered in the normal mass hierarchy ($m_1 \ll m_2 < m_3$) or inverted mass hierarchy ($m_3 \ll m_1 < m_2$). All three mass states remained relativistic until the temperature dropped below their rest mass. These results allow for the possibility that one mass eigenstate or two mass eigenstates of neutrinos may become non-relativistic today, which can affect the baryon-per-entropy ratio.

Nonequilibrium: departure from detailed balance

Thermal equilibrium implies both chemical equilibrium (particles abundances are balanced) and kinetic equilibrium (energy is evenly distributed). In chemical equilibrium, the rates of the forward and reverse reactions are equal, resulting in a

balance between production and annihilation/decay rates, which is called detailed balance. The chemical non-equilibrium can be achieved by breaking this detailed balance and leading to change in particle abundance over time. On the other hand, kinetic equilibrium is usually established much quicker and has less impact on the actual particle abundances. The chemical nonequilibrium condition is more important than the kinetic equilibrium because it relates to the arrow of time for the particle reactions.

The chemical nonequilibrium conditions in the early Universe are of general interest: they are understood to be prerequisite for the arrow of time dependent processes to take hold in the Hubble expanding Universe. The arrow of time plays an important role in the evolution of the early Universe, for example: 1.) The Big Bang Nucleosynthesis (BBN) [Pitrou et al. (2018); Kolb and Turner (1990b); Dodelson (2003); Mukhanov (2005)] the synthesis of light elements of e.g. D, ^3He , ^4He , and ^7Li are produced at temperatures around $86 \text{ keV} > T_{BBN} > 50 \text{ keV}$. 2.) Baryogenesis is believed to occur at or before the Universe underwent electroweak phase transition [Kolb and Turner (1990b)] at a temperature $T \simeq 130 \text{ GeV}$, which generates the excess of baryon number compared to anti-baryon number in order to create the observed baryon number today.

When Universe expands and temperature cools down, the chemical non-equilibrium can be achieved by breaking the detailed balance between particle production reaction and annihilation/decay as follows:

1.) The particle production rate becomes slower than the rate of Universe expansion and the production reaction freezeout. Once the production reactions freezeout from the cosmic plasma, the corresponding detailed balance is broken and particle abundance decrease via the decay/annihilation reactions.

2.) The non-equilibrium can also be achieved when the production reaction slows down and is not able to keep up with decay/annihilation reaction. In this case, the Hubble expansion rate is much longer than the decay and production rate and is not relevant to the nonequilibrium process. The key factor is competition between production and decay/annihilation which can result in chemical nonequilibrium in

the early Universe.

We will investigate the nonequilibrium situation for bottom quarks and strange quarks in early universe and their application in Chapter 2 and Chapter 3, respectively.

1.4 Cosmic plasma in early Universe $300 \text{ MeV} > T > 0.02 \text{ MeV}$

The primordial hot Universe fireball underwent several practically adiabatic phase changes that dramatically evolved its bulk properties as it expanded and cooled [Rafelski et al. (2023)]. We present an overview of the Universe evolution as a function of temperature from $300 \text{ MeV} > T > 0.02 \text{ MeV}$ and main events constituting the history of the early Universe in Fig. 1.2. After the electroweak symmetry breaking epoch and presumably inflation, the cosmic plasma in the early Universe evolves in the following sequence:

1. **Primordial quark-gluon plasma:** At early times when the temperature was between $130 \text{ GeV} > T > 0.15 \text{ GeV}$ we have the building blocks of the Universe as we know them today, including the leptons, vector bosons, and all three families of deconfined quarks and gluons which propagated freely in plasma. As all hadrons are dissolved into their constituents during this time, strongly interacting particles u, d, s, t, b, c, g controlled the fate of the Universe. When temperature is near to the QGP phase transition $300 \text{ MeV} > T > 150 \text{ MeV}$, the bottom quark breaks the detail balance and disappearance from particle inventory provides the arrow in time (see Chapter 2 for detail).
2. **Hadronic epoch:** Around the hadronization temperature $T_H \approx 150 \text{ MeV}$, a phase transformation occurred, forcing the free quarks and gluons become confined within baryon and mesons [Letessier and Rafelski (2008)]. In the temperature range $150 \text{ MeV} > T > 20 \text{ MeV}$, the Universe is rich in physics phenomena involving strange mesons and (anti)baryons including (anti)hyperon abundances [Fromerth et al. (2012); Yang and Rafelski (2022)]. The antibaryons disappear from the Universe at temperature $T = 38.2 \text{ MeV}$, and

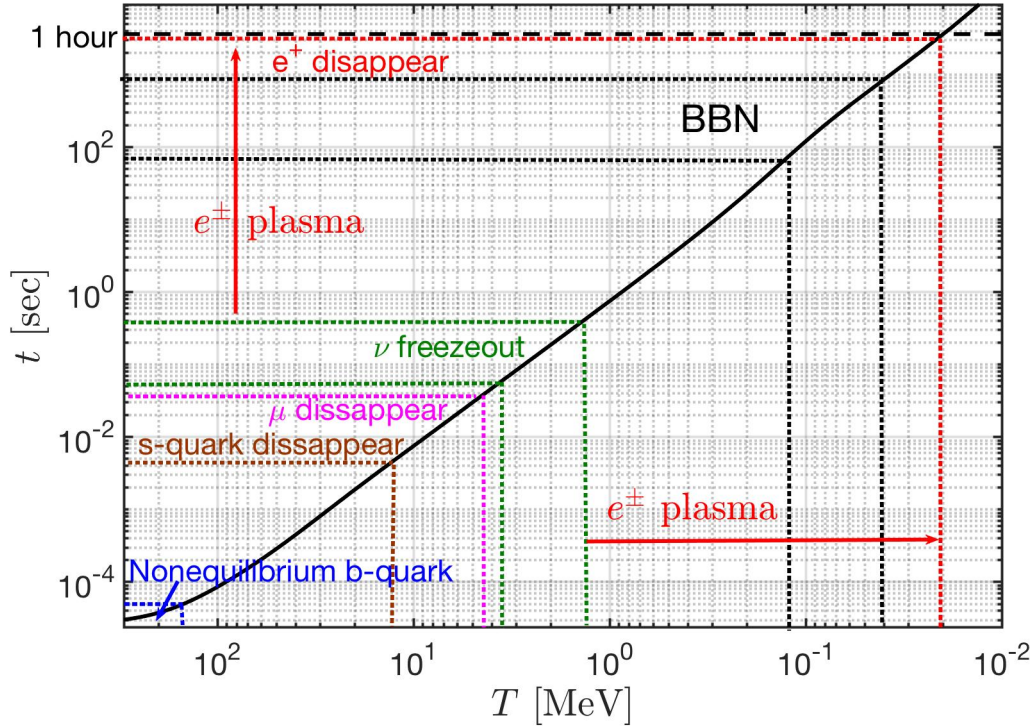


Figure 1.2: The time evolution of the early Universe as a function of temperature from $300 \text{ MeV} > T > 0.02 \text{ MeV}$ and different sequence of main events are shown with the temperature/time range in the evolution.

strangeness can be produced by the inverse decay reactions that are in equilibrium via weak, electromagnetic, and strong interactions in the early Universe until $T \approx 13 \text{ MeV}$ (see Chapter 3 for detailed discussion).

- Lepton-photon epoch:** For temperature $10 \text{ MeV} > T > 2 \text{ MeV}$, the Universe contained relativistic electrons, positrons, photons, and three species of (anti)neutrinos. During this epoch massless leptons and photons controlled the fate of the Universe. Massive τ^\pm disappear from the plasma at high temperature via decay processes. However μ^\pm leptons can persist in the early Universe until temperature $T = 4.2 \text{ MeV}$, and positron e^+ can persist until the temperature $T = 0.02 \text{ MeV}$ (See Chapter 5 for discussion). Neutrinos were still coupled to the charged leptons via the weak interaction [Birrell et al. (2014a);

Birrell (2014)] and freeze-out at temperature range $3 \text{ MeV} > T > 2 \text{ MeV}$ which depends on the neutrino's flavors and the magnitude of the Standard Model parameters (See Chapter 4 for details). After neutrino freeze-out, they still play an important role in the Universe expansion via the effective number of neutrinos N_ν^{eff} and affects the Hubble parameter significantly.

4. **Electron-positron epoch:** After neutrinos freeze-out at $T = 3 \sim 2 \text{ MeV}$ and become free-streaming in the early Universe, the cosmic plasma was dominated by electrons, positrons, and photons. The e^\pm plasma existed until $T \approx 0.02 \text{ MeV}$ such that BBN occurred within a rich electron-positron plasma, and the dense number density of electron/positron also provides the opportunities to investigate magnetization process (See Chapter 5 for detailed discussion). This is the last time the Universe will contain a significant fraction of its content in antimatter.

After e^\pm annihilation, the Universe was still opaque to photons at this point and remained so until the recombination period at $T \approx 0.25 \text{ eV}$ starting the era of observational cosmology with the Cosmic Microwave Background. This period has been studied in detail before in [Aghanim et al. (2020a)]. Therefore, we focus on the temperature $300 \text{ MeV} > T > 0.02 \text{ MeV}$ which corresponds to the first hour of the Universe evolution. We will address the cosmic plasma as follows: In Chapter 2, we discuss the heavy quarks (bottom/charm) abundance near to the QGP hadronization and show the nonequilibrium of bottom quark. In Chapter 3 we study the strangeness abundance after hadronization and show the long lasting strangeness in the early Universe. In Chapter 4 we focus on the neutrino-matter interactions and the evolution of cosmic neutrino in early universe before/after freeze-out. In Chapter 5 we study the abundance of charged leptons μ^\pm and e^\pm and show that the presence of e^\pm plasma plays an important role in early Universe. In Chapter 6 we address the ongoing and prospective research projects for future publication. Finally in Chapter 7 we summarize the important results of our study and conclusion.

CHAPTER 2

Heavy quarks in cosmic plasma

The primordial quark-gluon plasma (QGP) refers to the state of matter that existed in the early Universe, specifically for time $t \approx 10 \mu\text{s}$ after the Big Bang. At that time the Universe was controlled by the strongly interacting particles: quarks and gluons. In this chapter, I study the heavy bottom and charm flavor quarks near to the QGP hadronization temperature $0.3 \text{ GeV} > T > 0.15 \text{ GeV}$ and examine the relaxation time for the production and decay of bottom/charm quarks then show that the bottom quark nonequilibrium occur near to QGP –hadronization and create the arrow in time in the early Universe.

2.1 Overview of heavy quarks in primordial QGP

In the QGP epoch, up and down (u, d) (anti)quarks are effectively massless and remain in equilibrium via quark-gluon fusion. Strange (s) (anti)quarks are in equilibrium via weak, electromagnetic, and strong interactions until $T \approx 13 \text{ MeV}$ [Yang and Rafelski (2022)]. The massive top (t) (anti)quarks decay via the channel $t \rightarrow W + b$, with $\Gamma_t = 1.4 \pm 0.2 \text{ GeV}$ [Tanabashi et al. (2018)] which implies that no bound state of top quarks have time to form. Given the large value of Γ_t we realize that top quarks in hot QGP can be produced by the $W + b \rightarrow t$ fusion process – given the strength of this process there is no freeze-out of top quarks until W itself freezes out. To address the top quarks in QGP, a dynamic theory for W abundance is needed, a topic we will consider in the future. Finally, the bottom (b) and charm (c) quarks can be produced from strong interactions via quark-gluon pair fusion processes and disappear via weak interaction decays, and their abundance depends on the competition between the strong fusion and weak decay reaction rates.

The properties of QGP can be studied by experimental observations from high-

energy heavy-ion collision experiments, such as the Relativistic Heavy Ion Collider (RHIC) and the Large Hadron Collider (LHC). However, the conditions in the early Universe and those created in relativistic collisions are different. For example, the primordial QGP survives for about $10\mu\text{s}$ in the cosmological Big Bang. On the other hand, the QGP formed in micro-bangs resulting from ultra-relativistic nuclear collisions has a lifespan of around 10^{-23} s [Rafelski et al. (2001)]. Due to the considerably slower expansion rate of the Universe compared to quark production reactions and decays, in practicality, quark remained in equilibrium, and the quark fugacity is $\Upsilon = 1$ during the QGP epoch.

However near the hadronization temperature, the heavy quarks abundance and deviations from chemical equilibrium have not yet been studied in great detail. In following we will focus on bottom and charm quarks. We will show that the bottom quarks can deviate from chemical equilibrium $\Upsilon \neq 1$ by breaking the detailed balance between production and decay reactions of the quarks.

2.2 Bottom and Charm quark near QGP hadronization

In the following we consider the temperature near QGP hadronization $0.3\text{ GeV} > T > 0.15\text{ GeV}$, and study the bottom and charm abundance by examining the relevant reaction rates of their production and decay. In thermal equilibrium the number density of light quarks can be evaluated in the massless limit, and we have

$$n_q = \frac{g_q}{2\pi^2} T^3 F(\Upsilon_q), \quad F = \int_0^\infty \frac{x^2 dx}{1 + \Upsilon_q^{-1} e^x}, \quad (2.1)$$

where Υ_q is the quark fugacity. We have $F(\Upsilon_q = 1) = 3\zeta(3)/2$ with the Riemann zeta function $\zeta(3) \approx 1.202$. The thermal equilibrium number density of heavy quarks with mass $m \gg T$ can be well described by the Boltzmann expansion of the Fermi distribution function, giving

$$n_q = \frac{g_q T^3}{2\pi^2} \sum_{n=1}^{\infty} \frac{(-1)^{n+1} \Upsilon_q^n}{n^4} \left(\frac{n m_q}{T}\right)^2 K_2\left(\frac{n m_q}{T}\right), \quad (2.2)$$

where K_2 is the modified Bessel functions of integer order 2. In the case of interest, when $m \gg T$, it suffices to consider the Boltzmann limit and keep the first term

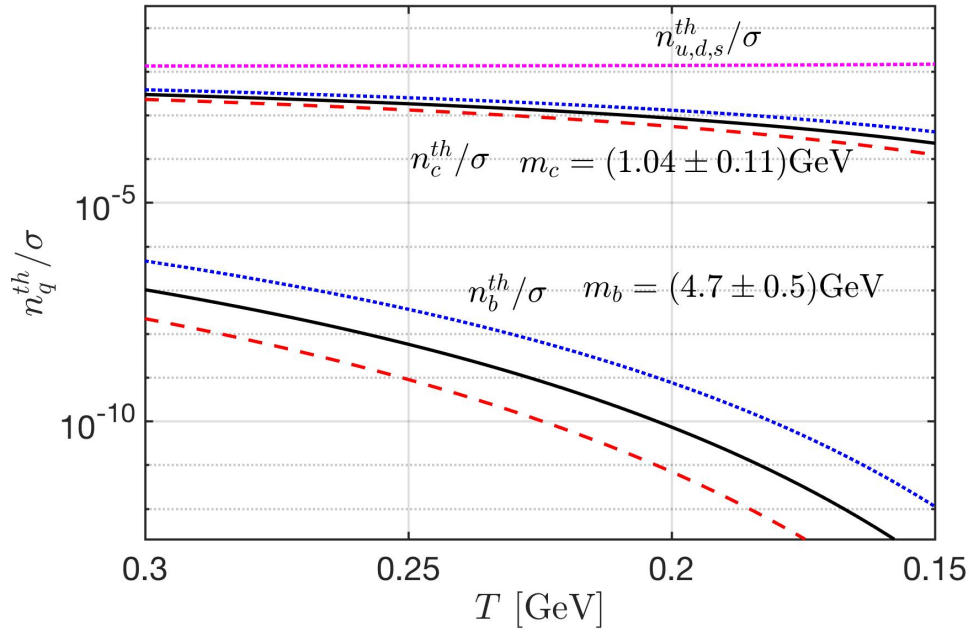


Figure 2.1: The quark number density normalized by entropy density, as a function of temperature in the early Universe with $\Upsilon = 1$. The b -quark mass parameters shown are $m_b = 4.2$ GeV (blue) dotted line, $m_b = 4.7$ GeV (black) solid line, and $m_b = 5.2$ GeV (red) dashed line. For c -quark $m_c = 0.93$ GeV (blue) dotted line, $m_c = 1.04$ GeV (black) solid line, and $m_c = 1.15$ GeV (red) dashed line.

$n = 1$ in the expansion. The first term $n = 1$ also suffices for both charmed c -quarks and bottom b -quarks, giving

$$n_{b,c} = \Upsilon_{b,c} n_{b,c}^{th}, \quad n_{b,c}^{th} = \frac{g_{b,c}}{2\pi^2} T^3 \left(\frac{m_{b,c}}{T} \right)^2 K_2(m_{b,c}/T). \quad (2.3)$$

However, for strange s quarks, several terms are needed.

In Fig. 2.1 we show the equilibrium ($\Upsilon = 1$) number density per entropy density ratio as a function of temperature T of quarks. The entropy density is given by Eq. (1.25) and only light particles contribute to the entropy density; thus the result we consider is independent of actual abundance of c , b and other heavy particles. We evaluated the density-per-entropy ratio for $m_b = 4.2, 4.7, 5.2$ GeV and $m_c = 1.04 \pm 0.11$ GeV. The $m_b \simeq 5.2$ GeV is a typical potential model mass used in modeling bound states of bottom, and $m_b = 4.2, 4.7$ GeV is the current quark mass

at low and high energy scales. In Fig. 2.1 we see that the charm abundance in the domain of interest $0.3 \text{ GeV} > T > 0.15 \text{ GeV}$ is about $10^4 \sim 10^9$ times greater than the bottom quarks. This implies that the small b, \bar{b} quark abundance is embedded in a large background comprising all lighter u, d, s, c quarks and antiquarks, as well as gluons g .

2.2.1 Reaction rate for quarks production and decay

In primordial QGP, the bottom and charm quarks can be produced from strong interactions via quark-gluon pair fusion processes and disappear via weak interaction decays. For production, we have the following processes

$$q + \bar{q} \longrightarrow b + \bar{b}, \quad q + \bar{q} \longrightarrow c + \bar{c}, \quad (2.4)$$

$$g + g \longrightarrow b + \bar{b}, \quad g + g \longrightarrow c + \bar{c}, \quad (2.5)$$

for bottom and charm we have

$$b \longrightarrow c + l + \bar{\nu}_l, \quad b \longrightarrow c + q + \bar{q}, \quad (2.6)$$

$$c \longrightarrow s + l + \bar{\nu}_l, \quad c \longrightarrow s + q + \bar{q}, \quad (2.7)$$

for their decay. In following we will calculate the production rate and decay rate for bottom and charm quarks and compare to the Universe expansion rate. We will show that in the epoch of interest to us the characteristic Universe expansion time $1/H$ is much longer than the lifespan and production time of the bottom/charm quark. In this case, the dilution of bottom/charm quark due to the Universe expansion is slow compare to the the strong interaction production, and the weak interaction decay of the bottom/charm.

Quark production rate via strong interaction

For the quark-gluon pair fusion processes the evaluation of the lowest-order Feynman diagrams yields the cross sections [Letessier and Rafelski (2002)]:

$$\sigma_{q\bar{q}\rightarrow b\bar{b},c\bar{c}} = \frac{8\pi\alpha_s^2}{27s} \left(1 + \frac{2m_{b,c}^2}{s}\right) w(s), \quad w(s) = \sqrt{1 - 4m_{b,c}^2/s}, \quad (2.8)$$

$$\sigma_{gg\rightarrow b\bar{b},c\bar{c}} = \frac{\pi\alpha_s^2}{3s} \left[\left(1 + \frac{4m_{b,c}^2}{s} + \frac{m_{b,c}^4}{s^2}\right) \ln\left(\frac{1+w(s)}{1-w(s)}\right) - \left(\frac{7}{4} + \frac{31m_{b,c}^2}{4s}\right) w(s) \right], \quad (2.9)$$

where $m_{b,c}$ represents the mass of bottom or charm quark, s is the Mandelstam variable, and α_s is the QCD coupling constant. Considering the perturbation expansion of the coupling constant α_s for the two-loop approximation [Letessier and Rafelski (2002)], we have:

$$\alpha_s(\mu^2) = \frac{4\pi}{\beta_0 \ln(\mu^2/\Lambda^2)} \left[1 - \frac{\beta_1 \ln(\ln(\mu^2/\Lambda^2))}{\beta_0 \ln(\mu^2/\Lambda^2)} \right], \quad (2.10)$$

where μ is the renormalization energy scale and Λ^2 is a parameter that determines the strength of the interaction at a given energy scale in QCD. The energy scale we consider is based on required gluon/quark collisions above $b\bar{b}$ energy threshold, so we have $\mu = 2m_b + T$. For the energy scale $\mu > 2m_b$ we have $\Lambda = 180 \sim 230$ MeV ($\Lambda \approx 205$ MeV in our calculation), and the parameters $\beta_0 = 11 - 2n_f/3$, $\beta_1 = 102 - 38n_f/3$ with the number of active fermions $n_f = 4$.

In general the thermal reaction rate per unit time and volume R can be written in terms of the scattering cross section as follows [Letessier and Rafelski (2002)]:

$$R \equiv \sum_i \int_{s_{th}}^{\infty} ds \frac{dR_i}{ds} = \sum_i \int_{s_{th}}^{\infty} ds \sigma_i(s) P_i(s), \quad (2.11)$$

where $\sigma_i(s)$ is the cross section of the reaction channel i , and $P_i(s)$ is the number of collisions per unit time and volume. Considering the quantum nature of the colliding particles (i.e., Fermi and Bose distribution) with the massless limit and chemical equilibrium condition ($\Upsilon = 1$), we obtain [Letessier and Rafelski (2002)]

$$P_i(s) = \frac{g_1 g_2}{32\pi^4} \frac{T}{1 + I_{12}} \frac{\lambda_2}{\sqrt{s}} \sum_{l,n=1}^{\infty} (\pm)^{l+n} \frac{K_1(\sqrt{lns}/T)}{\sqrt{ln}}, \quad (2.12)$$

$$\lambda_2 \equiv [s - (m_1 + m_2)^2] [s - (m_1 - m_2)^2], \quad (2.13)$$

where $+$ is for boson and $-$ is for fermions, and the factor $1/(1 + I_{12})$ is introduced to avoid double counting of indistinguishable pairs of particles. $I_{12} = 1$ for identical pair of particles, otherwise $I_{12} = 0$. Hence the total thermal reaction rate per volume for bottom quark production can be written as

$$R_{b,c}^{\text{Source}} = \int_{s_{th}}^{\infty} ds \left[\sigma_{q\bar{q} \rightarrow b\bar{b}, c\bar{c}} P_q + \sigma_{gg \rightarrow b\bar{b}, c\bar{c}} P_g \right] \quad (2.14)$$

We introduce the bottom/charm quark relaxation time for the quark-gluon pair fusion as follows:

$$\tau_{b,c}^{\text{Source}} \equiv \frac{dn_{b,c}/d\Upsilon_{b,c}}{R_{b,c}^{\text{Source}}}, \quad (2.15)$$

where $dn_{b,c}/d\Upsilon_{b,c} = n_{b,c}^{th}$ in the Boltzmann approximation. The relaxation time is on the order of magnitude of time needed to reach chemical equilibrium. In Fig. 2.2 we show the characteristic time for bottom/charm quark strong interaction production in the domain of interest, $0.3 \text{ GeV} > T > 0.15 \text{ GeV}$.

Quark decay rate via weak interaction

The bottom/charm quark decay via the weak interaction. The vacuum decay rate for $1 \rightarrow 2 + 3 + 4$ in vacuum can be evaluated via the weak interaction:

$$\frac{1}{\tau_1} = \frac{64G_F^2 V_{12}^2 V_{34}^2}{(4\pi)^3 g_1} m_1^5 \times \left[\frac{1}{2} \left(1 - \frac{m_2^2}{m_1^2} - \frac{m_3^2}{m_1^2} + \frac{m_4^2}{m_1^2} \right) \mathcal{J}_1 - \frac{2}{3} \mathcal{J}_2 \right], \quad (2.16)$$

where the Fermi constant is $G_F = 1.166 \times 10^{-5} \text{ GeV}^{-2}$, V_{ij} is the element of the Cabibbo-Kobayashi-Maskawa (CKM) matrix [Czarnecki et al. (2004)] for quark channel and $V_{\nu_l} = 1$ for lepton channel. The functions \mathcal{J}_1 and \mathcal{J}_2 are given by

$$\mathcal{J}_1 = \int_0^{(1-m_2^2/m_1^2)/2} dx \left(1 - 2x - \frac{m_2^2}{m_1^2} \right)^2 \left[\frac{1}{(1-2x)^2} - 1 \right] \quad (2.17)$$

$$\mathcal{J}_2 = \int_0^{(1-m_2^2/m_1^2)/2} dx \left(1 - 2x - \frac{m_2^2}{m_1^2} \right)^3 \left[\frac{1}{(1-2x)^3} - 1 \right] \quad (2.18)$$

The modification due to the heat bath(plasma) is small because the bottom and charm mass $m_{b,c} \gg T$ [Kuznetsova et al. (2008)]. In the temperature range we are interested in, the decay rate in the vacuum is a good approximation for our calculation. We show the lifespan for bottom/charm quark in Fig. 2.2.

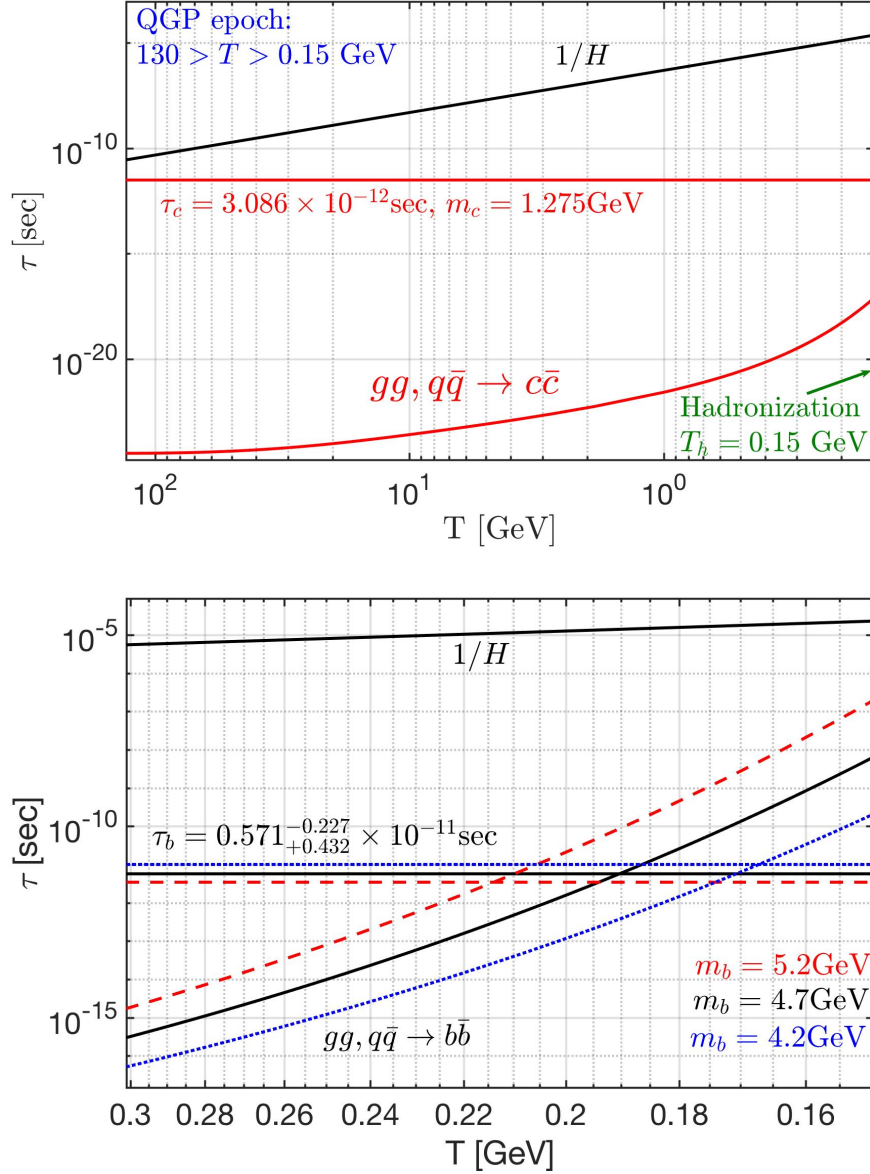


Figure 2.2: Comparison of Hubble time $1/H$, quark lifespan τ_q , and characteristic time for production via quark-gluon pair fusion for (top figure) charm and (bottom figure) bottom quarks as a function of temperature. Both figures end at approximately the hadronization temperature of $T_H \approx 150 \text{ MeV}$. Three different masses $m_b = 4.2 \text{ GeV}$ (blue short dashes), 4.7 GeV , (solid black), 5.2 GeV (red long dashes) for bottom quarks are plotted to account for its decay width.

Hubble expansion rate

In the early Universe, within a temperature range $130 \text{ GeV} > T > 0.15 \text{ GeV}$, we have the following particles: photons, 8 color charge gluons, W^\pm , Z^0 , three generations of 3 color charge quarks and leptons in the primordial QGP. The Hubble parameter can be written in terms of particle energy density ρ_i

$$H^2 = \frac{8\pi G_N}{3} (\rho_\gamma + \rho_{\text{lepton}} + \rho_{\text{quark}} + \rho_{g,W^\pm,Z^0}), \quad (2.19)$$

where G_N is the Newtonian constant of gravitation. The effectively massless particles and radiation dominate the speed of expansion of the Universe. The characteristic Universe expansion time constant $1/H$ is seen in Fig. 2.2. In the epoch of interest to us $0.3 \text{ GeV} > T > 0.15 \text{ GeV}$, the Hubble time $1/H \approx 10^{-5}$ sec which is much longer than the lifespan and production time of the bottom and charm quarks.

Rate Comparison: Strong fusion, Weak decay, and Hubble expansion

In Fig. 2.2 (top), we plot the relaxation time of the production/decay for charm quarks and Hubble time $1/H$ as a function of temperature. Throughout the entire duration of QGP, the Hubble time is larger than the lifespan and production times of the charm quark. Additionally, the charm quark production time is faster than the decay. The faster quark-gluon pair fusion keeps the charm in chemical equilibrium up until hadronization. After hadronization, charm quarks form heavy mesons that decay into multi-particles quickly in plasma. The daughter particles from charm meson decay can interact and reequilibrate with the plasma quickly. In this case the energy required for the inverse decay reaction to produce charm meson is difficult to overcome and causing the charm quark to vanish from the inventory of particles via decay in the Universe.

In Fig. 2.2 (bottom) we present the relaxation time for production and decay of the bottom quark with different masses as a function of temperature. It shows that both production and decay are faster than the Hubble time $1/H$ for the duration of QGP. However, unlike charm quarks, the relaxation time for bottom quark production intersects with bottom quark decay at different temperatures which depends on

the mass of the bottom. The intersection implies that the bottom quark freeze-out from the primordial plasma before hadronization as the production process slows down at low temperatures and the subsequent weak interaction decay leads to a dilution of the bottom quark content within the QGP plasma. All of this occurs with rates faster than Hubble expansion and thus as the Universe expands, the system departs from a detailed chemical balance because of the competition between decay and production reactions in QGP. In this scenario, the dynamic equation on bottom abundance is required and causes the distribution to deviate from equilibrium with $\Upsilon \neq 1$ in the temperature range below the crossing point but before the hadronization.

2.2.2 Bottom quark abundance nonequilibrium

The competition between weak interaction decay and strong interaction production rates leads the dynamic bottom abundance in QGP. The dynamic equation for bottom quark abundance in QGP can be written as

$$\frac{1}{V} \frac{dN_b}{dt} = (1 - \Upsilon_b^2) R_b^{\text{Source}} - \Upsilon_b R_b^{\text{Decay}} , \quad (2.20)$$

where R_b^{Source} and R_b^{Decay} are the thermal reaction rates per volume of production and decay of bottom quark, respectively. The bottom source rates are the gluon and quark fusion rates Eq. (2.14). The decay rate depends on whether the bottom quarks are freely present in the plasma or are bounded within mesons. We consider two extreme scenarios for the bottom quark population: 1.) all bottom flavor is free, and 2.) all bottom flavor is bounded into mesons in QGP. In Fig. 2.3 we show the characteristic interaction times relevant to the abundance of bottom quarks, as well as the Hubble time $1/H$ for the temperature range of interest, $0.3 \text{ GeV} > T > 0.15 \text{ GeV}$.

Considering all bottom flavor is free in QGP, the bottom decay rate per volume is the bottom lifespan weighted with density of particles Eq. (2.2) [Kuznetsova et al.

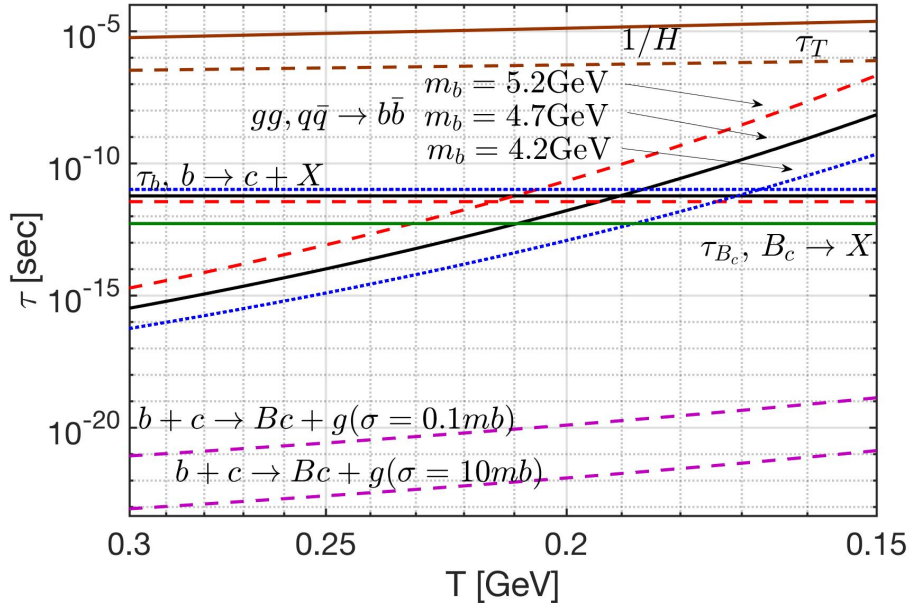


Figure 2.3: Production and decay characteristic times of bottom quark and the Hubble time $1/H$ within the temperature range of interest $0.3 \text{ GeV} > T > 0.15 \text{ MeV}$. Near the top of figure $1/H$ (brown solid line) and τ_T (brown dashed line); other horizontal lines are bottom-quark (in QGP) weak interaction lifetimes τ_b for the three different masses: $m_b = 4.2 \text{ GeV}$ (blue dotted line), $m_b = 4.7 \text{ GeV}$ (black solid line), $m_b = 5.2 \text{ GeV}$ (red dashed line), and the vacuum lifespan τ_B of the B_c meson (green solid line). The relaxation time for strong interaction bottom production $g + g, q + \bar{q} \rightarrow b + \bar{b}$ is shown with three different bottom masses and same type-color coding as weak interaction decay rate. At bottom of figure the in plasma formation process (dashed lines, purple) $b + c \rightarrow B_c + g$ with cross section range $\sigma = 0.1, 10 \text{ mb}$.

(2008)]. We have

$$R_b^{\text{Decay}} = \frac{dn_b/dY_b}{\tau_b}, \quad \tau_b \approx 0.57 \times 10^{-11} \text{ sec.} \quad (2.21)$$

On the other hand, b, \bar{b} quark abundance is embedded in a large background comprising all lighter quarks and antiquarks (see Fig. 2.1). After formation the heavy b, \bar{b} quark can bind with any of the available lighter quarks, with the most likely

outcome being a chain of reactions

$$b + q \longrightarrow B + g , \quad (2.22)$$

$$B + s \longrightarrow B_s + q , \quad (2.23)$$

$$B_s + c \longrightarrow B_c + s , \quad (2.24)$$

with each step providing a gain in binding energy and reduced speed due to the diminishing abundance of heavier quarks s, c . To capture the lower limit of the rate of B_c production we show in Fig. 2.3 the expected formation rate by considering the direct process $b + \bar{c} \rightarrow B_c + g$, considering the range of cross section $\sigma = 0.1 \sim 10$ mb [Schroedter et al. (2000)]. The rapid formation rate of $B_c(b\bar{c})$ states in primordial plasma is shown by purple dashed lines at bottom in Fig. 2.3, we have

$$\tau(b + \bar{c} \rightarrow B_c + g) \approx (10^{-16} \sim 10^{-14}) \times \frac{1}{H} . \quad (2.25)$$

Despite the low abundance of charm, the rate of B_c formation is relatively fast, and that of lighter flavored B-mesons is substantially higher. Note that as long as we have bottom quarks made in gluon/quark fusion bound practically immediately with any quarks u, d, s into B-mesons, we can use the production rate of b, \bar{b} pairs as the rate of B-meson formation in the primordial-QGP, which all decay with lifespan of pico-seconds. We believe that this process is fast enough to allow consideration of bottom decay from the $B_c(b\bar{c}), \bar{B}_c(\bar{b}c)$ states [Yang and Rafelski (2020)]. Based on the hypothesis that all bottom flavor is bound rapidly into B_c^\pm mesons, we have

$$g + g, q + q \longleftrightarrow b + \bar{b} [b(\bar{b}) + \bar{c}(c)] \longrightarrow B_c^\pm \longrightarrow \text{anything} . \quad (2.26)$$

In this case, the decay rate per volume can be written as

$$R_b^{\text{Decay}} = \frac{dn_b/d\Upsilon_b}{\tau_{B_c}}, \quad \tau_{B_c} \approx 0.51 \times 10^{-12} \text{sec} . \quad (2.27)$$

To investigate the nonequilibrium phenomena of bottom quarks, we aim to replace the variation of particle abundance seen on LHS in Eq. (2.20) by the time variation of abundance fugacity Υ . This substitution allows us to derive the dynamic equation for the fugacity parameter and enables us to study the fugacity as

a function of time . Considering the expansion of the Universe we have

$$\frac{1}{V} \frac{dN_b}{dt} = \frac{dn_b}{d\Upsilon_b} \frac{d\Upsilon_b}{dt} + \frac{dn_b}{dT} \frac{dT}{dt} + 3Hn_b, \quad (2.28)$$

where we use $d \ln(V)/dt = 3H$ for the Universe expansion. Substituting Eq. (2.28) into Eq. (2.20) and dividing both sides of equation by $dn_b/d\Upsilon_b = n_b^{th}$, the fugacity equation becomes

$$\frac{d\Upsilon_b}{dt} + 3H\Upsilon_b + \Upsilon_b \frac{dn_b^{th}/dT}{n_b^{th}} \frac{dT}{dt} = (1 - \Upsilon_b^2) \frac{1}{\tau_b^{\text{Source}}} - \Upsilon_b \frac{1}{\tau_b^{\text{Decay}}}, \quad (2.29)$$

where relaxation time for bottom production is obtained using Eq. (2.15). It is convenient to introduce the relaxation time $1/\tau_T$ as follows,

$$\frac{1}{\tau_T} \equiv - \frac{dn_b^{th}/dT}{n_b^{th}} \frac{dT}{dt}, \quad (2.30)$$

where we put '-' sign in the definition to have $\tau_T > 0$. The relaxation time τ_T represents how the bottom density changes due to the Universe temperature cooling. In this case, the fugacity equation can be written as

$$\frac{d\Upsilon_b}{dt} = (1 - \Upsilon_b^2) \frac{1}{\tau_b^{\text{Source}}} - \Upsilon_b \left(\frac{1}{\tau_b^{\text{Decay}}} + 3H - \frac{1}{\tau_T} \right). \quad (2.31)$$

In following sections we will solve the fugacity differential equation in two different scenarios: stationary and nonstationary Universe.

First solution: stationary Universe

In Fig. 2.2 (bottom) we show that the relaxation time for both production and decay are faster than the Hubble time $1/H$ for the duration of QGP, which implies that $H, 1/\tau_T \ll 1/\tau_b^{\text{Source}}, 1/\tau_b^{\text{Decay}}$. In this scenario, we can solve the fugacity equation by considering the stationary Universe first, i.e., the Universe is not expanding and we have

$$H = 0, \quad 1/\tau_T = 0. \quad (2.32)$$

In the stationary Universe at each given temperature we consider the dynamic equilibrium condition (detailed balance) between production and decay reactions that keep

$$\frac{d\Upsilon_b}{dt} = 0. \quad (2.33)$$

Neglecting the time dependence of the fugacity $d\Upsilon_b/dt$ and substituting the condition Eq. (2.32) into the fugacity equation Eq. (2.31), then we can solve the quadratic equation to obtain the stationary fugacity as follows:

$$\Upsilon_{st} = \sqrt{1 + \left(\frac{\tau_{source}}{2\tau_{decay}}\right)^2} - \left(\frac{\tau_{source}}{2\tau_{decay}}\right). \quad (2.34)$$

In Fig. 2.4 the fugacity of bottom quark Υ_{st} as a function of temperature, Eq. (2.34) is shown around the temperature $T = 0.3 \text{ GeV} > T > 0.15 \text{ GeV}$ for different masses of bottom quarks. In all cases we see prolonged non-equilibrium, this happens since the decay and reformation rates of bottom quarks are comparable to each other as we have noted in Fig. 2.3 where both lines cross. One of the key results shown in Fig. 2.4 is that the smaller mass of bottom quark slows the strong interaction formation rate to the value of weak interaction decays just near the phase transformation of QGP to HG phase. Finally, the stationary fugacity corresponds to the reversible reactions in the stationary Universe. In this case, there is no arrow in time for bottom quark because of the detailed balance.

Non-stationary correction in expanding Universe

The Universe is expanding and temperature is a function of time. In this section we now consider the fugacity as a function of time and study the correction in fugacity due to the expanding Universe. In general, the fugacity of bottom quark can be written as

$$\Upsilon_b = \Upsilon_{st} + \Upsilon_{st}^{\text{non}} = \Upsilon_{st}(1 + x), \quad x \equiv \Upsilon_{st}^{\text{non}}/\Upsilon_{st}, \quad (2.35)$$

where the variable x corresponds to the correction due to non-stationary Universe. Substituting the general solution Eq.(2.35) into differential equation Eq.(2.31), we

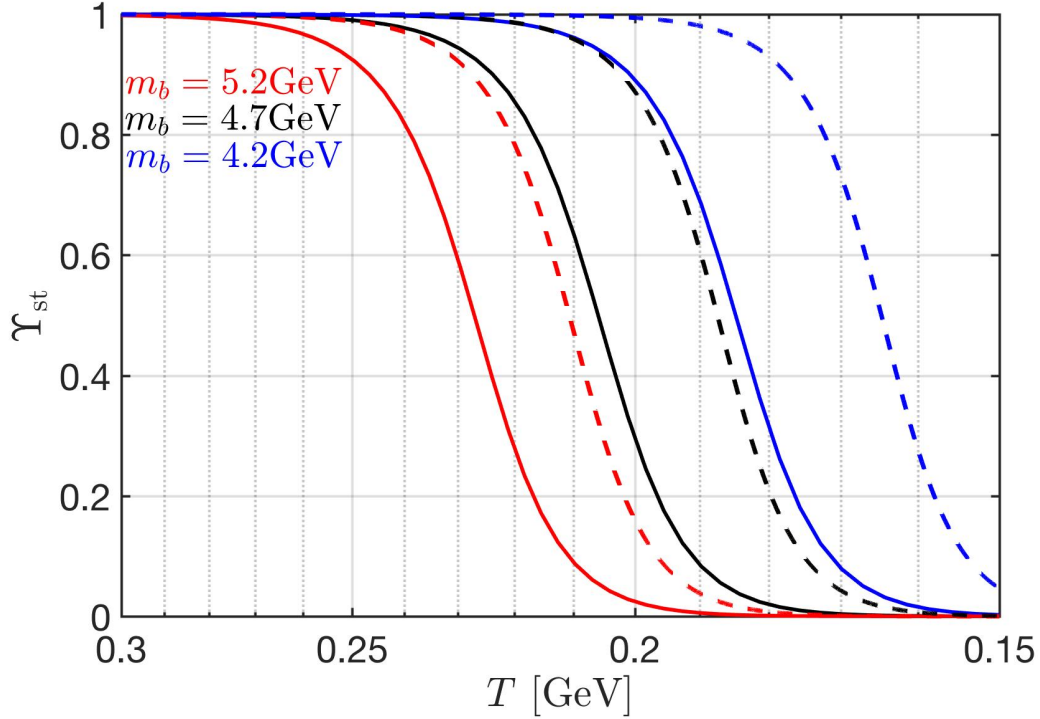


Figure 2.4: The fugacity of free/ bounded bottom quark as a function of temperature in the early Universe for $m_b = 4.2$ GeV (blue), $m_b = 4.7$ GeV (black), and $m_b = 5.2$ GeV (red). The solid lines represent the case bottom quark bound into B_c mesons, and the dashed lines label the case of free bottom quark.

obtain

$$\frac{dx}{dt} = -x^2 \frac{\Upsilon_{st}}{\tau_{source}} - x \left[\frac{1}{\tau_{eff}} + 3H - \frac{1}{\tau_T} \right] - \left[\frac{d \ln \Upsilon_{st}}{dt} + 3H - \frac{1}{\tau_T} \right], \quad (2.36)$$

where the effective relaxation time $1/\tau_{eff}$ is defined as

$$\frac{1}{\tau_{eff}} \equiv \left[\frac{2\Upsilon_{st}}{\tau_{source}} + \frac{1}{\tau_{decay}} + \frac{d \ln \Upsilon_{st}}{dt} \right]. \quad (2.37)$$

In Fig. 2.5 we see that when temperature is near to $T = 0.2$ GeV, we have $1/\tau_{eff} \approx 10^7 H$, and $1/\tau_{eff} \approx 10^5/\tau_T$. In this case, the last two terms in Eq. (2.36) compare to $1/\tau_{eff}$ can be neglected, and the differential equation becomes

$$\frac{dx}{dt} = -\frac{x^2 \Upsilon_{st}}{\tau_{source}} - \frac{x}{\tau_{eff}} - \left[\frac{d \ln \Upsilon_{st}}{dt} + 3H - \frac{1}{\tau_T} \right], \quad (2.38)$$

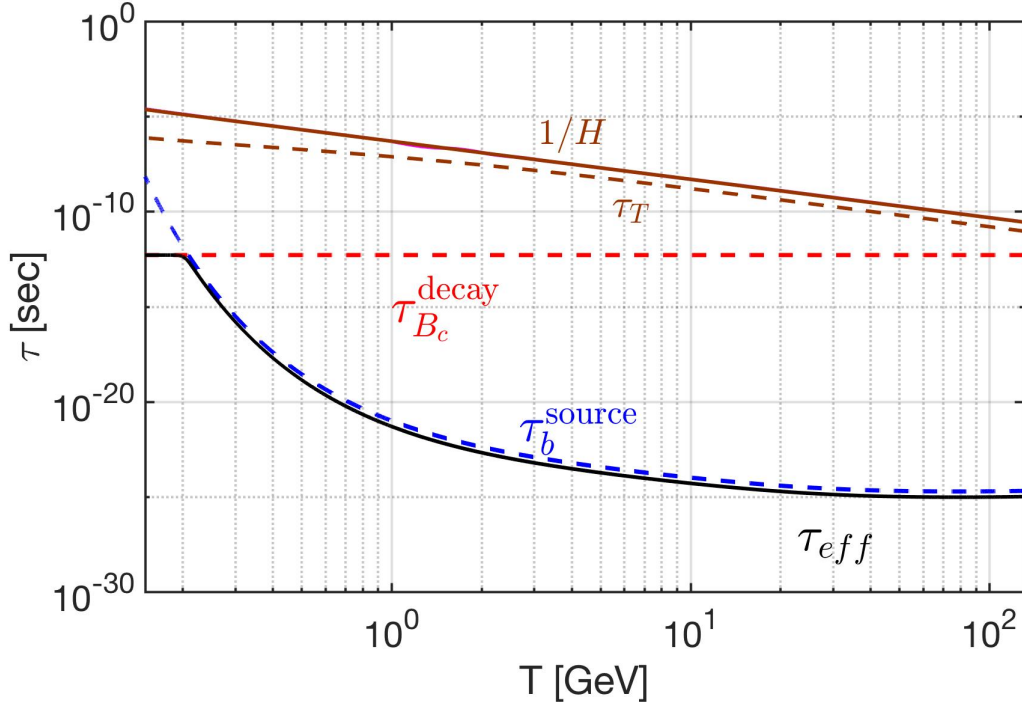


Figure 2.5: The effective relaxation time τ_{eff} as a function of temperature in the early Universe for bottom mass $m_b = 4.7\text{GeV}$. For comparison, we also plot the vacuum lifespan of B_c meson $\tau_{B_c}^{decay}$ (red dashed-line), the relaxation time for bottom production τ_{source}^b (blue dashed-line), Hubble expansion time $1/H$ (brown solid line) and relaxation time for temperature cooling τ_T (brown dashed-line).

To solve the variable x we consider the case $dx/dt, x^2 \ll 1$ first, we neglect the terms dx/dt and x^2 in Eq. (2.38) then solve the linear fugacity equation. We will establish that these approximations are justified by checking the magnitude of the solution. Neglecting terms dx/dt and x^2 in Eq. (2.38) we obtain

$$x \approx \tau_{eff} \left[\frac{d \ln \Upsilon_{st}}{dt} + 3H - \frac{1}{\tau_T} \right]. \quad (2.39)$$

It is convenient to change the variable from time to temperature. For an isentropically-expanding universe, we have

$$\frac{dt}{dT} = -\frac{\tau_H^*}{T}, \quad \tau_H^* = \frac{1}{H} \left(1 + \frac{T}{3g_*^s} \frac{dg_*^s}{dT} \right). \quad (2.40)$$

In this case, we have

$$x = \tau_{eff} \left[\frac{1}{\Upsilon_{st}} \frac{d\Upsilon_{st}}{dT} \frac{T}{\tau_H^*} + 3H - \frac{1}{\tau_T} \right]. \quad (2.41)$$

Finally, we can obtain the nonstationary fugacity by multiplying the fugacity ratio x with Υ_{st} , giving

$$\Upsilon_{st}^{\text{non}} \approx \left(\frac{\tau_{eff}}{\tau_H^*} \right) \left[\frac{d\Upsilon_{st}}{dT} T - \Upsilon_{st} \left(3H\tau_H^* - \frac{\tau_H^*}{\tau_T} \right) \right]. \quad (2.42)$$

In Fig. 2.6 we plot the nonstationary $\Upsilon_{st}^{\text{non}}$ as a function of temperature. The nonstationary fugacity $\Upsilon_{st}^{\text{non}}$ follows the behavior of $d\Upsilon_{st}/dT$, which corresponds to the irreversible process in expanding Universe. In this case, the irreversible nonequilibrium process creates the arrow in time for bottom quark in the Universe. The large value of Hubble time compares to the effective relaxation time suppressing the value of nonstationary fugacity to $\mathcal{O} \sim 10^{-7}$, which shows that the neglecting $dx/dt, x^2 \ll 1$ is a good approximation for solving the non-stationary fugacity in the early Universe.

To conclude this chapter, we have demonstrated that the bottom quark nonequilibrium occurs near the QGP phase transition around the temperature $T = 0.3 \sim 0.15$ GeV in Fig. 2.4 and Fig. 2.6. We show the competition between weak interaction decay and the strong interaction $g + g \rightarrow b + \bar{b}$, $q + \bar{q} \rightarrow b + \bar{b}$ fusion processes drive the bottom quark departure from the equilibrium and create the arrow of time in the early Universe at relatively low QGP temperature. The results provide a strong motive for exploring the physics of baryon nonconservation involving the bottomonium mesons or/and bottom quarks in a thermal environment.

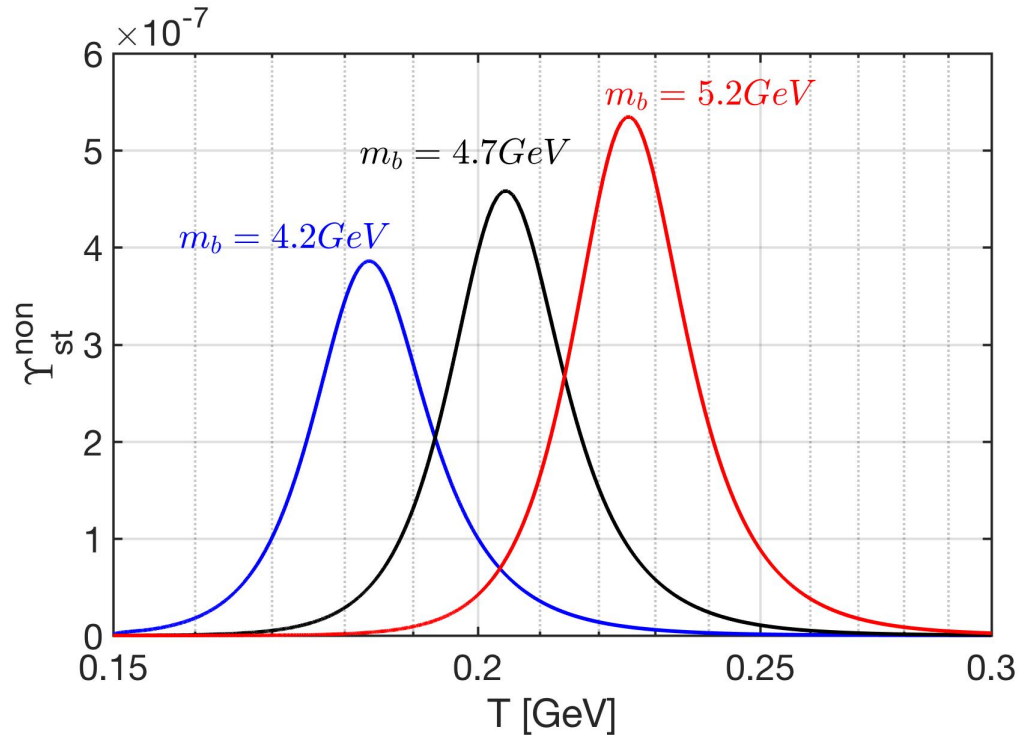


Figure 2.6: The non-stationary fugacity $\Upsilon_{st}^{\text{non}}$ as a function of temperature in the Universe for different bottom mass $m_b = 4.2 \text{ GeV}$ (blue), $m_b = 4.7 \text{ GeV}$ (black), and $m_b = 5.2 \text{ GeV}$ (red) for the case bottom quarks bound into B_c mesons.

CHAPTER 3

Strangeness abundance in cosmic plasma

As the Universe expanded and cooled down to the hadronization temperature $T_H \approx 150$ MeV, the primordial QGP underwent a phase transformation called hadronization. This transition resulted in the confinement of the strong force, causing quarks and gluons to combine and form matter and antimatter. After hadronization, one may think the relatively short lived massive hadrons decay rapidly and disappear from the Universe. However, the most abundant hadrons, pions $\pi(q\bar{q})$, can be produced via their inverse decay process $\gamma\gamma \rightarrow \pi^0$ and retain their chemical equilibrium until temperature $T = 3 \sim 5$ MeV [Kuznetsova et al. (2008)].

Following the idea and the framework presented by [Kuznetsova et al. (2008)], we investigate the strange particle composition of the expanding early Universe in the epoch $150 \text{ MeV} \geq T \geq 10 \text{ MeV}$, and examine the freeze-out temperature for strangeness-producing by comparing the relevant reaction rates to the Hubble expansion rate. We show that strangeness is kept in equilibrium via weak, electromagnetic, and strong interactions in the early Universe until $T \approx 13$ MeV.

3.1 Chemical equilibrium in the hadronic Universe

In this section, we explore the Universe composition assuming both kinetic and particle abundance equilibrium (chemical equilibrium) by considering the charge neutrality and prescribed conserved baryon-per-entropy-ratio $(n_B - n_{\bar{B}})/\sigma$ to determine the baryon chemical potential μ_B [Fromerth et al. (2012); Rafelski and Birrell (2014)]. With the chemical potential as a function of temperature, we can obtain the particle number densities for different species and study their composition in the early Universe.

We improve the prior work [Fromerth et al. (2012)] by considering the conserved

entropy per baryon ratio with conservation of strangeness in the early Universe. To study the baryon and strange quark chemical potential, it is convenient to introduce the chemical fugacity for strangeness λ_s and quark λ_q as follows:

$$\lambda_s = \exp(\mu_s/T) \quad \lambda_q = \exp(\mu_B/3T), \quad (3.1)$$

where μ_s and μ_B are the chemical potential of strangeness and baryon, respectively. For the quark fugacity λ_q , we divide the chemical potential of baryons by 3 as an approximation for quark chemical potential. Imposing the conservation of strangeness $\langle s - \bar{s} \rangle = 0$, we have, when the baryon chemical potential does not vanish the chemical potential of strangeness in the early Universe satisfying (see Section 11.5 in [Letessier and Rafelski (2002)])

$$\lambda_s = \lambda_q \sqrt{\frac{F_K + \lambda_q^{-3} F_Y}{F_K + \lambda_q^3 F_Y}}. \quad (3.2)$$

where we employ the phase-space function F_i for sets of nucleon N , kaon K , and hyperon Y particles defined as (see [Letessier and Rafelski (2002)], Section 11.4):

$$F_N = \sum_{N_i} g_{N_i} W(m_{N_i}/T), \quad N_i = n, p, \Delta(1232), \quad (3.3)$$

$$F_K = \sum_{K_i} g_{K_i} W(m_{K_i}/T), \quad K_i = K^0, \bar{K}^0, K^\pm, K^*(892), \quad (3.4)$$

$$F_Y = \sum_{Y_i} g_{Y_i} W(m_{Y_i}/T), \quad Y_i = \Lambda, \Sigma^0, \Sigma^\pm, \Sigma(1385), \quad (3.5)$$

where g_{N_i, K_i, Y_i} are the degenerate factors, $W(x) = x^2 K_2(x)$ with K_2 is the modified Bessel functions of integer order "2".

Considering the Boltzmann approximation for the massive particle number density we have

$$n_N = \frac{T^3}{2\pi^2} \lambda_q^3 F_N, \quad n_{\bar{N}} = \frac{T^3}{2\pi^2} \lambda_q^{-3} F_N, \quad (3.6)$$

$$n_K = \frac{T^3}{2\pi^2} (\lambda_s \lambda_q^{-1}) F_K, \quad n_{\bar{K}} = \frac{T^3}{2\pi^2} (\lambda_s^{-1} \lambda_q) F_K, \quad (3.7)$$

$$n_Y = \frac{T^3}{2\pi^2} (\lambda_q^2 \lambda_s) F_Y, \quad n_{\bar{Y}} = \frac{T^3}{2\pi^2} (\lambda_q^{-2} \lambda_s^{-1}) F_Y. \quad (3.8)$$

In this case, the net baryon density in the early Universe with temperature range $150 \text{ MeV} > T > 10 \text{ MeV}$ can be written as

$$\begin{aligned}
\frac{(n_B - n_{\bar{B}})}{\sigma} &= \frac{1}{\sigma} [(n_p - n_{\bar{p}}) + (n_n - n_{\bar{n}}) + (n_Y - n_{\bar{Y}})] \\
&= \frac{T^3}{2\pi^2 \sigma} [(\lambda_q^3 - \lambda_q^{-3}) F_N + (\lambda_q^2 \lambda_s - \lambda_q^{-2} \lambda_s^{-1}) F_Y] \\
&= \frac{T^3}{2\pi^2 \sigma} (\lambda_q^3 - \lambda_q^{-3}) F_N \left[1 + \frac{\lambda_s}{\lambda_q} \left(\frac{\lambda_q^3 - \lambda_q^{-1} \lambda_s^{-2}}{\lambda_q^3 - \lambda_q^{-3}} \right) \frac{F_Y}{F_N} \right] \\
&\approx \frac{T^3}{2\pi^2 \sigma} (\lambda_q^3 - \lambda_q^{-3}) F_N \left[1 + \frac{\lambda_s}{\lambda_q} \frac{F_Y}{F_N} \right], \tag{3.9}
\end{aligned}$$

where we can neglect the term F_Y/F_K in the expansion of Eq.(3.2) in our temperature range. Introducing the strangeness $\langle s - \bar{s} \rangle = 0$ constraint and using the entropy density in early universe, the explicit relation for baryon to entropy ratio becomes

$$\frac{n_B - n_{\bar{B}}}{\sigma} = \frac{45}{2\pi^4 g_*^s} \sinh \left[\frac{\mu_B}{T} \right] F_N \times \left[1 + \frac{F_Y}{F_N} \sqrt{\frac{1 + e^{-\mu_B/T} F_Y/F_K}{1 + e^{\mu_B/T} F_Y/F_K}} \right]. \tag{3.10}$$

Governing Eq. (3.10) is the present-day baryon-per-entropy-ratio, and we obtain the value

$$\frac{n_B - n_{\bar{B}}}{\sigma} = \frac{n_B - n_{\bar{B}}}{\sigma} \Big|_{t_0} = (0.865 \pm 0.008) \times 10^{-10}. \tag{3.11}$$

For a detailed evaluation method we refer to this earlier work now using a baryon-to-photon ratio [Tanabashi et al. (2018)]: $(n_B - n_{\bar{B}})/n_\gamma = (0.609 \pm 0.06) \times 10^{-9}$, as well as the entropy per particle for a massless boson $\sigma/n|_{\text{boson}} \approx 3.60$ and a massless fermion $\sigma/n|_{\text{fermion}} \approx 4.20$.

We solve Eq. (3.2) and Eq (3.10) numerically to obtain baryon and strangeness chemical potentials as a function of temperature in Fig. 3.1. The chemical potential changes dramatically in the temperature window $50 \text{ MeV} \leq T \leq 30 \text{ MeV}$, its behavior describing the process of antibaryon disappearance. Substituting the chemical potential λ_q and λ_s into particle density Eq. (3.6), Eq. (3.7), and Eq. (3.8), we can obtain the particle number densities for different species as a function of temperature.

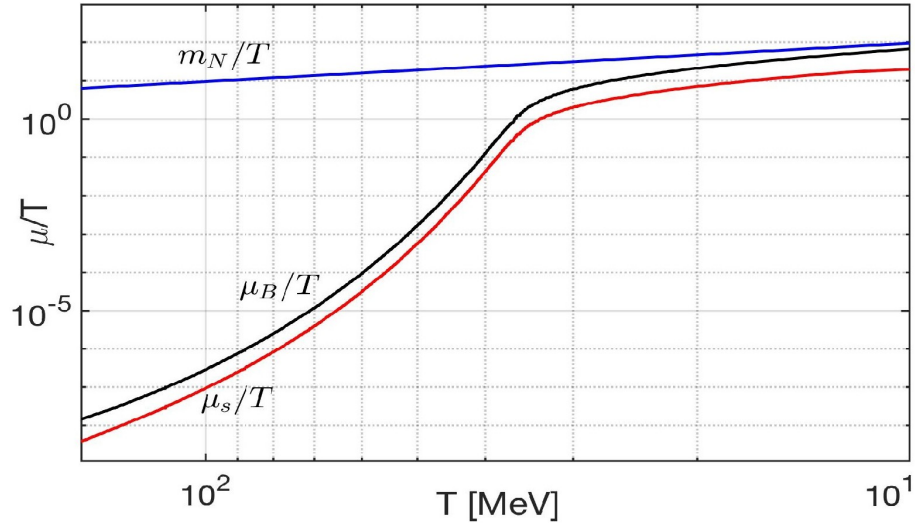


Figure 3.1: The chemical potential of baryon μ_B/T and strangeness μ_s/T as a function of temperature $150 \text{ MeV} > T > 10 \text{ MeV}$ in the early Universe; for comparison we show m_N/T with $m_N = 938.92 \text{ MeV}$, the average nucleon mass.

In Fig. 3.2 we plot the number density of baryon and antibaryon as a function of temperature. We consider that when the $n_{\bar{B}} \ll (n_B - n_{\bar{B}})$ the antibaryons density is sufficiently low and disappear from the Universe inventory quickly. To determine the temperature where antibaryons are sufficiently low in the Universe inventory we defined the condition when the ratio $n_{\bar{B}}/(n_B - n_{\bar{B}}) = 1$. This condition is reached in an expanding Universe at $T = 38.2 \text{ MeV}$, which is in agreement with the qualitative result in [Kolb and Turner (1990a)]. After this temperature, the net baryon density dilutes with a residual co-moving conserved quantity determined by the observed baryon asymmetry.

In Fig. 3.3 we show examples of particle abundance ratios of interest. Pions $\pi(q\bar{q})$ are the most abundant hadrons $n_\pi/n_B \gg 1$, because of their low mass and the reaction $\gamma\gamma \rightarrow \pi^0$, which assures chemical yield equilibrium [Kuznetsova et al. (2008)]. For $150 \text{ MeV} > T > 20.8 \text{ MeV}$, we see the ratio $n_{\bar{K}(\bar{q}s)}/n_B \gg 1$, which implies pair abundance of strangeness is more abundant than baryons, and is dominantly present in mesons, since $n_{\bar{K}}/n_Y \gg 1$. For $20.8 \text{ MeV} > T$, the baryon becomes dominant $n_{\bar{K}}/n_B < 1$, which implies that the strange meson is embedded in a large

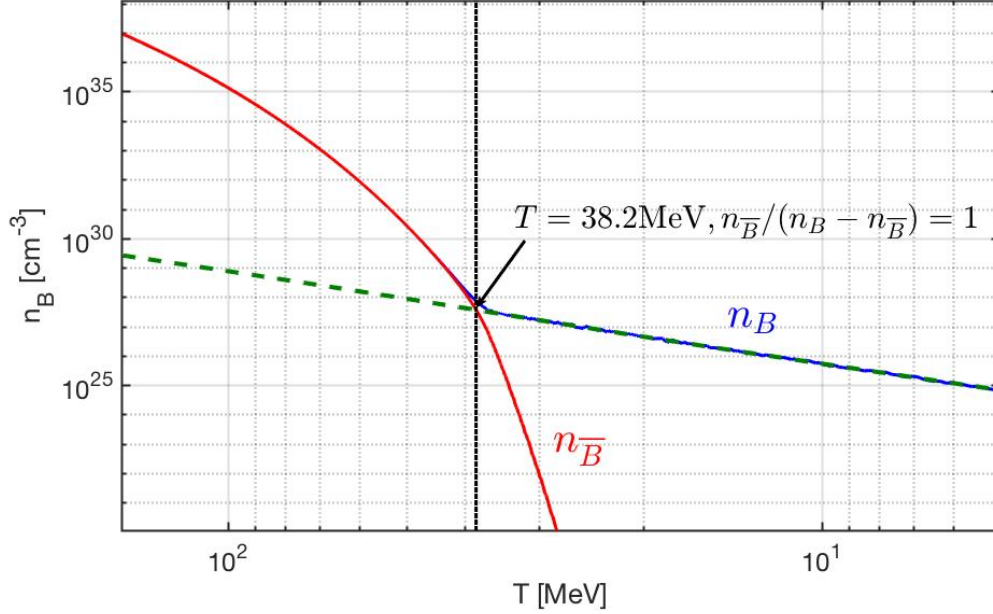


Figure 3.2: The baryon (blue solid line) and antibaryon (red solid line) number density as a function of temperature in the range $150 \text{ MeV} > T > 5 \text{ MeV}$. The green dashed line is the extrapolated value for baryon density. The temperature $T = 38.2 \text{ MeV}$ (black dashed vertical line) is denoted when the ratio $n_{\bar{B}} / (n_B - n_{\bar{B}}) = 1$ which defines the condition where antibaryons disappear from the Universe.

background of baryons, and the exchange reaction $\bar{K} + N \rightarrow \Lambda + \pi$ can re-equilibrate kaons and hyperons in the temperature range; therefore strangeness symmetry $s = \bar{s}$ is maintained. For $12.9 \text{ MeV} > T$ we have $n_Y/n_B > n_{\bar{K}}/n_B$, now the still existent tiny abundance of strangeness is found predominantly in hyperons.

3.2 Seeking strangeness freeze-out chemical nonequilibrium

This section considers an unstable strange particle S decaying into two particles 1 and 2, which themselves have no strangeness content. In a dense and high-temperature plasma with particles 1 and 2 in thermal equilibrium, the inverse reaction populates the system with particle S . This is written schematically as

$$S \rightleftharpoons 1 + 2, \quad \text{Example : } K^0 \rightleftharpoons \pi + \pi. \quad (3.12)$$

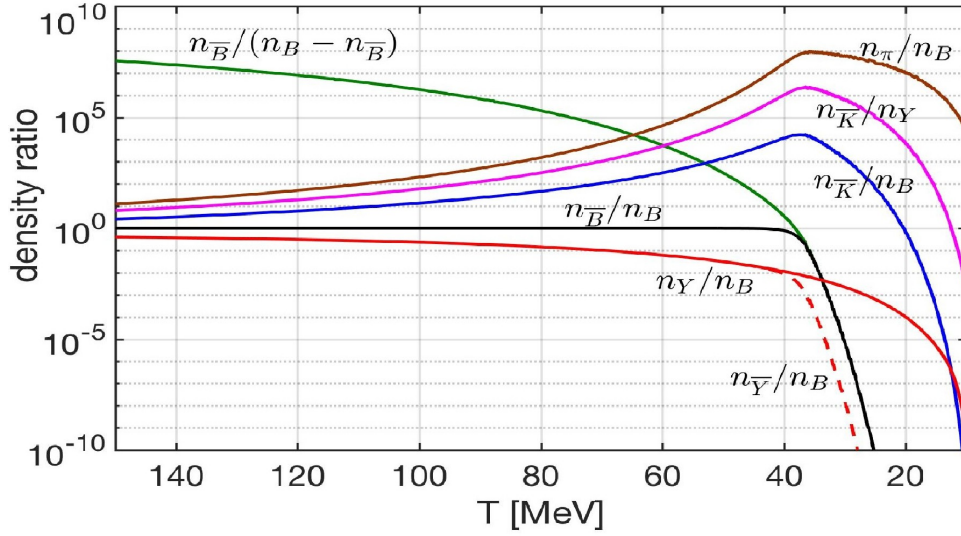


Figure 3.3: Ratios of hadronic particle number densities as a function of temperature $150 \text{ MeV} > T > 10 \text{ MeV}$ in the early Universe, with baryon B yields: pions π (brown line), kaons $K(q\bar{s})$ (blue), antibaryon \bar{B} (black), hyperon Y (red) and anti-hyperons \bar{Y} (dashed red). Also shown \bar{K}/Y (purple).

The natural decay of the daughter particles provides the intrinsic strength of the inverse strangeness production reaction rate. As long as both decay and production reactions are possible, particle S abundance remains in thermal equilibrium. This balance between production and decay rates is called a detailed balance.

Once the primordial Universe expansion rate $1/H$ overwhelms the strongly temperature dependent back-reaction and the back reaction freeze-out, then the decay $S \rightarrow 1 + 2$ occurs out of balance and particle S disappears from the inventory. The two-on-two strangeness producing reactions have a significantly higher strangeness production reaction threshold, thus especially near to strangeness decoupling their influence is negligible. Such reactions are more important near the QGP hadronization temperature $T_H \simeq 150 \text{ MeV}$, and they characterize strangeness exchange reactions such as $K + N \leftrightarrow \Lambda + \pi$, (see Chapter 18 in [Letessier and Rafelski (2002)]).

In Fig. 3.4 we show reactions relevant to strangeness evolution in the considered Universe evolution epoch $150 \text{ MeV} \geq T \geq 10 \text{ MeV}$ and their pertinent reaction strength. As shown:

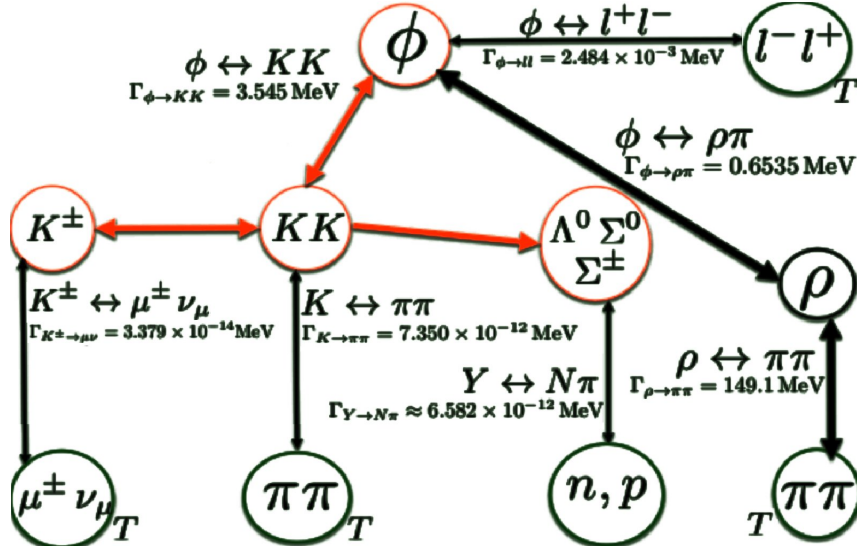


Figure 3.4: The strangeness abundance changing reactions in the primordial Universe. The red circles show strangeness carrying hadronic particles; red thick lines denote effectively instantaneous reactions. Black thick lines show relatively strong hadronic reactions. The reaction rates required to describe strangeness time evolution are shown in [Rafelski and Yang (2022)].

- We study strange quark abundance in baryons and mesons, considering both open and hidden strangeness (hidden: $s\bar{s}$ -content). Important source reactions are $l^- + l^+ \rightarrow \phi$, $\rho + \pi \rightarrow \phi$, $\pi + \pi \rightarrow K_S$, $\Lambda \leftrightarrow \pi + N$, and $\mu^\pm + \nu \rightarrow K^\pm$.
- Muons and pions are coupled through electromagnetic reactions $\mu^+ + \mu^- \leftrightarrow \gamma + \gamma$ and $\pi \leftrightarrow \gamma + \gamma$ to the photon background and retain their chemical equilibrium until the temperature $T = 4 \text{ MeV}$ and $T = 5 \text{ MeV}$, respectively [Rafelski and Yang (2021); Kuznetsova et al. (2008)]. The large $\phi \leftrightarrow K + K$ rate assures ϕ and K are in relative chemical equilibrium.

In order to determine where exactly strangeness disappears from the Universe inventory, we explore the magnitudes of different rates of production and decay processes in mesons and hyperons.

3.2.1 Strangeness creation/annihilation rate in mesons

From Fig. 3.4 in the meson domain, the relevant interaction rates competing with Hubble time are the reactions

$$\pi + \pi \leftrightarrow K, \quad \mu^\pm + \nu \leftrightarrow K^\pm, \quad l^+ + l^- \leftrightarrow \phi, \quad (3.13)$$

$$\rho + \pi \leftrightarrow \phi, \quad \pi + \pi \leftrightarrow \rho. \quad (3.14)$$

The thermal reaction rate per time and volume for two body-to-one particle reactions $1 + 2 \rightarrow 3$ has been presented before [Koch et al. (1986); Kuznetsova et al. (2008); Kuznetsova and Rafelski (2010a)]. In full kinetic and chemical equilibrium, the reaction rate per time per volume can be written as [Kuznetsova and Rafelski (2010a)] :

$$R_{12 \rightarrow 3} = \frac{g_3}{(2\pi)^2} \frac{m_3}{\tau_3^0} \int_0^\infty \frac{p_3^2 dp_3}{E_3} \frac{e^{E_3/T}}{e^{E_3/T} \pm 1} \Phi(p_3), \quad (3.15)$$

where τ_3^0 is the vacuum lifetime of particle 3. The positive sign “+” is for the case when particle 3 is a boson, and negative sign “−” for fermion. The function $\Phi(p_3)$ for the non-relativistic limit $m_3 \gg p_3, T$ can be written as

$$\Phi(p_3 \rightarrow 0) = 2 \frac{1}{(e^{E_1/T} \pm 1)(e^{E_2/T} \pm 1)}. \quad (3.16)$$

Considering the Boltzmann limit, the thermal reaction rate per unit time and volume becomes

$$R_{12 \rightarrow 3} = \frac{g_3}{2\pi^2} \left(\frac{T^3}{\tau_3^0} \right) \left(\frac{m_3}{T} \right)^2 K_1(m_3/T), \quad (3.17)$$

where K_1 is the modified Bessel functions of integer order “1”. In order to compare the reaction time with Hubble time $1/H$, it is convenient to define the relaxation time for the process $1 + 2 \rightarrow 3$ as follows:

$$\tau_{12 \rightarrow 3} \equiv \frac{n_1^{eq}}{R_{12 \rightarrow 3}}, \quad n_1^{eq} = \frac{g_1}{2\pi^2} \int_{m_1}^\infty dE \frac{E \sqrt{E^2 - m_1^2}}{\exp(E/T) \pm 1}, \quad (3.18)$$

where n_1^{eq} is the thermal equilibrium number density of particle 1 with the ‘heavy’ mass $m_1 > T$. Combining Eq. (3.17) with Eq. (3.18) we obtain

$$\frac{\tau_{12 \rightarrow 3}}{\tau_3^0} = \frac{2\pi^2 n_1^{eq} / T^3}{g_3 (m_3/T)^2 K_1(m_3/T)}, \quad n_1^{eq} \simeq g_1 \left(\frac{m_1 T}{2\pi} \right)^{3/2} e^{-m_1/T}, \quad (3.19)$$

where, conveniently, the relaxation time does not depend on the abundant and often relativistic heat bath component 2, *e.g.* l^\pm, π, ν, γ . The density of heavy particles 1 and 3 can in general be well approximated using the leading and usually nonrelativistic Boltzmann term as shown above.

In general, the reaction rates for inelastic collision process capable of changing particle number, for example $\pi\pi \rightarrow K^0$, is suppressed by the factor $\exp(-m_{K^0}/T)$. On the other hand, there is no suppression for the elastic momentum and energy exchanging particle collisions in plasma. We conclude that for the case $m \gg T$, the dominant collision term in the relativistic Boltzmann equation is the elastic collision term, keeping all heavy particles in kinetic energy equilibrium with the plasma. This allows us to study the particle abundance in plasma presuming the energy-momentum statistical distribution equilibrium exists. This insight was discussed in detail in the preparatory phase of laboratory exploration of hot hadron and quark matter, see [Koch et al. (1986)]. In order to study the particle abundance in the Universe when $m \gg T$, instead of solving the exact Boltzmann equation, we can separate the fast energy-momentum equilibrating collisions from the slow particle number changing inelastic collisions. In the following we explore the rates of inelastic collision and compare the relaxation times of particle production in all relevant reactions with the Universe expansion rate.

It is common to refer to particle freeze-out as the epoch where a given type of particle ceases to interact with other particles. In this situation the particle abundance decouples from the cosmic plasma, a chemical nonequilibrium and even complete abundance disappearance of this particle can happen; the condition for the given reaction $1 + 2 \rightarrow 3$ to decouple is

$$\tau_{12 \rightarrow 3}(T_f) = 1/H(T_f), \quad (3.20)$$

where T_f is the freeze-out temperature. In the epoch of interest, $150 \text{ MeV} > T > 10 \text{ MeV}$, the Universe is dominated by radiation and effectively massless matter behaving like radiation. The Hubble parameter can be written as [Kolb and Turner

(1990b)]

$$H^2 = H_{rad}^2 \left(1 + \frac{\rho_{\pi, \mu, \rho}}{\rho_{rad}} + \frac{\rho_{strange}}{\rho_{rad}} \right) = \frac{8\pi^3 G_N}{90} g_*^e T^4, \quad H_{rad}^2 = \frac{8\pi G_N \rho_{rad}}{3}, \quad (3.21)$$

where: g_*^e is the total number of effective relativistic ‘energy’ degrees of freedom; G_N is the Newtonian constant of gravitation; the ‘radiation’ energy density includes $\rho_{rad} = \rho_\gamma + \rho_\nu + \rho_{e^\pm}$ for photons, neutrinos, and massless electrons(positrons). The massive-particle correction is $\rho_{\pi, \mu, \rho} = \rho_\pi + \rho_\mu + \rho_\rho$; and at highest T of interest, also of (minor) relevance, $\rho_{strange} = \rho_{K^0} + \rho_{K^\pm} + \rho_{K^*} + \rho_\eta + \rho_{\eta'}$.

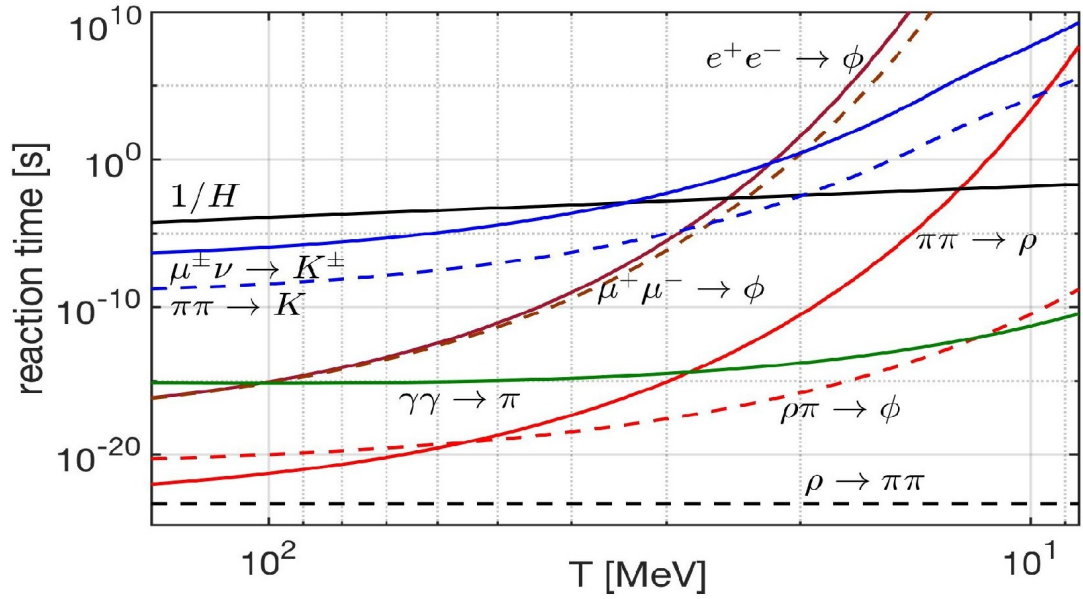


Figure 3.5: Hadronic relaxation reaction times, see Eq. (3.18), as a function of temperature T , are compared to Hubble time $1/H$ (black solid line). At bottom the horizontal black-dashed line is the natural (vacuum) lifespan of ρ .

When presenting the reaction rates and quoting decoupling as a function of temperature T , we must remember that for a temperature range $50 \text{ MeV} > T > 5 \text{ MeV}$, we have $10^{-1} < dT/dt < 10^{-4} \text{ MeV}/\mu\text{s}$. We estimate the width of freezeout temperature interval ΔT_f as follows:

$$\frac{1}{\Delta T_f} \equiv \left[\frac{1}{(\Gamma_{12 \rightarrow 3}/H)} \frac{d(\Gamma_{12 \rightarrow 3}/H)}{dT} \right]_{T_f}, \quad \Gamma_{12 \rightarrow 3} \equiv \frac{1}{\tau_{12 \rightarrow 3}}. \quad (3.22)$$

Reactions	Freeze-out Temperature (MeV)	ΔT_f (MeV)
$\mu^\pm \nu \rightarrow K^\pm$	$T_f = 33.8 \text{ MeV}$	3.5 MeV
$e^+ e^- \rightarrow \phi$	$T_f = 24.9 \text{ MeV}$	0.6 MeV
$\mu^+ \mu^- \rightarrow \phi$	$T_f = 23.5 \text{ MeV}$	0.6 MeV
$\pi\pi \rightarrow K$	$T_f = 19.8 \text{ MeV}$	1.2 MeV
$\pi\pi \rightarrow \rho$	$T_f = 12.3 \text{ MeV}$	0.2 MeV

Table 3.1: The characteristic strangeness reaction and their freeze-out temperature and temperature width in early Universe.

Using Eq.(3.21) and Eq.(3.19) and considering the temperature range $50 \text{ MeV} > T > 5 \text{ MeV}$ with $g_*^e \approx \text{constant}$ we obtain using the Boltzmann approximation to describe the massive particles 1 and 3

$$\frac{\Delta T_f}{T_f} \approx \frac{T_f}{m_3 - m_1 - 2T_f}, \quad m_3 - m_1 \gg T_f. \quad (3.23)$$

The width of freeze-out is shown in the right column in Table 3.1. We see a range of 2-10%. Therefore it is justified to consider as a decoupling condition in time the value of temperature at which the pertinent rate cross the Hubble expansion rate, see Fig. 3.5.

In Fig. 3.5 we plot the hadronic reaction relaxation times τ_i in the meson sector as a function of temperature compared to Hubble time $1/H$. It shows that the weak interaction reaction $\mu^\pm + \nu_\mu \rightarrow K^\pm$ becomes slower compared to the Universe expansion near temperature $T_f^{K^\pm} = 33.8 \text{ MeV}$, signaling the onset of abundance nonequilibrium for K^\pm . For $T < T_f^{K^\pm}$, the reactions $\mu^\pm + \nu_\mu \rightarrow K^\pm$ decouples from the cosmic plasma; the corresponding detailed balance can be broken and the decay reactions $K^\pm \rightarrow \mu^\pm + \nu_\mu$ are acting like a (small) ‘‘hole’’ in the strangeness abundance ‘‘pot’’. If other strangeness production reactions did not exist, strangeness would disappear as the Universe cools below $T_f^{K^\pm}$. However, we have other reactions: $l^+ + l^- \leftrightarrow \phi$, $\pi + \pi \leftrightarrow K$, and $\rho + \pi \leftrightarrow \phi$ can still produce the strangeness in cosmic plasma and the rate is very large compared to the weak interaction decay.

In Table 3.1 we show the characteristic strangeness reactions and their freeze-out temperatures in the early Universe. The intersection of strangeness reaction times with $1/H$ occurs for $l^- + l^+ \rightarrow \phi$ at $T_f^\phi = 25 \sim 23 \text{ MeV}$, and for $\pi + \pi \rightarrow K$ at

$T_f^K = 19.8 \text{ MeV}$, for $\pi + \pi \rightarrow \rho$ at $T_f^\rho = 12.3 \text{ MeV}$. The reactions $\gamma + \gamma \rightarrow \pi$ and $\rho + \pi \leftrightarrow \phi$ are faster compared to $1/H$. However, the $\rho \rightarrow \pi + \pi$ lifetime (black dashed line in Fig. 3.5) is smaller than the reaction $\rho + \pi \leftrightarrow \phi$; in this case, most of ρ -meson decays faster, thus are absent and cannot contribute to the strangeness creation in the meson sector. Below the temperature $T < 20 \text{ MeV}$, all the detail balances in the strange meson reactions are broken and the strangeness in the meson sector should disappear rapidly, were it not for the small number of baryons present in the Universe.

3.2.2 Strangeness production/ exchange rate in hyperons

In order to understand strangeness in hyperons in the baryonic domain, we now consider the strangeness production reaction $\pi + N \rightarrow K + \Lambda$, the strangeness exchange reaction $\bar{K} + N \rightarrow \Lambda + \pi$; and the strangeness decay $\Lambda \rightarrow N + \pi$. The competition between different strangeness reactions allows strange hyperons and antihyperons to influence the dynamic nonequilibrium condition, including development of $\langle s - \bar{s} \rangle \neq 0$.

To evaluate the reaction rate in two-body reaction $1+2 \rightarrow 3+4$ in the Boltzmann approximation we can use the reaction cross section $\sigma(s)$ and the relation [Letessier and Rafelski (2002)]:

$$R_{12 \rightarrow 34} = \frac{g_1 g_2}{32\pi^4} \frac{T}{1 + I_{12}} \int_{s_{th}}^{\infty} ds \sigma(s) \frac{\lambda_2(s)}{\sqrt{s}} K_1(\sqrt{s}/T), \quad (3.24)$$

where K_1 is the Bessel function of order 1 and the function $\lambda_2(s)$ is defined as

$$\lambda_2(s) = [s - (m_1 + m_2)^2] [s - (m_1 - m_2)^2], \quad (3.25)$$

with m_1 and m_2 , g_1 and g_2 as the masses and degeneracy of the initial interacting particle. The factor $1/(1 + I_{12})$ is introduced to avoid double counting of indistinguishable pairs of particles; we have $I_{12} = 1$ for identical particles and $I_{12} = 0$ for others.

The thermal averaged cross sections for the strangeness production and exchange processes are about $\sigma_{\pi N \rightarrow K\Lambda} \sim 0.1 \text{ mb}$ and $\sigma_{\bar{K}N \rightarrow \Lambda\pi} = 1 \sim 3 \text{ mb}$ in the energy

range in which we are interested [Koch et al. (1986)]. The cross section can be parameterized as follows:

1) For the cross section $\sigma_{\bar{K}N \rightarrow \Lambda\pi}$ we use [Koch et al. (1986)]

$$\sigma_{\bar{K}N \rightarrow \Lambda\pi} = \frac{1}{2} (\sigma_{K^-p \rightarrow \Lambda\pi^0} + \sigma_{K^-n \rightarrow \Lambda\pi^-}) . \quad (3.26)$$

Here the experimental cross sections can be parameterized as

$$\sigma_{K^-p \rightarrow \Lambda\pi^0} = \begin{cases} 1479.53 \text{mb} \cdot \exp\left(\frac{-3.377\sqrt{s}}{\text{GeV}}\right), & \text{for } \sqrt{s_m} < \sqrt{s} < 3.2 \text{GeV} \\ 0.3 \text{mb} \cdot \exp\left(\frac{-0.72\sqrt{s}}{\text{GeV}}\right), & \text{for } \sqrt{s} > 3.2 \text{GeV} \end{cases} \quad (3.27)$$

$$\sigma_{K^-n \rightarrow \Lambda\pi^-} = 1132.27 \text{mb} \cdot \exp\left(\frac{-3.063\sqrt{s}}{\text{GeV}}\right), \text{ for } \sqrt{s} > 1.699 \text{GeV}, \quad (3.28)$$

where $\sqrt{s_m} = 1.473 \text{ GeV}$.

2) For the cross section $\sigma_{\pi N \rightarrow K\Lambda}$ we use [Cugnon and Lombard (1984)]

$$\sigma_{\pi N \rightarrow K\Lambda} = \frac{1}{4} \times \sigma_{\pi p \rightarrow K^0\Lambda} . \quad (3.29)$$

The experimental $\sigma_{\pi p \rightarrow K^0\Lambda}$ can be approximated as follows

$$\sigma_{\pi p \rightarrow K^0\Lambda} = \begin{cases} \frac{0.9 \text{mb} \cdot (\sqrt{s} - \sqrt{s_0})}{0.091 \text{GeV}}, & \text{for } \sqrt{s_0} < \sqrt{s} < 1.7 \text{GeV} \\ \frac{90 \text{MeV} \cdot \text{mb}}{\sqrt{s} - 1.6 \text{GeV}}, & \text{for } \sqrt{s} > 1.7 \text{GeV}, \end{cases} \quad (3.30)$$

with $\sqrt{s_0} = m_\Lambda + m_K$.

Given the cross sections, we obtain the thermal reaction rate per volume for strangeness exchange reaction seen in Fig. 3.6. We see that around $T = 20 \text{ MeV}$, the dominant reactions for the hyperon Λ production is $\bar{K} + N \leftrightarrow \Lambda + \pi$. At the same time, the $\pi + \pi \rightarrow K$ reaction becomes slower than Hubble time and kaon K decay rapidly in the early Universe. However, the anti-kaons \bar{K} produce the hyperon Λ because of the strangeness exchange reaction $\bar{K} + N \rightarrow \Lambda + \pi$ in the baryon-dominated Universe. We have strangeness in Λ and it disappears from the Universe via the decay $\Lambda \rightarrow N + \pi$. Both strangeness and anti-strangeness disappear

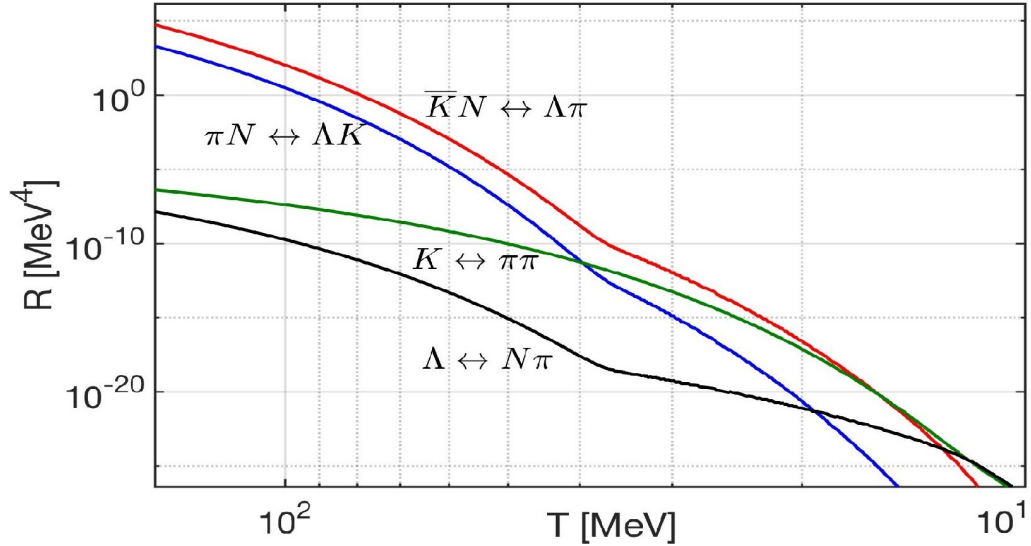


Figure 3.6: Thermal reaction rate R per volume and time for important hadronic strangeness production and exchange processes as a function of temperature $150 \text{ MeV} > T > 10 \text{ MeV}$ in the early Universe.

because of the $K \rightarrow \pi + \pi$ and $\Lambda \rightarrow N + \pi$, while the strangeness abundance $s = \bar{s}$ in the early Universe remains.

Around $T = 12.9 \text{ MeV}$, the reaction $\Lambda + \pi \rightarrow \bar{K} + N$ becomes slower than the strangeness decay $\Lambda \leftrightarrow N + \pi$ and shows that at the low temperature the Λ particles are still in equilibrium via the reaction $\Lambda \leftrightarrow N + \pi$ and little strangeness remains in the Λ . Then strangeness abundance becomes asymmetric $s \gg \bar{s}$, which implies that the assumption for strangeness conservation can only be valid until the temperature $T \sim 13 \text{ MeV}$. Below this temperature a new regime opens up in which the tiny residual strangeness abundance is governed by weak decays with no re-equilibration with mesons. Also, in view of baryon asymmetry, $\langle s - \bar{s} \rangle \neq 0$.

The primary conclusion of this first study of strangeness production and content in the early Universe, following on QGP hadronization, is that the relevant temperature domains indicate a complex interplay between baryon and meson (strange and non-strange) abundances and non-trivial decoupling from equilibrium for strange and non-strange mesons. We believe that this work contributes to the opening of a new and rich domain in the study of the Universe evolution in the future.

CHAPTER 4

Neutrinos in cosmic plasma

Neutrinos are fundamental particles and play an important role in the evolution of the Universe. In the early Universe the neutrinos are kept in equilibrium with cosmic plasma via the weak interaction. The neutrino-matter interactions play a crucial role in understanding of neutrinos evolution in the early Universe (such as the neutrino freezeout) and the later Universe (the property of today's neutrino background). In this chapter, I will examine the neutrino coherent and incoherent scattering with matter and their application in cosmology. The investigation of the relation between the effective number of neutrinos N_ν^{eff} and lepton asymmetry L after neutrino freezeout and its impact on Universe expansion is also discussed in this chapter.

4.1 Matrix element for neutrino coherent/ incoherent scattering

According to the standard model, neutrinos interact with other particles via the Charged-Current(CC) and Neutral-Current(NC) interactions. Their Lagrangian can be written as [Giunti and Kim (2007)]

$$\mathcal{L}^{CC} = \frac{g}{2\sqrt{2}} \left(j_W^\mu W_\mu + j_W^{\mu\dagger} W_\mu^\dagger \right), \quad \mathcal{L}^{NC} = -\frac{g}{2\cos\theta_w} j_Z^\mu Z_\mu, \quad (4.1)$$

where $g = e \sin\theta_w$, W^μ and Z^μ are W and Z boson gauge fields, and j_W^μ and j_Z^μ are the charged-current and neutral-current separately. In the limit of energies lower than the $W(m_w = 80 \text{ GeV})$ and $Z(m_z = 91 \text{ GeV})$ gauge bosons, the effective Lagrangians are given by

$$\mathcal{L}_{eff}^{CC} = -\frac{G_F}{\sqrt{2}} j_{W\mu}^\dagger j_W^\mu, \quad \mathcal{L}_{eff}^{NC} = -\frac{G_F}{\sqrt{2}} j_{Z\mu}^\dagger j_Z^\mu, \quad \frac{G_F}{\sqrt{2}} = \frac{g^2}{8m_W^2}, \quad (4.2)$$

where $G_F = 1.1664 \times 10^{-5} \text{ GeV}^{-2}$ is the Fermi constant, which is one of the important parameters that determine the strength of the weak interaction rate. When neutrinos interact with matter, based on the neutrino's wavelength, they can undergo two types of scattering processes: coherent scattering and incoherent scattering with the particles in the medium.

With coherent scattering, neutrinos interact with the entire composite system rather than individual particles within the system. The coherent scattering is particularly relevant for low-energy neutrinos when the wavelength of neutrino is much larger than the size of system. In 1978, Lincoln Wolfenstein pointed out that the coherent forward scattering of neutrinos off matter could be very important in studying the behavior of neutrino flavor oscillation in a dense medium [Wolfenstein (1978)]. The fact that neutrinos propagating in matter may interact with the background particles can be described by the picture of free neutrinos traveling in an effective potential.

For incoherent scattering, neutrinos interact with particles in the medium individually. Incoherent scattering is typically more prominent for high-energy neutrinos, where the wavelength of neutrino is smaller compared to the spacing between particles. Study of incoherent scattering of high-energy neutrinos is important for understanding the physics in various astrophysical systems (e.g. supernova, stellar formation) and the evolution of the early Universe.

In this section, we discuss the coherent scattering between long wavelength neutrinos and atoms, and study the effective potential for neutrino coherent interaction. Then we present the matrix elements that describe the incoherent interaction between high energy neutrinos and other fundamental particles in the early Universe. Understanding these matrix elements is crucial for comprehending the process of neutrino freeze-out in the early Universe.

4.1.1 Long wavelength limit of neutrino-atom coherent scattering

According to the standard cosmological model, the Universe today is filled with the cosmic neutrinos with temperature $T_\nu^0 = 1.9 \text{ K} = 1.7 \times 10^{-4} \text{ eV}$. The average

momentum of present-day relic neutrinos is given by $\langle p_\nu^0 \rangle \approx 3.15 T_\nu^0$ and the typical wavelength $\lambda_\nu^0 = 2\pi/\langle p_\nu^0 \rangle \approx 2.3 \times 10^5 \text{ \AA}$, which is much larger than the radius at the atomic scale, such as the Bohr radius $R_{\text{atom}} = 0.529 \text{ \AA}$. In this case we have the long wavelength condition $\lambda_\nu \gg R_{\text{atom}}$ for cosmic neutrino background today.

Under the condition $\lambda_\nu \gg R_{\text{atom}}$, when the neutrino is scattering off an atom, the interaction can be coherent scattering [Weber (1988); Lewis (1980); Papavassiliou et al. (2006)]. According to the principles of quantum mechanics, with neutrino scattering it is impossible to identify which scatters the neutrino interacts with and thus it is necessary to sum over all possible contributions. In such circumstances, it is appropriate to view the scattering reaction as taking place on the atom as a whole, i.e.,

$$\nu + \text{Atom} \longrightarrow \nu + \text{Atom}. \quad (4.3)$$

Considering a neutrino elastic scattering off an atom which is composed of Z protons, N neutrons and Z electrons. For the elastic neutrino atom scattering, the low-energy neutrinos scatter off both atomic electrons and nucleus. For nucleus parts, we consider that the neutrinos interact via the Z^0 boson with a nucleus as

$$\nu + A_N^Z \longrightarrow \nu + A_N^Z. \quad (4.4)$$

In this process a neutrino of any flavor scatters off a nucleus with the same strength. Therefore, the scattering will be insensitive to neutrino flavor. On the other hand, the neutrons can also interact via the W^\pm with nucleus as

$$\nu_l + A_N^Z \longrightarrow l^- + A_N^{Z+1}, \quad (4.5)$$

which is a quasi-elastic process for neutrino scattering with the nucleus; we have $A_N^{Z_e} \rightarrow A_N^{Z_e+1}$. Since this process will change the nucleus state into an excited one, we will not consider its effect here. For detail discussion pf quasi-elastic scattering see [Sajjad Athar et al. (2023)].

For atomic electrons, the neutrinos can interact via the Z^0 and W^\pm bosons with

electrons for different flavors, we have

$$\nu_e + e^- \longrightarrow \nu_e + e^- \quad (Z^0, W^\pm \text{ exchange}), \quad (4.6)$$

$$\nu_{\mu,\tau} + e^- \longrightarrow \nu_{\mu,\tau} + e^- \quad (Z^0 \text{ exchange}). \quad (4.7)$$

Because of the fact that the coupling of ν_e to electrons is quite different from that of $\nu_{\mu,\tau}$, one may expect large differences in the behavior of ν_e scattering compared to the other neutrino types.

Neutrino-atom coherent scattering amplitude/matrix element

This section considers how a neutrino scatters from a composite system, assumed to consist of N individual constituents at positions x_i , $i = 1, 2, \dots, N$. Due to the superposition principle, the scattering amplitude $\mathcal{M}_{\text{sys}}(\mathbf{p}', \mathbf{p})$ for scattering from an incoming momentum \mathbf{p} to an outgoing momentum \mathbf{p}' is given as the sum of the contributions from each constituent [Freedman et al. (1977); Papavassiliou et al. (2006)]:

$$\mathcal{M}_{\text{sys}}(\mathbf{p}', \mathbf{p}) = \sum_i^N \mathcal{M}_i(\mathbf{p}', \mathbf{p}) e^{i\mathbf{q}\cdot\mathbf{x}_i}, \quad (4.8)$$

where $\mathbf{q} = \mathbf{p}' - \mathbf{p}$ is the momentum transfer and the individual amplitudes $\mathcal{M}_i(\mathbf{p}', \mathbf{p})$ are added with a relative phase factor determined by the corresponding wave function. In principle, due to the presence of the phase factors, major cancellation may take place among the terms for the condition $|\mathbf{q}|R \gg 1$, where R is the size of the composite system, and the scattering would be incoherent. However, for the momentum small compared to the inverse target size, i.e., $|\mathbf{q}|R \ll 1$, then all phase factors may be approximated by unity and contributions from individual scatters add coherently.

In the case of neutrino coherent scattering with an atom: If we consider sufficiently small momentum transfer to an atom from a neutrino which satisfies the coherence condition, i.e., $|\mathbf{q}|R_{\text{atom}} \ll 1$, then the relevant phase factors have little

effect, allowing us to write the transition amplitude as [Nicolescu (2013)]

$$\mathcal{M}_{\text{atom}} = \sum_t \frac{G_F}{\sqrt{2}} [\bar{u}(p'_\nu) \gamma_\mu (1 - \gamma_5) u(p_\nu)] [\bar{u}(p'_t) \gamma^\mu (c_V^t - c_A^t \gamma^5) u(p_t)], \quad (4.9)$$

where t is all the target constituents (Z protons, N neutrons and Z electrons). The transition amplitude includes contributions from both charged and neutral currents, with

$$\text{Charged Current : } c_V^t = c_A^t = 1 \quad (4.10)$$

$$\text{Neutral Current : } c_V^t = I_3 - 2\mathcal{Q} \sin^2 \theta_w, \quad c_A^t = I_3 \quad (4.11)$$

where I_3 is the weak isospin, θ_w is the Weinberg angle, and \mathcal{Q} is the particle electric charge.

Considering the target can be regarded as an equal mixture of spin states $s_z = \pm 1/2$, and we can simplify the transition amplitude by summing the coupling constants of the constituents [Lewis (1980); Sehgal and Wanninger (1986)].

We have

$$\mathcal{M}_{\text{atom}} = \frac{G_F}{2\sqrt{2}} [\bar{u}(p'_\nu) \gamma_\mu (1 - \gamma_5) u(p_\nu)] \left[\bar{u}(p'_a) \sum_t (C_L + C_R)_t \gamma^\mu u(p_a) - \bar{u}(p'_a) \sum_t (C_L - C_R)_t \gamma^\mu \gamma^5 u(p_a) \right], \quad (4.12)$$

where the $u(p_\nu)$, $u(p'_\nu)$ are the initial and final neutrino states and $u(p_a)$, $u(p'_a)$ are the initial and final states of the target atom. The coupling coefficients C_L and C_V are defined as

$$C_L = c_V + c_A, \quad C_R = c_V - c_A, \quad (4.13)$$

where the coupling constants for neutrino scattering with proton, neutron, and electron are given by Table. 4.1. The coupling constants for $\nu_{\mu,\tau}$ are the same as for the ν_e , excepting the absence of a charged current in neutrino-electron scattering.

Given the neutrino-atom coherent scattering amplitude Eq.(4.12), the transition matrix element can be written as

$$|\mathcal{M}_{\text{atom}}|^2 = \frac{G_F^2}{8} L_{\alpha\beta}^{\text{neutrino}} \Gamma_{\text{atom}}^{\alpha\beta}, \quad (4.14)$$

	Electron (Z^0 boson)	Electron (W^\pm boson)	Proton (uud)	Neutron (udd)
C_L	$-1 + 2 \sin^2 \theta_w$	2	$1 - 2 \sin^2 \theta_w$	-1
C_R	$2 \sin^2 \theta_w$	0	$-2 \sin^2 \theta_w$	0

Table 4.1: The coupling constants for neutrino scattering with proton, neutron, and electron.

where the neutrino tensor $L_{\alpha\beta}^{\text{neutrino}}$ is given by

$$\begin{aligned} L_{\alpha\beta}^{\text{neutrino}} &= \text{Tr} \left[\gamma_\alpha (1 - \gamma_5) (\not{p}_\nu + m_\nu) \gamma_\beta (1 - \gamma_5) (\not{p}'_\nu + m_\nu) \right] \\ &= 8 \left[(p_\nu)_\alpha (p'_\nu)_\beta + (p_\nu)'_\alpha (p_\nu)_\beta - g_{\alpha\beta} (p_\nu \cdot p'_\nu) + i \epsilon_{\alpha\sigma\beta\lambda} (p_\nu)^\sigma (p'_\nu)^\lambda \right], \end{aligned} \quad (4.15)$$

and the atomic tensor $\Gamma_{\text{atom}}^{\alpha\beta}$ can be written as

$$\begin{aligned} \Gamma_{\text{atom}}^{\alpha\beta} &= \text{Tr} \left[(C_{LR} \gamma^\alpha - C'_{LR} \gamma^\alpha \gamma^5) (\not{p}_a + M_a) (C_{LR} \gamma^\beta - C'_{LR} \gamma^\beta \gamma^5) (\not{p}'_a + M_a) \right] \\ &= 4 \left\{ (C_{LR}^2 + C'^2_{LR}) [(p_a)^\alpha (p'_a)^\beta + (p_a)'^\alpha (p_a)^\beta] \right. \\ &\quad \left. - g^{\alpha\beta} [(C_{LR}^2 - C'^2_{LR}) (p_a \cdot p'_a) - (C_{LR}^2 - C'^2_{LR}) M_a^2] \right. \\ &\quad \left. + 2i C_{LR} C'_{LR} \epsilon^{\alpha\sigma\beta\lambda'} (p_a)_{\sigma'} (p'_a)^{\lambda'} \right\}, \end{aligned} \quad (4.16)$$

where M_a is the target atom's mass ($M_a = AM_{\text{nucleon}}, A = Z + N$), the coupling constants C_{LR} and C'_{LR} are defined by

$$C_{LR} = \sum_t (C_L + C_R)_t, \quad C'_{LR} = \sum_t (C_L - C_R)_t. \quad (4.17)$$

Substituting Eq.(4.15) and Eq.(4.16) into Eq.(4.14), then the transition matrix element for coherent elastic neutrino atom scattering is given by:

$$\begin{aligned} |\mathcal{M}_{\text{atom}}|^2 &= \frac{G_F^2}{8} L_{\alpha\beta}^{\text{neutrino}} \Gamma_{\text{atom}}^{\alpha\beta} \\ &= 8G_F^2 \left[(C_{LR} + C'_{LR})^2 (p_\nu \cdot p_a) (p'_\nu \cdot p'_a) + (C_{LR} - C'_{LR})^2 (p_\nu \cdot p'_a) (p'_\nu \cdot p_a) \right. \\ &\quad \left. - (C_{LR}^2 - C'^2_{LR}) M_a^2 (p_\nu \cdot p'_\nu) \right]. \end{aligned} \quad (4.18)$$

Taking the atom at rest in the laboratory frame, and considering small momentum transfer to an atom from a neutrino, i.e., $q^2 = (p_\nu - p'_\nu)^2 = (p'_a - p_a)^2 \ll M_a^2$, we have

$$p_\nu \cdot p_a = E_\nu M_a, \quad (4.19)$$

$$p'_\nu \cdot p_a = E'_\nu M_a \approx E_\nu M_a, \quad (4.20)$$

$$p'_\nu \cdot p'_a = p'_\nu \cdot (p_a + q) = E'_\nu M_a \left[\left(1 + \frac{q_0}{M_a}\right) - \frac{|p'_\nu||q|}{M_a} \cos \theta \right] \approx E_\nu M_a, \quad (4.21)$$

$$p_\nu \cdot p'_a = p_\nu \cdot (p_a + q) = E_\nu M_a \left[\left(1 + \frac{q_0}{M_a}\right) - \frac{|p_\nu||q|}{M_a} \cos \theta \right] \approx E_\nu M_a. \quad (4.22)$$

Then the transition matrix element for neutrino coherent elastic scattering off a rest atom can be written as

$$|\mathcal{M}_{\text{atom}}|^2 = 8 G_F^2 M_a E_\nu^2 \left[C_{LR}^2 \left(1 + \frac{|p_\nu|^2}{E_\nu^2} \cos \theta\right) + 3C_{LR}'^2 \left(1 - \frac{|p_\nu|^2}{3E_\nu^2} \cos \theta\right) \right], \quad (4.23)$$

which is consistent with the results in papers [Weber (1988); Lewis (1980); Papavassiliou et al. (2006); Smith (1984)]. From the above formula we found that the scattering matrix neatly divides into two distinct components: a vector-like component (first term) and an axial-vector like component (second term). They have different angular dependencies: the vector part has a $(|p_\nu|^2/E_\nu^2 \cos \theta)$ dependence, while the axial part has a $(-|p_\nu|^2/3E_\nu^2 \cos \theta)$ behavior. However, in the case of the nonrelativistic neutrino, both angular dependencies can be neglected because of the limit $p_\nu \ll m_\nu$.

Next, we consider the nonrelativistic electron neutrino ν_e scattering off an general atom with Z protons, N neutrons and Z electrons. Then from Eq. (4.23), the matrix element can be written as

$$\begin{aligned} |\mathcal{M}_{\text{atom}}|^2 &= 8 G_F^2 M_a E_\nu^2 \left[(3Z - A)^2 \left(1 + \frac{|p_\nu|^2}{E_\nu^2} \cos \theta\right) + 3(3Z - A)^2 \left(1 - \frac{|p_\nu|^2}{3E_\nu^2} \cos \theta\right) \right] \\ &\approx 32 G_F^2 M_a E_\nu^2 (3Z - A)^2, \end{aligned} \quad (4.24)$$

where we neglect the angular dependence because of the nonrelativistic limit, and the coefficient $(3Z - A)^2$ for different target atoms are given in Table.(4.2). On the

other hand, for nonrelativistic $\nu_{\mu,\tau}$, the scattering matrix is given by

$$|\mathcal{M}_{\text{atom}}|^2 = 8 G_F^2 M_a E_\nu^2 \left[(A - Z)^2 \left(1 + \frac{|p_\nu|^2}{E_\nu^2} \cos \theta \right) + 3 (A - Z)^2 \left(1 - \frac{|p_\nu|^2}{3E_\nu^2} \cos \theta \right) \right] \\ \approx 32 G_F^2 M_a E_\nu^2 (Z - A)^2, \quad (4.25)$$

where the coefficient $(Z - A)^2$ different target atoms are given in Table.(4.2). The transition matrix for ν_e differs from that of $\nu_{\mu,\tau}$; this is due to the charged current reaction with the atomic electrons. Furthermore, the neutral current interaction for the electron and proton will cancel each other because of the opposite weak isospin I_3 and charge \mathcal{Q} . As a result, the coherent neutrino scattering from an atom is sensitive to the method of the neutrino-electron coupling.

Neutrino Flavor:	ν_e	$\nu_{\mu,\tau}$
Target Atom	$(3Z - A)^2$	$(Z - A)^2$
$H_2(A = 2, Z = 2)$	16	0
${}^3H_e(A = 3, Z = 2)$	9	1
$HD(A = 3, Z = 2)$	9	1
${}^4_2H_e(A = 4, Z = 2)$	4	4
$DD(A = 4, Z = 2)$	4	4
${}^{12}_6C(A = 12, Z = 6)$	36	36

Table 4.2: The coefficients for transition amplitude and scattering probability of ν_e and $\nu_{\mu,\tau}$ coherent elastic scattering off different target atoms. The definition of atomic mass is $A = Z + N$, where Z and N are the number of protons and neutron respectively.

Mean field potential for neutrino coherent scattering

When neutrinos are propagating in matter and interacting with the background particles, they can be described by the picture of free neutrinos traveling in an effective potential [Wolfenstein (1978)]. In the following we describe the effective potential between neutrinos and the target atom, and generalize the potential to the case of neutrino coherent scattering with a multi-atom system.

Let us consider a neutrino elastic scattering off an atom which is composed of Z protons, N neutrons and Z electrons. For the elastic neutrino atom scattering, the

low-energy neutrinos are scattering off both atomic electrons and the nucleus. Considering the effective low-energy CC and NC interactions, the effective Hamiltonian in current-current interaction form can be written as

$$\mathcal{H}_I^{\text{atom}} = \mathcal{H}_I^{\text{electron}} + \mathcal{H}_I^{\text{nucleon}} = \frac{G_F}{\sqrt{2}} (j_\mu \mathcal{J}_{\text{electron}}^\mu + j_\mu \mathcal{J}_{\text{nucleon}}^\mu), \quad (4.26)$$

where $\mathcal{J}_{\text{nucleon}}^\mu$ denote the hadronic current for nucleus, j^μ and $\mathcal{J}_{\text{electron}}^\mu$ are the lepton currents for neutrino and electron respectively. According to the weak interaction theory, the lepton current for neutrino and electron can be written as

$$j_\mu = \overline{\psi}_\nu \gamma_\mu (1 - \gamma_5) \psi_\nu, \quad (4.27)$$

$$\mathcal{J}_{\text{electron}}^\mu = \overline{\psi}_e \gamma_\mu (1 - \gamma_5) \psi_e \quad (\text{W}^\pm \text{ exchange}), \quad (4.28)$$

$$\mathcal{J}_{\text{electron}}^\mu = \overline{\psi}_e \gamma_\mu (c_V^e - c_A^e \gamma_5) \psi_e \quad (\text{Z}^0 \text{ exchange}), \quad (4.29)$$

where ψ_ν and ψ_e represent the spinor for the neutrino and electron, respectively. From Eq. (4.11) the coupling coefficient for electrons are $c_V^e = -1/2 + 2 \sin^2 \theta_w$ and $c_A^e = -1/2$. The hadronic current for is given by the expression [Giunti and Kim (2007)]

$$\mathcal{J}_{\text{nucleon}}^\mu \equiv \overline{\psi}_t \gamma^\mu (c_V^t - c_A^t \gamma_5) \psi_t, \quad (4.30)$$

where subscript t means the target constituents (protons and neutrons). From Eq. (4.11) the coupling constants for proton(uud) and neutron(udd) are given by

$$c_V^p = \frac{1}{2} - 2 \sin^2 \theta_w, \quad c_A^p = \frac{1}{2}, \quad \text{proton} \quad (4.31)$$

$$c_V^n = -\frac{1}{2}, \quad c_A^n = -\frac{1}{2}, \quad \text{neutron}. \quad (4.32)$$

To obtain the effective potential for atom, we need to average the effective Hamiltonian over the electron and nucleon background. For the neutrino-nucleon (proton,neutron) interaction, we only have the neutral current interaction via Z^0 boson. However, for the neutrino-electron interaction, we can have charged-current or neutral current interaction depending on the flavor or neutrino. In following, we consider interaction between ν_e and electrons first which includes both charged and neutral-currents interaction for general discussion.

Considering atomic electrons as a gas of unpolarized electrons with a statistical distribution function $f(E_e)$, the effective potential for neutrino-electron interaction can be obtained by averaging the effective Hamiltonian over the electron background [Giunti and Kim (2007)]

$$\begin{aligned} \langle \mathcal{H}_I^{\text{electron}} \rangle &= \frac{G_F}{\sqrt{2}} \int \frac{d^3 p_e}{(2\pi)^3 2E_e} f(E_e, T) [\overline{\psi}_\nu(x) \gamma_\mu (1 - \gamma_5) \psi_\nu(x)] \\ &\times \frac{1}{2} \sum_{h_e=\pm 1} \langle e^-(p_e, h_e) | \overline{\psi}_e \gamma^\mu ((1 + c_V^e) - (1 + c_A^e) \gamma_5) \psi_e | e^-(p_e, h_e) \rangle, \end{aligned} \quad (4.33)$$

where h_e denotes the helicity of the electron. The average over helicity of the electron matrix element can be calculated with Dirac spinor and gamma matrix traces [Giunti and Kim (2007)]. Then the average effective Lagrangian can be written as

$$\begin{aligned} \langle \mathcal{H}_I^{\text{electron}} \rangle &= \frac{G_F}{\sqrt{2}} (1 + c_V^e) \int \frac{d^3 p_e}{(2\pi)^3} f(E_e) \left[\overline{\psi}_\nu(x) \frac{\gamma^\mu p_{e\mu}}{E_e} (1 - \gamma_5) \psi_\nu(x) \right] \\ &= \frac{G_F}{\sqrt{2}} (1 + c_V^e) \left[\int \frac{d^3 p_e}{(2\pi)^3} f(E_e) \left(\gamma^0 - \frac{\vec{\gamma} \cdot \vec{p}_e}{E_e} \right) \right] \overline{\psi}_\nu(x) (1 - \gamma_5) \psi_\nu(x) \\ &= \left[\frac{G_F}{\sqrt{2}} (1 + c_V^e) n_e \right] \overline{\psi}_\nu(x) \gamma^0 (1 - \gamma_5) \psi_\nu(x), \end{aligned} \quad (4.34)$$

where n_e is the number density of the electron. In this case, the effective potential for neutrino-atomic electron interaction can be written as

$$V_I^{\text{electron}} = \frac{G_F}{\sqrt{2}} (1 + c_V^e) n_e = \frac{G_F}{\sqrt{2}} (4 \sin^2 \theta_w + 1) n_e. \quad (4.35)$$

The same method can be applied to the neutrino-nuclear interactions. Following the same approach and averaging the effective neutrino-nuclear Hamiltonian over the nuclear background, the effective potential experienced by a neutrino in a background of neutron/proton is given by [Giunti and Kim (2007)]

$$V_I^{\text{proton}} = \frac{G_F}{\sqrt{2}} (1 - 4 \sin^2 \theta_w) n_p, \quad V_I^{\text{neutron}} = -\frac{G_F}{\sqrt{2}} n_n, \quad (4.36)$$

where n_p and n_n represent the number density of proton and neutron. Combining the neutron and proton potential together, we define the effective nucleon potential

experienced by neutrino as

$$V_I^{\text{nucleon}} \equiv -\frac{G_F}{\sqrt{2}} \left[1 - (1 - 4 \sin^2 \theta_w) \xi \right] n_n, \quad \xi = n_p/n_n, \quad (4.37)$$

where ξ is the ratio between proton and neutron number density.

In our study, we generalize the effective potential to the case of neutrino coherent scattering with multi-atom system, we consider a neutrino coherent forward scatters from a spherical symmetric system which is composed by atoms. In this case, the neutrino scatters off every atom, and it is impossible to identify which scatterer the neutrino interacts with and thus it is necessary to sum over all possible contributions from each atom. In such circumstances, it is appropriate to assume that the number density of electrons and neutrons can be written as

$$n_e = Z_e \left(\frac{N_{\text{atom}}}{V} \right), \quad \text{and} \quad n_n = N \left(\frac{N_{\text{atom}}}{V} \right), \quad (4.38)$$

where N_{atom} is the number of atoms inside the system, V is the volume of system, Z is the number of electrons, and N is the number of neutrons. Then the effective potential is given by

$$\begin{aligned} V_I &= V_I^{\text{electron}} + V_I^{\text{nucleon}} \\ &= \frac{G_F}{\sqrt{2}} \left(\frac{N_{\text{atom}}}{V} \right) \left\{ (4 \sin^2 \theta_w \pm 1) Z_e - \left[1 - (1 - 4 \sin^2 \theta_w) \xi \right] N \right\}, \end{aligned} \quad (4.39)$$

where the + sign is for electron neutrinos ν_e and the - sign is for muon(tau) neutrinos $\nu_{\mu,\tau}$, separately. From Eq. (4.39), it shows that the effective potential depends on the number density of electrons and nucleons contained within the wavelength. Thus by increasing the atoms contained in the wavelength or selecting different atoms as targets, we can enhance the effective potential and may be able to provide a sensitive way to detect the cosmic neutrino background. Beside the detection of cosmic neutrino background, the effective potential for multi-atom can also provide new approaches for studying other aspects of neutrino physics in the future.

4.1.2 Matrix elements of incoherent neutrino scattering

To determine the freeze-out temperature (chemical/kinetic freeze-out) for a given flavor of neutrinos, we need to know all the elastic and inelastic interaction pro-

cesses in the early Universe and compare their interaction rate with Hubble expansion rate. In this section we summarize the matrix elements for the neutrino annihilation/production processes and elastic scattering processes which are relevant for investigating neutrino freezeout. These matrix elements serve as one of the fundamental ingredients for solving the Boltzmann equation [Birrell et al. (2014b)].

Considering the Universe with temperature $T \approx \mathcal{O}(\text{MeV})$, the particle species in comisc plasma are given by:

$$\text{Particle species in plasma : } \{ \gamma, l^-, l^+, \nu_e, \nu_\mu, \nu_\tau, \bar{\nu}_e, \bar{\nu}_\mu, \bar{\nu}_\tau \}, \quad (4.40)$$

where l^\pm represents the charged leptons. In this case, neutrinos can interact with all these particles via weak interactions and remain in equilibrium. In Table. 4.3 and Table. 4.4 we present the matrix elements $|M|^2$ for different weak interaction processes in the early Universe.

In the calculation of transition amplitude, we use the low energy approximation for W^\pm and Z^0 massive propagators, i.e.

$$Z^0 \text{ boson : } \frac{-i \left[g_{\mu\nu} - \frac{q_\mu q_\nu}{M_z^2} \right]}{q^2 - M_z^2} \approx \frac{i g_{\mu\nu}}{M_z^2}, \quad W^\pm \text{ boson : } \frac{-i \left[g_{\mu\nu} - \frac{q_\mu q_\nu}{M_w^2} \right]}{q^2 - M_w^2} \approx \frac{i g_{\mu\nu}}{M_w^2}, \quad (4.41)$$

and consider the tree-level Feynman diagram contributions only. Then, following the Feynman rules of weak interaction [Griffiths (2008)], we obtain the matrix elements $|M|^2$ for different interaction processes.

Annihilation/Production	
Scattering Process	Transition Amplitude $ M ^2$
$l^- + l^+ \longrightarrow \nu_l + \bar{\nu}_l$	$32G_F^2 \left[(1 + 2 \sin^2 \theta_w)^2 (p_1 \cdot p_4) (p_2 \cdot p_3) \right. \\ + (2 \sin^2 \theta_w)^2 (p_1 \cdot p_3) (p_2 \cdot p_4) \\ \left. + 2 \sin^2 \theta_w (1 + 2 \sin^2 \theta_w) m_l^2 (p_3 \cdot p_4) \right]$
$l'^- + l'^+ \longrightarrow \nu_l + \bar{\nu}_l$	$32G_F^2 \left[(1 - 2 \sin^2 \theta_w)^2 (p_1 \cdot p_4) (p_2 \cdot p_3) \right. \\ + (2 \sin^2 \theta_w)^2 (p_1 \cdot p_3) (p_2 \cdot p_4) \\ \left. - 2 \sin^2 \theta_w (1 - 2 \sin^2 \theta_w) m_{l'}^2 (p_3 \cdot p_4) \right]$
$\nu_l + \bar{\nu}_l \longrightarrow \nu_l + \bar{\nu}_l$	$32G_F^2 (p_1 \cdot p_4) (p_2 \cdot p_3)$
$\nu_{l'} + \bar{\nu}_{l'} \longrightarrow \nu_l + \bar{\nu}_l$	$32G_F^2 (p_1 \cdot p_4) (p_2 \cdot p_3)$

Table 4.3: The transition amplitude for different annihilation and production processes. The definition of particle number is given by $1 + 2 \leftrightarrow 3 + 4$, where $l, l' = e, \mu, \tau$ ($l \neq l'$).

Elastic Scattering Process (ν_e)	
Scattering Process	Transition Amplitude $ M ^2$
$\nu_l + l^- \longrightarrow \nu_l + l^-$	$32G_F^2 \left[(1 + 2 \sin^2 \theta_w)^2 (p_1 \cdot p_2) (p_3 \cdot p_4) \right. \\ \left. + (2 \sin^2 \theta_w)^2 (p_1 \cdot p_4) (p_2 \cdot p_3) \right. \\ \left. - 2 \sin^2 \theta_w (1 + 2 \sin^2 \theta_w) m_l^2 (p_1 \cdot p_3) \right]$
$\nu_l + l^+ \longrightarrow \nu_l + l^+$	$32G_F^2 \left[(1 + 2 \sin^2 \theta_w)^2 (p_1 \cdot p_4) (p_2 \cdot p_3) \right. \\ \left. + (2 \sin^2 \theta_w)^2 (p_1 \cdot p_2) (p_3 \cdot p_4) \right. \\ \left. - 2 \sin^2 \theta_w (1 + 2 \sin^2 \theta_w) m_l^2 (p_1 \cdot p_3) \right]$
$\nu_l + l'^- \longrightarrow \nu_l + l'^-$	$32G_F^2 \left[(1 - 2 \sin^2 \theta_w)^2 (p_1 \cdot p_2) (p_3 \cdot p_4) \right. \\ \left. + (2 \sin^2 \theta_w)^2 (p_1 \cdot p_4) (p_2 \cdot p_3) \right. \\ \left. + 2 \sin^2 \theta_w (1 - 2 \sin^2 \theta_w) m_{l'}^2 (p_1 \cdot p_3) \right]$
$\nu_l + l'^+ \longrightarrow \nu_l + l'^+$	$32G_F^2 \left[(1 - 2 \sin^2 \theta_w)^2 (p_1 \cdot p_4) (p_2 \cdot p_3) \right. \\ \left. + (2 \sin^2 \theta_w)^2 (p_1 \cdot p_2) (p_3 \cdot p_4) \right. \\ \left. + 2 \sin^2 \theta_w (1 - 2 \sin^2 \theta_w) m_{l'}^2 (p_1 \cdot p_3) \right]$
$\nu_l + \nu_l \longrightarrow \nu_l + \nu_l$	$\frac{1}{2!} \frac{1}{2!} \times 32G_F^2 \left[4 (p_1 \cdot p_2) (p_3 \cdot p_4) \right]$
$\nu_l + \bar{\nu}_l \longrightarrow \nu_l + \bar{\nu}_l$	$32G_F^2 \left[4 (p_1 \cdot p_4) (p_2 \cdot p_3) \right]$
$\nu_l + \nu_{l'} \longrightarrow \nu_l + \nu_{l'}$	$32G_F^2 \left[(p_1 \cdot p_2) (p_3 \cdot p_4) \right]$
$\nu_l + \bar{\nu}_{l'} \longrightarrow \nu_l + \bar{\nu}_{l'}$	$32G_F^2 \left[(p_1 \cdot p_4) (p_2 \cdot p_3) \right]$

Table 4.4: The transition amplitude for different elastic scattering processes. The definition of particle number is given by $1 + 2 \leftrightarrow 3 + 4$, where $l, l' = e, \mu, \tau$ ($l \neq l'$).

4.2 Neutrinos in the early Universe

In the early Universe the neutrinos are kept in equilibrium with cosmic plasma via the weak interaction processes. However, as the Universe expanded, these weak interactions gradually became too slow to maintain equilibrium, then the neutrinos ceased interacting and decoupled from the cosmic background. This relic neutrino background carries great information about our early Universe which can provide the information when our Universe is about 1 sec old.

Today the Universe is believed to be filled with relic cosmic neutrinos. Although the cosmic neutrino background is hard to detect, we can use entropy conservation to infer their temperature and find that they should have the temperature $T_\nu^0 = 1.9$ K in the present epoch for massless neutrinos. However, from the neutrino oscillation experiment, we know that the neutrinos are not massless particles.

The square mass difference Δm_{ij}^2 has been experimentally measured, from the neutrino oscillation experiment [Workman et al. (2022)]:

$$\Delta m_{21}^2 = 7.39_{-0.20}^{+0.21} \times 10^{-5} \text{ eV}^2, \quad (4.42)$$

$$\Delta m_{32}^2 = 2.45_{-0.03}^{+0.03} \times 10^{-3} \text{ eV}^2. \quad (4.43)$$

and neutrino mass eigenvalue can be ordered in the normal mass hierarchy ($m_1 \ll m_2 < m_3$) or inverted mass hierarchy ($m_3 \ll m_1 < m_2$). All three mass states remained relativistic until the temperature dropped below their rest mass. These results allow for the possibility that one mass eigenstate or two mass eigenstates of neutrinos may become non-relativistic today.

4.2.1 Overview of neutrino freeze-out in the early Universe

The properties of the neutrino background are influenced by the details of the freeze-out or decoupling process at a temperature $T = \mathcal{O}(2\text{MeV})$. In the literature one finds estimates of freeze-out temperatures based on a comparison of Hubble expansion with neutrino scattering length and considering only number changing (i.e. chemical) processes. In the paper [Birrell et al. (2014b)], we employ a similar defini-

tion of freeze-out temperature in the context of the Boltzmann equation and refine the results by noting that there are three different freeze-out processes for neutrinos:

1. Neutrino chemical freeze-out: the temperature at which neutrino number changing processes such as $e^-e^+ \rightarrow \nu\bar{\nu}$ effectively cease. After chemical freeze-out, there are no reactions that, in a noteworthy fashion, can change the neutrino abundance and so particle number is conserved.

2. Neutrino kinetic freeze-out: the temperature at which the neutrino momentum exchanging interactions such as $e^\pm\nu \rightarrow e^\pm\nu$ are no longer occurring rapidly enough to maintain an equilibrium momentum distribution.

3. Collisions between neutrinos: Those collisions $\nu\nu \rightarrow \nu\nu$ are capable of reequilibrating energy within and between neutrino flavor families. These processes end at a yet lower temperature and the neutrinos will be truly free-streaming from that point on.

To estimate the freeze-out temperature, we need to solve the Boltzmann equation with different types of collision terms with the transition matrices from Table. 4.3 and Table. 4.4. The paper [Birrell et al. (2014b)] developed a new method for analytically simplifying the collision integrals and showing that the neutrino freeze-out temperature is controlled by standard model (SM) parameters. The freeze-out temperature depends only on the magnitude of the Weinberg angle in the form $\sin^2\theta_W$, and a dimensionless relative interaction strength parameter η ,

$$\eta \equiv M_p m_e^3 G_F^2, \quad M_p^2 \equiv \frac{1}{8\pi G_N}, \quad (4.44)$$

a combination of the electron mass m_e , Newton constant G_N (expressed above in terms of Planck mass M_p), and the Fermi constant G_F . The dimensionless interaction strength parameter η in the present-day vacuum has the value

$$\eta_0 \equiv M_p m_e^3 G_F^2|_0 = 0.04421. \quad (4.45)$$

The magnitude of $\sin^2\theta_W$ is not fixed within the SM and could be subject to variation as a function of time or temperature. In Fig. 4.1 we show the dependence of neutrino freeze-out temperatures for ν_e and $\nu_{\mu,\tau}$ on SM model parameters $\sin^2\theta_W$

and η in detail. The impact of SM parameter values on neutrino freeze-out and the discussion of the implications and connections of this work to other areas of physics, namely Big Bang Nucleosynthesis and dark radiation can be found in detail in [Dreiner et al. (2012); Boehm et al. (2012); Blennow et al. (2012); Birrell et al. (2014b)]. A comprehensive investigation of neutrino freezeout, and a novel approach to analytically simplify the collision integrals for the Boltzmann equation can be found in Dr. Jeremiah Birrell's PhD thesis [Birrell (2014)].

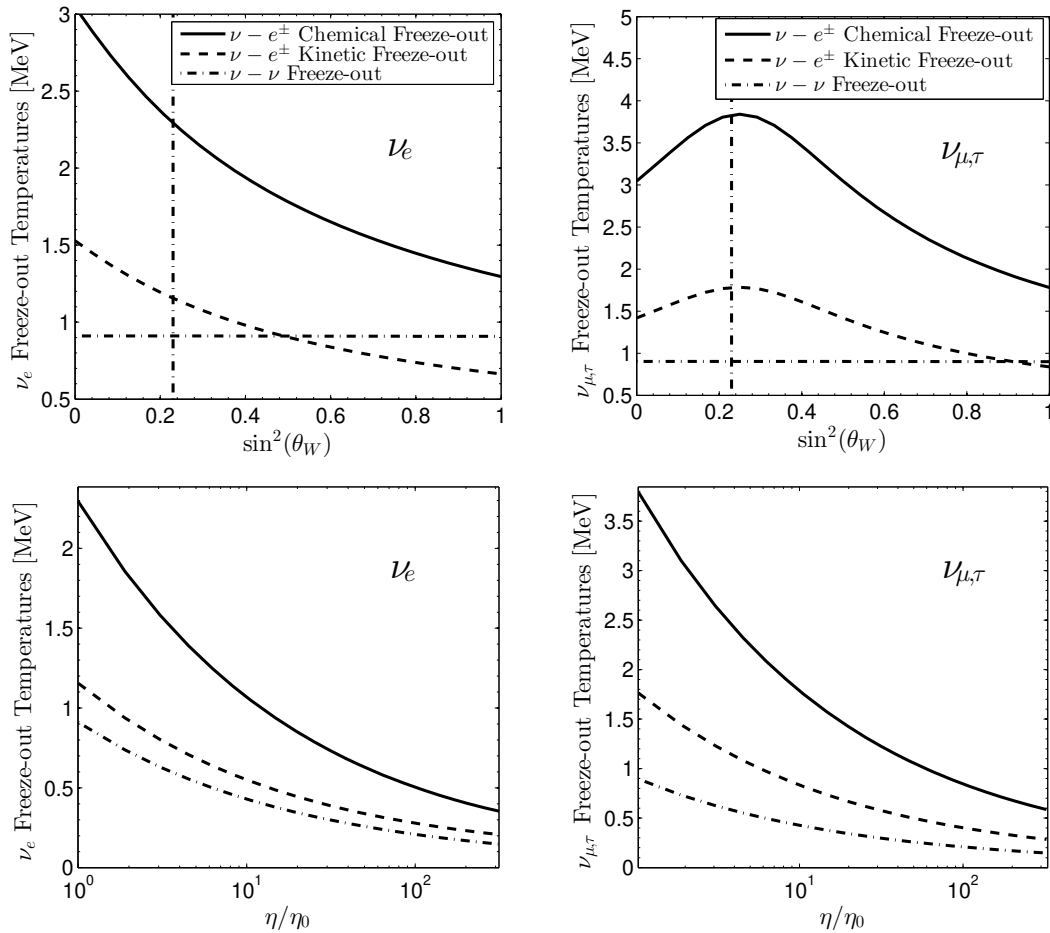


Figure 4.1: Freeze-out temperatures for electron neutrinos (left) and μ, τ neutrinos (right) for the three types of freeze-out processes adapted from paper [Birrell et al. (2014b)]. Top panels print temperature curves as a function of $\sin^2 \theta_W$ for $\eta = \eta_0$, the vertical dashed line is $\sin^2 \theta_W = 0.23$; bottom panels are printed as a function of relative change in interaction strength η/η_0 obtained for $\sin^2 \theta_W = 0.23$.

4.2.2 Lepton number and effective number of neutrinos

Neutrinos decoupled from the cosmic plasma in the early Universe at a temperature of $T = \mathcal{O}(2\text{MeV})$ and became free-streaming. However, after freezeout neutrinos still continue to play a significant role in the evolution of the Universe and have a huge impact on cosmological observations such as Big Bang Nucleosynthesis (BBN), the Cosmic Microwave Background (CMB), and the matter spectrum for large scale structure. This is due to the sensitivity of the Hubble parameter to the total energy density in the Universe. Besides photons, neutrinos are the most abundant species and contribute significantly to the relativistic energy density throughout the early Universe, affecting the Hubble expansion rate significantly.

The contribution of energy density from the neutrino sector can be described by the effective number of neutrinos N_ν^{eff} , which captures the number of relativistic degrees of freedom for neutrinos as well as any reheating that occurred in the sector after freeze-out. The effective number of neutrino is defined as

$$N_\nu^{\text{eff}} \equiv \frac{\rho_\nu^{\text{tot}}}{\frac{7\pi^2}{120} \left(\frac{4}{11}\right)^{4/3} T_\gamma^4}, \quad (4.46)$$

where ρ_ν^{tot} is the total energy density in neutrinos and T_γ is the photon temperature. N_ν^{eff} is defined such that three neutrino flavors with zero participation of neutrinos in reheating during e^\pm annihilation results in $N_\nu^{\text{eff}} = 3$. The factor of $(4/11)^{1/3}$ relates the photon temperature to the free-streaming neutrinos temperature, under the assumption of zero neutrino reheating after e^\pm annihilation. The currently accepted theoretical value is $N_\nu^{\text{eff}} = 3.046$, after including the slight effect of neutrino reheating [Mangano et al. (2005); Birrell et al. (2014b)]. The favored value of N_ν^{eff} can be found by fitting to CMB data. In 2013 the Planck collaboration found $N_\nu^{\text{eff}} = 3.36 \pm 0.34$ (CMB only) and $N_\nu^{\text{eff}} = 3.62 \pm 0.25$ (CMB and H_0) [Ade et al. (2014)].

To explain the experimental value of N_ν^{eff} , many studies aim to improve the calculation of neutrino decoupling in the early Universe, including exploring the dependence of freeze-out on natural constants [Birrell et al. (2014b)], the entropy transfer from e^\pm annihilation and finite temperature correction [Dicus et al. (1982);

Heckler (1994); Fornengo et al. (1997)], neutrino decoupling with flavor oscillations [Mangano et al. (2002, 2005)], and investigating nonstandard neutrino interactions [Morgan (1981); Fukugita and Yazaki (1987); Elmfors et al. (1997); Vogel and Engel (1989); Mangano et al. (2006); Giunti and Studenikin (2009); Mangano et al. (2006)].

The standard cosmological model assumes that the lepton asymmetry $L \equiv [N_L - N_{\bar{L}}]/N_\gamma$ (normalized with the photon number) between leptons and anti-leptons is small, similar to the baryon asymmetry $B = [N_B - N_{\bar{B}}]/N_\gamma$; most often it is assumed $L = B$. Barenboim, Kinney, and Park [Barenboim et al. (2017); Barenboim and Park (2017)] noted that the lepton asymmetry of the Universe is one of the most weakly constrained parameters in cosmology and they propose that models with leptogenesis are able to accommodate a large lepton number asymmetry surviving up to today. Moreover, the discrepancy between H_{CMB} and H_0 has increased [Riess et al. (2018a,b); Aghanim et al. (2020a)]. The Hubble tension and the possibility that leptogenesis in the early Universe resulted in neutrino asymmetry motivate our study of the dependence of N_ν^{eff} on lepton asymmetry, L . In our work [Yang et al. (2018a)] we consider $L \simeq 1$ and explore how this large cosmological lepton yield relates to the effective number of (Dirac) neutrinos N_ν^{eff} .

Relation between N_ν^{eff} and neutrino chemical potential

We consider now neutrinos decouple [Birrell et al. (2015)] at a temperature of $T_f \simeq 2 \text{ MeV}$ and are subsequently free-streaming. Assuming exact thermal equilibrium at the time of decoupling, the neutrino distribution can be subsequently written as (see [Birrell et al. (2014a)] and references therein)

$$f_\nu = \frac{1}{\exp\left(\sqrt{\frac{E^2 - m_\nu^2}{T_\nu^2} + \frac{m_\nu^2}{T_f^2}} - \sigma \frac{\mu_\nu}{T_f}\right) + 1}, \quad T_\nu \equiv \frac{a(t_f)}{a(t)} T_f, \quad (4.47)$$

where $\sigma = +1(-1)$ denotes particles (antiparticles) and we define the effective neutrino temperature T_ν by the red-shifting of momentum in the comoving volume element of the Universe.

Since the freeze-out temperature $T_f \gg m_\nu$ and also neutrino temperature $T_\nu \gg m_\nu$ in the domain of our analysis, we consider the massless limit in Eq. (4.47). Under this approximation, the total neutrino energy density can be written as

$$\rho_\nu^{\text{tot}} = \frac{g_\nu T_\nu^4}{2\pi^2} \left[\frac{7\pi^4}{60} + \frac{\pi^2}{2} \left(\frac{\mu_\nu}{T_f} \right)^2 + \frac{1}{4} \left(\frac{\mu_\nu}{T_f} \right)^4 \right]. \quad (4.48)$$

Substituting Eq. (4.48) into the definition of the effective number of neutrinos Eq. (4.46), we obtain

$$N_\nu^{\text{eff}} = 3 \left(\frac{11}{4} \right)^{\frac{4}{3}} \left(\frac{T_\nu}{T_\gamma} \right)^4 \left[1 + \frac{30}{7\pi^2} \left(\frac{\mu_\nu}{T_f} \right)^2 + \frac{15}{7\pi^4} \left(\frac{\mu_\nu}{T_f} \right)^4 \right]. \quad (4.49)$$

From Eq. (4.49) we have for the standard photon reheating ratio $T_\nu/T_\gamma = (4/11)^{1/3}$ [Kolb and Turner (1990b)] and degeneracy $g_\nu = 3$ (flavor), the relation between the effective number of neutrinos and the chemical potential at freezeout

$$N_\nu^{\text{eff}} = 3 \left[1 + \frac{30}{7\pi^2} \left(\frac{\mu_\nu}{T_f} \right)^2 + \frac{15}{7\pi^4} \left(\frac{\mu_\nu}{T_f} \right)^4 \right]. \quad (4.50)$$

To solve the neutrino chemical potential μ_ν/T_f as a function of the effective number of neutrinos, we can neglect the $(\mu_\nu/T_f)^4$ term in Eq. (4.50) because $m_\nu \ll T_f$ and obtain

$$\frac{\mu_\nu}{T_f} = \pm \sqrt{\frac{7\pi^2}{30} \left(\frac{N_\nu^{\text{eff}}}{3} - 1 \right)}. \quad (4.51)$$

In Fig. 4.2 we plot the free-streaming neutrino chemical potential $|\mu_\nu|/T_f$ as a function of the effective number of neutrinos N_ν^{eff} . For comparison, the solid (blue) line is the exact solution of $|\mu_\nu|/T_f$ by solving Eq. (4.50) numerically, and the (red) dashed line is the approximate solution Eq. (4.51) by neglecting the $(\mu_\nu/T_f)^4$ in calculation. In the parameter range of interest, we show that the term $(\mu_\nu/T_f)^4$ only contributes $\approx 2\%$ to the calculation and henceforth we neglect it, and use the approximation Eq. (4.51).

The SM value of the effective number of neutrinos, $N_\nu^{\text{eff}} = 3$, is obtained under the assumption that the neutrino chemical potentials are not essential, *i.e.*, $\mu_\nu \ll T_f$.

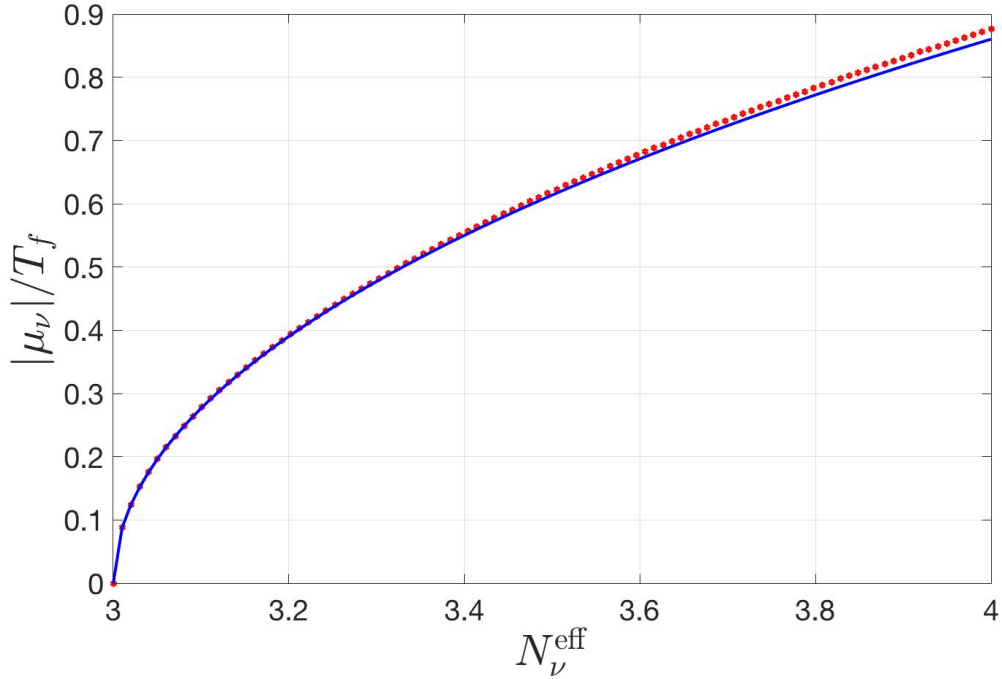


Figure 4.2: The free-streaming neutrino chemical potential $|\mu_\nu|/T_f$ as a function of the effective number of neutrinos N_ν^{eff} . The solid (blue) line is the exact solution and the (red) dashed line is the approximate solution neglecting the $(\mu_\nu/T_f)^4$ term; the maximum difference in the domain shown is about 2%.

From Fig. 4.2, to interpret the literature values $N_\nu^{\text{eff}} = 3.36 \pm 0.34$ (CMB only) and $N_\nu^{\text{eff}} = 3.62 \pm 0.25$ (CMB and H_0), we require $0.52 \leq \mu_\nu/T_f \leq 0.69$. These values suggest a possible neutrino-antineutrino asymmetry at freezeout, *i.e.* a difference between the number densities of neutrinos and antineutrinos.

Dependence of N_ν^{eff} on lepton asymmetry

We now obtain the relation between neutrino chemical potential and the baryon to lepton ratio. Let us consider the neutrino freezeout temperature $T_f \simeq 2.0$ MeV; here we treat neutrino freezeout as occurring instantaneously and prior to e^\pm annihilation (implying zero neutrino reheating). Comoving lepton (and baryon) number is conserved after the epoch of leptogenesis (baryogenesis, respectively) which precedes

the epoch under consideration in this work ($T \lesssim 2$ MeV).

The lepton-density asymmetry ℓ at neutrino freeze-out can be written as

$$\ell_f \equiv (n_e - n_{\bar{e}})_f + \sum_{i=e,\mu,\tau} (n_{\nu_i} - n_{\bar{\nu}_i})_f, \quad (4.52)$$

where we use the subscript f to indicate that the quantities should be evaluated at the neutrino freeze-out temperature. As a first approximation, here we assume that all neutrinos freeze-out at the same temperature and their chemical potentials are the same; *i.e.*,

$$\mu_\nu = \mu_{\nu_e} = \mu_{\nu_\mu} = \mu_{\nu_\tau}. \quad (4.53)$$

Furthermore, neutrino oscillation implies that neutrino number is freely exchanged between flavors; *i.e.*, $\nu_e \rightleftharpoons \nu_\mu \rightleftharpoons \nu_\tau$, and we can assume that all neutrino flavors share the same population. Under these assumptions, the lepton-density asymmetry can be written as

$$\ell_f = (n_e - n_{\bar{e}})_f + (n_\nu - n_{\bar{\nu}})_f, \quad (4.54)$$

where the three flavors are accounted for by taking the degeneracy $g_\nu = 3$ in the last term. The difference in yield of neutrinos and antineutrinos can be written as

$$(n_\nu - n_{\bar{\nu}})_f = \frac{g_\nu}{6\pi^2} T_f^3 \left[\pi^2 \left(\frac{\mu_\nu}{T_f} \right) + \left(\frac{\mu_\nu}{T_f} \right)^3 \right]. \quad (4.55)$$

On the other hand, the baryon-density asymmetry b at neutrino freezeout is given by

$$b_f \equiv (n_p - n_{\bar{p}})_f + (n_n - n_{\bar{n}})_f \approx (n_p + n_n)_f, \quad (4.56)$$

where $n_{\bar{n}}$ and $n_{\bar{p}}$ are negligible in the temperature range we consider here. Taking the ratio ℓ_f/b_f , using charge neutrality, and introducing the entropy density we obtain

$$\left(\frac{\ell_f}{b_f} \right) \approx \left(\frac{n_p}{n_B} \right)_f + (n_\nu - n_{\bar{\nu}})_f \left(\frac{s}{n_B} \right)_f \frac{1}{s_f}, \quad n_B = (n_p + n_n), \quad (4.57)$$

where we introduce the notation n_B for the baryon number density. The proton concentration at neutrino freeze-out is given by

$$\left(\frac{n_p}{n_B}\right)_f = \frac{1}{1 + (n_n/n_p)_f} = \frac{1}{1 + \exp[-(Q + \mu_\nu)/T_f]}, \quad (4.58)$$

with $Q = m_n - m_p = 1.293 \text{ MeV}$. We neglect the electron chemical potential in the last step because the e^\pm asymmetry is determined by the proton density, and at energies of order a few MeV, the proton density is small, *i.e.*, $\mu_e \ll T_f$.

However, as we will see, for our study of N_ν^{eff} we will be interested in the case of a large lepton-to-baryon ratio. From Eq. (4.58) it is apparent that this can only be achieved through the second term in Eq. (4.57), with the first term then being negligible, as it is smaller than 1. So we further approximate

$$\left(\frac{\ell_f}{b_f}\right) \approx (n_\nu - n_{\bar{\nu}})_f \left(\frac{s}{n_B}\right)_f \frac{1}{s_f}. \quad (4.59)$$

We retained the full expression Eq. (4.58) in our above discussion to show that the presence of a chemical potential $\mu_\nu \simeq 0.2Q$ could lead to small, perhaps noticeable, effects on pre-BBN proton and neutron abundance. We defer this unrelated discussion to a separate future work. Note that for large $|\mu_\nu|$, Eq. (4.59) implies that the signs of μ_ν and ℓ_f are the same. However, for very small μ_ν the sign of ℓ_f is determined by the interplay between (anti)electrons and (anti)neutrinos; *i.e.*, there is competition between the two terms in Eq. (4.54).

In general, the total entropy density at freeze-out can be written

$$s_f = \frac{2\pi^2}{45} g_*^s(T_f) T_f^3, \quad (4.60)$$

where the g_*^s counts the degree of freedom for relativistic particles [Kolb and Turner (1990b)]. At $T_f \simeq 2 \text{ MeV}$, the relativistic species in the early Universe are photons, electron/positrons, and 3 neutrino species. We have

$$g_*^s = g_\gamma + \frac{7}{8} g_{e^\pm} + \frac{7}{8} g_{\nu\bar{\nu}} \left(\frac{T_\nu}{T_\gamma}\right)^3 \left[1 + \frac{15}{7\pi^2} \left(\frac{\mu_\nu}{T_f}\right)^2\right] = 10.75 + \frac{45}{4\pi^2} \left(\frac{\mu_\nu}{T_f}\right)^2, \quad (4.61)$$

where the degrees of freedom are given by $g_\gamma = 2$, $g_{e^\pm} = 4$, and $g_{\nu\bar{\nu}} = 6$, and we have $T_\nu = T_\gamma = T_f$ at neutrino freeze-out.

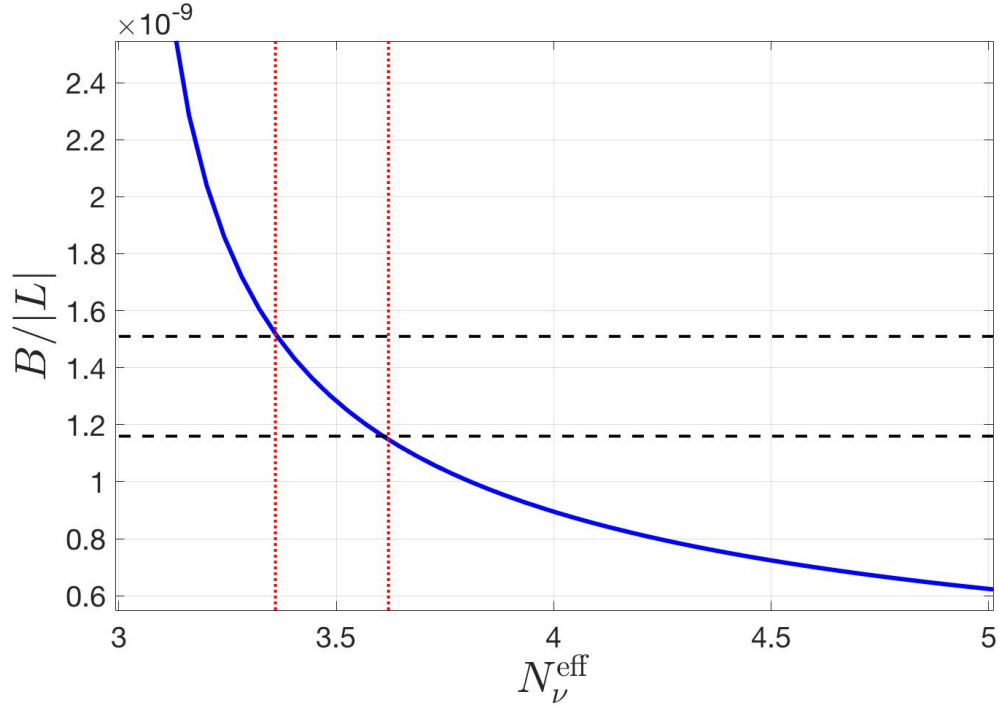


Figure 4.3: The ratio $B/|L|$ between the net baryon number and the net lepton number as a function of N_ν^{eff} : The solid blue line shows $B/|L|$. The vertical (red) dotted lines represent the values $3.36 \leq N_\nu^{\text{eff}} \leq 3.62$, which correspond to $1.16 \times 10^{-9} \leq B/|L| \leq 1.51 \times 10^{-9}$ (horizontal dashed lines).

Finally, since the entropy-per-baryon from neutrino freeze-out up to the present epoch is constant, we can obtain this value by considering the Universe's entropy content today [Fromerth et al. (2012)]. For $T \ll 1$ MeV, the entropy content today is carried by photons and neutrinos, yielding

$$\left(\frac{s}{n_B}\right)_{t_0} = \frac{\sum_i s_i}{n_B} = \frac{n_\gamma}{n_B} \left(\frac{s_\gamma}{n_\gamma} + \frac{s_\nu}{n_\gamma} + \frac{s_{\bar{\nu}}}{n_\gamma} \right) \quad (4.62)$$

$$= \left(\frac{1}{B}\right)_{t_0} \left[\frac{s_\gamma}{n_\gamma} + \frac{4}{3T_\nu} \frac{\rho_\nu^{\text{tot}}}{n_\gamma} - \frac{\mu_\nu}{T_f} \left(\frac{n_\nu - n_{\bar{\nu}}}{n_\gamma} \right) \right]_{t_0}, \quad (4.63)$$

where t_0 denotes the present day values, we have $B = n_B/n_\gamma = 0.605 \times 10^{-9}$ (CMB) [Patrignani et al. (2016)] from today's observation. The entropy per particle for a massless boson at zero chemical potential is $(s/n)_{\text{boson}} \approx 3.602$.

Substituting Eq. (4.55) and Eq. (4.60) into Eq. (4.59) yields the lepton-to-baryon

ratio

$$\frac{L}{B} = \frac{45}{4\pi^4} \frac{\pi^2(\mu_\nu/T_f) + (\mu_\nu/T_f)^3}{10.75 + 45(\mu_\nu/T_f)^2/4\pi^2} \left(\frac{s}{n_B} \right)_{t_0}, \quad (4.64)$$

in terms of μ_ν/T_f which is given by Eq.(4.51) and the present day entropy-per-baryon ratio. In Fig. 4.3 we show the ratio between the net baryon number and the net lepton number as a function of the effective number of neutrino species N_ν^{eff} with the parameter $B|_{t_0} = 0.605 \times 10^{-9}$ (CMB). We find that the values $N_\nu^{\text{eff}} = 3.36 \pm 0.34$ and $N_\nu^{\text{eff}} = 3.62 \pm 0.25$ require the ratio between baryon number and lepton number to be $1.16 \times 10^{-9} \leq B/|L| \leq 1.51 \times 10^{-9}$. These values are close to the baryon-to-photon ratio $0.57 \times 10^{-9} \leq B \leq 0.67 \times 10^{-9}$.

In summary, motivated by the necessity to explain a slightly faster Universe expansion, we believe that there is need for additional unobserved particles, leading to an increase in the Universe expansion rate. Considerable effort has been made in this direction, e.g., by introducing exotic and new ‘dark’ particles, see [Birrell and Rafelski (2015)] and references therein. In this work a similar effect is achieved by introducing lepton asymmetry in the Universe. We connected the lepton asymmetry in the Universe with the chemical neutrino potential μ_ν , and further evaluated the consequences for the Universe expansion. We have explored the other natural scenario regarding the baryon number-to-lepton number ratio. Instead of $B \simeq |L|$, we found that $0.4 \leq |L| \leq 0.52$ and $B \simeq 1.33 \times 10^{-9}|L|$ reconciles the CMB and current epoch results for the Hubble expansion parameter.

The large lepton asymmetry from cosmic neutrino can also affect the neutron lifespan in cosmic plasma which is one of the important parameter controlling BBN element abundances. In general the neutron lifespan dependence on temperature of the cosmic medium. When temperature $T = \mathcal{O}(\text{MeV})$, neutron decay occurs in the plasma of electron/positron and neutrino/antineutrino. Electrons and neutrinos in the background plasma can reduce the neutron decay rate by Fermi suppression to the neutron decay rate. Furthermore, the neutrino background can still provide the suppression after electron/positron pair annihilation becomes nearly complete. In this case, the large neutrino chemical potential from lepton asymmetry would play an

important role and needs to be accounted for in the precision study of the neutron lifespan in the cosmic plasma.

CHAPTER 5

Charged leptons in cosmic plasma

Charged leptons played significant roles in the dynamics and evolution of the early Universe. They were kept in equilibrium via electromagnetic and weak interactions. In this chapter, I examine a dynamical model of the abundance of charged leptons μ^\pm and e^\pm in the early Universe obtaining their disappearance temperature, the condition when they disappear from the particle inventory. Of particular interest is the dense electron-positron plasma present during the early Universe evolution. I study the damping rate and the magnetization process in this dense e^\pm plasma in the early Universe.

5.1 Overview of charge leptons in early Universe

The τ^\pm leptons can undergo various decay processes via the weak interaction in the early Universe, and is the only charged lepton that can decay into hadrons because of its heavy mass ($m_\tau = 1776.86$ MeV). The principle decay channels of τ^\pm are given by

$$\tau^- \rightarrow \nu_\tau + e^- + \bar{\nu}_e, \quad \tau^- \rightarrow \nu_\tau + \mu^- + \bar{\nu}_\mu, \quad (5.1)$$

$$\tau^- \rightarrow \nu_\tau + \pi^-, \quad \tau^+ \rightarrow \bar{\nu}_\tau + \pi^+, \quad (5.2)$$

where the vacuum lifespan for τ^\pm is given by [Workman et al. (2022)]

$$\tau_\tau = (290.3 \pm 0.5) \times 10^{-15} \text{ sec.} \quad (5.3)$$

Moreover, following the decay of τ^\pm into pions, these pions subsequently decay into a muon and a neutrino through the reaction

$$\pi^- \rightarrow \nu_\mu + \mu^-, \quad \pi^+ \rightarrow \bar{\nu}_\mu + \mu^+, \quad (5.4)$$

with pion vacuum lifespan $\tau_\pi = 2.6033 \times 10^{-8}$ sec [Workman et al. (2022)]. In this scenario, τ^\pm disappears from the Universe via multiparticle decay processes. These decay processes can contribute as one of the sources for the production of neutrinos and muons in the early Universe.

The μ^\pm lepton abundance is an important quantity required for the understanding of several fundamental questions regarding properties of the primordial Universe, particularly in relation to the freeze-out of strangeness flavor in the early Universe. We recall that the strangeness decay often proceeds into muons, energy thresholds permitting, as the charged kaons K^\pm have a 63% branching into $\mu + \bar{\nu}_\mu$. Should muons fall out of thermal abundance equilibrium this would directly impact the detailed balance back-reaction processes. Another, indirect influence on strangeness in early Universe arises through the nearly exclusive decay of charged pions into $\mu + \bar{\nu}_\mu$. Without chemical abundance equilibrium this back reaction stops too impacting pions and thus all other hadronic particles in the Universe.

On the other hand, we will show that the lightest charged leptons e^\pm can persist via the reaction $\gamma\gamma \rightarrow e^-e^+$ until the temperature $T = 20$ keV in the early Universe. After $T = 20$ keV, the positron rapidly disappears through annihilation, leaving only residual electrons to maintain the Universe's charge neutrality. The existence of an electron-positron plasma plays a pivotal role in several aspects of the early Universe as follows:

1. The role of electron-positron plasma has not received the appropriate attention in the days of precision Big-Bang nucleosynthesis studies. The standard BBN model indicates that the synthesis of light elements typically takes place at temperatures around $86 \text{ keV} > T_{BBN} > 50 \text{ keV}$ [Pitrou et al. (2018)]. Within this temperature range there are millions of electron-positron pairs per charged nucleon, providing an electron-positron-rich plasma environment for nucleosynthesis which leads to modifications in the Coulomb potential due to the screening effect. Furthermore, the electron-positron densities can reach millions of times normal atomic densities. The presence of these $e\bar{e}$ -pairs before and during BBN has been acknowledged by Wang, Bertulani and Balantekin [Wang et al. (2011)] nearly a decade ago.

2. The Universe today is filled with magnetic fields at various scales and strengths both within galaxies and in deep extra-galactic space. The origin of these magnetic fields is currently unknown. In the early Universe, when temperature $T > 20$ keV, we have dense e^\pm plasma. The significant magnetic moments of electrons and positrons also provide opportunities to investigate spin magnetization process.

Understanding the abundances of muons and electrons/positrons provides essential insights into the evolution of the primordial Universe. In the following we discuss the muon density at persistence temperature in section 5.2, and explore the electron/positron plasma properties, including the damped rate and magnetization in section 5.3.

5.2 Muon–antimuon in the early Universe

Our interest in strangeness flavor freeze-out in the early Universe requires the understanding of the abundance of muons in the early Universe. The specific question needing an answer is at which temperature muons remain in abundance (chemical) equilibrium established predominantly by electromagnetic and weak interaction processes, allowing detailed-balance back-reactions to influence strangeness abundance.

In the early Universe in the the cosmic plasma muons of mass $m_\mu = 105.66$ MeV can be produced by the following interaction processes

$$\gamma + \gamma \longrightarrow \mu^+ + \mu^-, \quad e^+ + e^- \longrightarrow \mu^+ + \mu^-, \quad (5.5)$$

$$\pi^- \longrightarrow \mu^- + \bar{\nu}_\mu, \quad \pi^+ \longrightarrow \mu^+ + \nu_\mu. \quad (5.6)$$

The back reactions for all above processes are in detailed balance, provided all particles shown on the right hand side (RHS) exist in chemical abundance equilibrium in the Universe. We recall the empty space (no plasma) at rest lifetime of pions $\tau_\pi = 2.6033 \times 10^{-8}$ sec.

However, all produced muons can also decay via the reactions

$$\mu^- \rightarrow \nu_\mu + e^- + \bar{\nu}_e, \quad \mu^+ \rightarrow \bar{\nu}_\mu + e^+ + \nu_e, \quad (5.7)$$

with the empty space (no plasma) at rest lifetime $\tau_\mu = 2.197 \times 10^{-6}$ sec. We thus must establish the range of temperature in which production processes exceed in speed the decay process.

The temperature range of our interests is the Universe when $m_\mu \gg T$. In this case the Boltzmann approximation is appropriate for studying massive particles muons and pions. The thermal decay rate per volume and time for muons μ^\pm (and pions π^\pm) in the Boltzmann limit are given by [Kuznetsova and Rafelski (2010b)]:

$$R_\mu = \frac{g_\mu}{2\pi^2} \left(\frac{T^3}{\tau_\mu} \right) \left(\frac{m_\mu}{T} \right)^2 K_1(m_\mu/T), \quad (5.8)$$

$$R_\pi = \frac{g_\pi}{2\pi^2} \left(\frac{T^3}{\tau_\pi} \right) \left(\frac{m_\pi}{T} \right)^2 K_1(m_\pi/T), \quad (5.9)$$

where the lifespan of μ^\pm and π^\pm in the vacuum were given above. This rate accounts for both the density of particles in chemical abundance equilibrium and the effect of time dilation present when particles are in thermal motion with respect to observer at rest in the local reference frame. The effects of Fermi blocking or boson stimulated emission have been neglected.

The thermal averaged reaction rate per volume for the reaction $a\bar{a} \rightarrow b\bar{b}$ in Boltzmann approximation is given by [Letessier and Rafelski (2002)]

$$R_{a\bar{a} \rightarrow b\bar{b}} = \frac{g_a g_{\bar{a}}}{1 + I} \frac{T}{32\pi^4} \int_{s_{th}}^{\infty} ds \frac{s(s - 4m_a^2)}{\sqrt{s}} \sigma_{a\bar{a} \rightarrow b\bar{b}} K_1(\sqrt{s}/T), \quad (5.10)$$

where s_{th} is the threshold energy for the reaction, $\sigma_{a\bar{a} \rightarrow b\bar{b}}$ is the cross section for the given reaction, and K_1 is the modified Bessel function of integer order "1". We introduce the factor $1/(1 + I)$ to avoid the double counting of indistinguishable pairs of particles; we have $I = 1$ for an identical pair and $I = 0$ for a distinguishable pair.

The leading order invariant matrix elements for the reactions $e^+ + e^- \rightarrow \mu^+ + \mu^-$

and $\gamma + \gamma \rightarrow \mu^+ + \mu^-$, are introduced in this work by [Kuznetsova et al. (2008)]

$$|M_{e\bar{e} \rightarrow \mu\bar{\mu}}|^2 = 32\pi^2\alpha^2 \frac{(m_\mu^2 - t)^2 + (m_\mu^2 - u)^2 + 2m_\mu^2 s}{s^2}, \quad m_\mu \gg m_e, \quad (5.11)$$

$$|M_{\gamma\gamma \rightarrow \mu\bar{\mu}}|^2 = 32\pi^2\alpha^2 \left[\left(\frac{m_\mu^2 - u}{m_\mu^2 - t} + \frac{m_\mu^2 - t}{m_\mu^2 - u} \right) + 4 \left(\frac{m_\mu^2}{m_\mu^2 - t} + \frac{m_\mu^2}{m_\mu^2 - u} \right) \right. \\ \left. - 4 \left(\frac{m_\mu^2}{m_\mu^2 - t} + \frac{m_\mu^2}{m_\mu^2 - u} \right)^2 \right], \quad (5.12)$$

where s, t, u are the Mandelstam variables. The cross section required in Eq. (5.10) can be obtained by integrating the matrix elements Eq. (5.11) and Eq. (5.12) over the Mandelstam variable t [Kuznetsova and Rafelski (2010b)]. We have

$$\sigma_{e\bar{e} \rightarrow \mu\bar{\mu}} = \frac{64\pi\alpha^2}{48\pi} \left(\frac{1 + 2m_\mu^2/s}{s - 4m_e^2} \right) \sqrt{1 - \frac{4m_\mu^2}{s}}, \quad (5.13)$$

$$\sigma_{\gamma\gamma \rightarrow \mu\bar{\mu}} = \frac{\pi}{2} \left(\frac{\alpha}{m_\mu} \right)^2 (1 - \beta^2) \left[(3 - \beta^4) \ln \frac{1 + \beta}{1 - \beta} - 2\beta(2 - \beta^2) \right], \quad (5.14)$$

$$\beta = \sqrt{1 - 4m_\mu^2/s} \quad (5.15)$$

Substituting the cross sections into Eq. (5.10) we obtain the production rates for $e\bar{e} \rightarrow \mu\bar{\mu}$ and $\gamma\gamma \rightarrow \mu\bar{\mu}$ respectively.

In Fig. 5.1 we show the invariant thermal reaction rates per volume and time for rates of relevance, as a function of temperature T . As the temperature decreases in the expanding Universe, the initially dominant production rates ($e\bar{e}, \gamma\gamma \rightarrow \mu\bar{\mu}$) decrease with decreasing temperature, and eventually cross the μ^\pm decay rates. Muon abundance disappears as soon as any decay rate is faster than the fastest production rate. Specifically after the Universe cools below the temperature $T_{\text{disappear}} = 4.195$ MeV, the dominant reaction is the muon decay. Due to the relatively slow expansion of the Universe, the disappearance of muons is sudden, and the abundance of muons vanishes as soon as a decay rate surpasses the dominant production rate.

On the other hand, considering the number density for nonrelativistic μ^\pm in the Boltzmann approximation, we have

$$n_{\mu^\pm} = \frac{g_{\mu^\pm}}{2\pi^2} T^3 \left(\frac{m_\mu}{T} \right)^2 K_2(m_\mu/T) = g_{\mu^\pm} \left(\frac{m_\mu T}{2\pi} \right)^{3/2} e^{-m_\mu/T}. \quad (5.16)$$

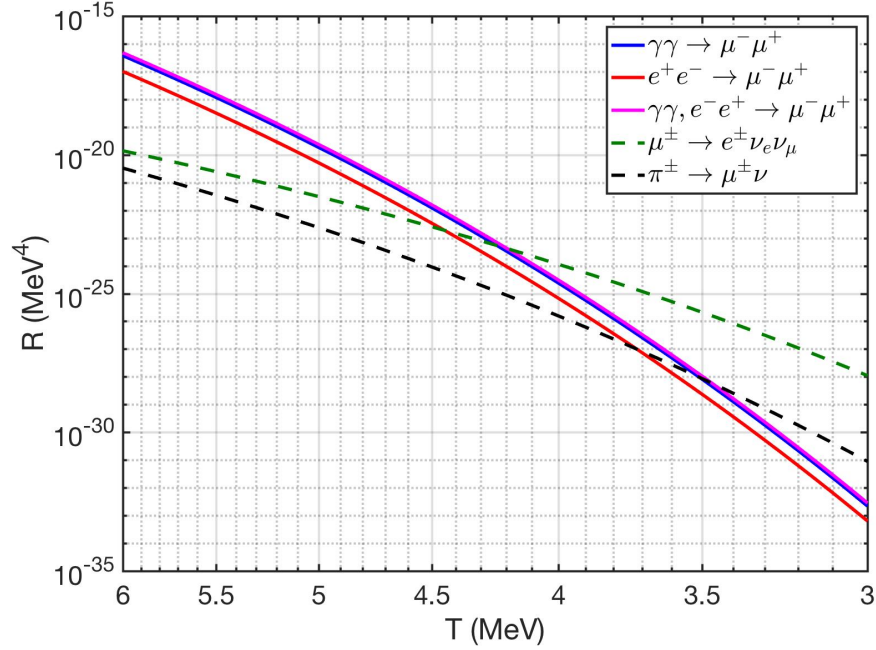


Figure 5.1: We plot the thermal reaction rate per volume for different reactions as a function of temperature. We found that dominant reactions for μ^\pm production are $\gamma + \gamma \rightarrow \mu^+ + \mu^-$ and $e^+ + e^- \rightarrow \mu^+ + \mu^-$, and the total production rate crosses the decay rate of μ^\pm at temperature $T_{disappear} \approx 4.195$ MeV.

then the number density between n_{μ^\pm} and baryon n_B can be written as

$$\frac{n_{\mu^\pm}}{n_B} = \frac{n_{\mu^\pm}}{s} \frac{s}{n_B} = \frac{n_{\mu^\pm}}{s} \left(\frac{s}{n_B} \right)_{t_0}, \quad (5.17)$$

where we used that s/n_B remains constant and t_0 represent present day value. The present value is given by $(n_B/s)_{t_0} \approx 8.69 \times 10^{-11}$ (detail please see Chapter 1). The entropy density s can be characterized introducing g_*^s , the total number of ‘entropic’ degrees of freedom

$$s = \frac{2\pi^2}{45} g_*^s T^3. \quad (5.18)$$

For temperature $10 \text{ MeV} > T > 3 \text{ MeV}$, the massless photons, nearly relativistic electron/positrons, and practically massless neutrinos contribute to the degree of freedom g_*^s . In this case, the number density between n_{μ^\pm} and baryon n_B in the

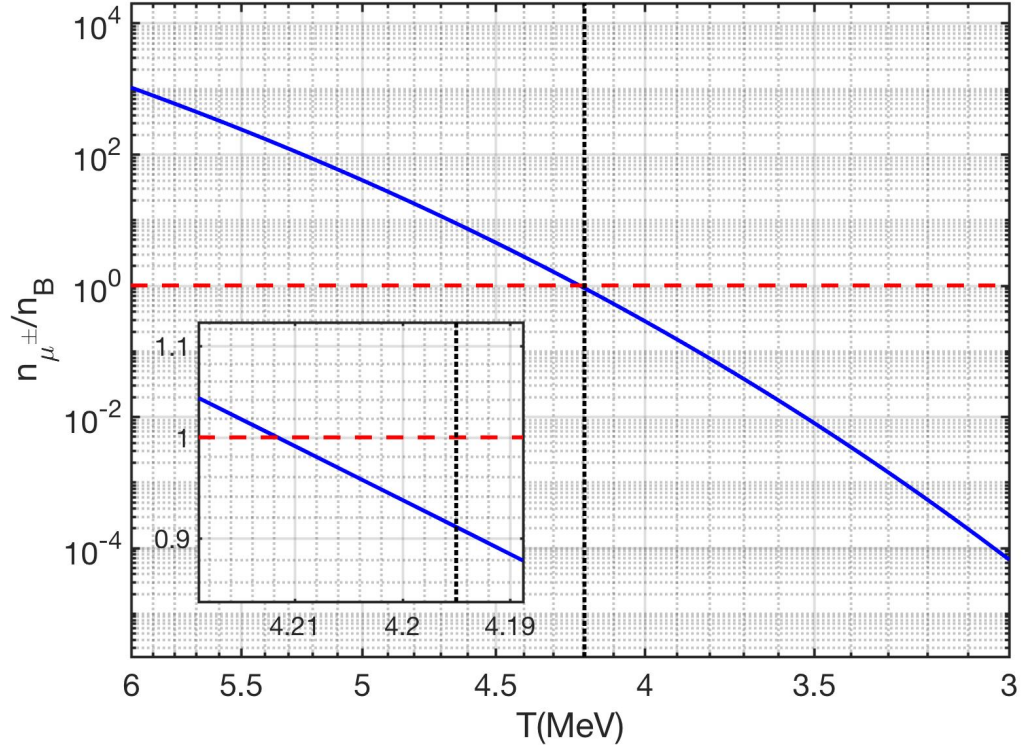


Figure 5.2: The density ratio between μ^\pm and baryons as a function of temperature. The density ratio at muon disappearance temperature is about $n_{\mu^\pm}/n_B(T_{\text{disappear}}) \approx 0.911$, and around the temperature $T \approx 4.212$ MeV the density ratio $n_{\mu^\pm}/n_B \approx 1$.

temperature interval we consider $10 \text{ MeV} > T > 3 \text{ MeV}$ is given by

$$\frac{n_{\mu^\pm}}{n_B} = \frac{45}{2\pi^2} \frac{g_{\mu^\pm}}{g_*^s} \left(\frac{m_\mu}{2\pi T} \right)^{3/2} e^{-m_\mu/T} \left(\frac{s}{n_B} \right)_{t_0}. \quad (5.19)$$

In Fig. 5.2 we show the muon to baryon density ratio Eq. (5.19) as a function of T . We see that the muon abundance $T = 10 \text{ MeV}$ exceeds that of baryons by a factor 500,000 while at muon disappearance temperature $n_{\mu^\pm}/n_B(T_{\text{disappear}}) \approx 0.911$. The number density n_{μ^\pm} and n_B abundances are equal at around the temperature $T_{\text{equal}} \approx 4.212 \text{ MeV} > T_{\text{disappear}}$. This means that the muon abundance may still be able to influence baryon evolution because their number density is comparable to the baryon density.

The primary insight of this work is that aside of protons, neutrons and other non-

relativistic particles, both positively and negatively charged muons μ^\pm are present in thermal equilibrium and in non-negligible abundance for $T > T_{\text{dissappear}} \approx 4.195 \text{ MeV}$. This offers a new and tantalizing model building opportunity for anyone interested in baryon-antibaryon separation in the primordial Universe, strangelet formation, and perhaps other exotic primordial structure formation mechanisms.

5.3 Electron-positron plasma in the early Universe

In the early Universe, after the neutrino freeze-out at $T \approx 2 \text{ MeV}$, the Universe is controlled by the electron-positron-photon plasma. In this section, we demonstrate the rich electron-positron plasma in the early Universe by examining the chemical potential μ_e in the charge-neutral and entropy-conserving Universe. We study the microscope collision property of electron-positron plasma and explore the spin response of the electron-positron plasma to external and self-magnetization fields, thus developing methods for future detailed study.

5.3.1 Electron chemical potential in the early Universe

In this section, we derive the dependence of electron chemical potential, and hence e^\pm density, on the photon background temperature by employing the following physical principles:

1. Charge neutrality of the Universe:

$$n_e - n_{\bar{e}} = n_p - n_{\bar{p}} \approx n_p, \quad (5.20)$$

where n_e and $n_{\bar{e}}$ denotes the number density of electron and positron.

2. Neutrinos decouple (freeze-out) at a temperature $T_f \simeq 2 \text{ MeV}$, after which they free stream through the Universe with an effective temperature [Birrell et al. (2014a)]

$$T_\nu(t) = T_f a(t_f)/a(t), \quad (5.21)$$

where $a(t)$ is the FLRW Universe scale factor.

3. Total comoving entropy is conserved. At $T \leq T_f$ the dominant contributors to entropy are photons, e^\pm , and neutrinos. In addition, after neutrino freeze-out, neutrino comoving entropy is independently conserved [Birrell et al. (2014a)]. This implies that the combined comoving entropy in γ , e^\pm is also conserved for $T_\gamma \leq T_f$.

Motivated by the fact that comoving entropy in γ , e^\pm is conserved after neutrino freeze-out, we rewrite the charge neutrality condition, Eq.(5.20) in the form

$$n_e - n_{\bar{e}} = X_p \frac{n_B}{s_{\gamma,e,\bar{e}}} s_{\gamma,e,\bar{e}}, \quad X_p \equiv \frac{n_p}{n_B}, \quad (5.22)$$

where n_B is the number density of baryons, and $s_{\gamma,e,\bar{e}}$ is the combined entropy density in photons, electrons, and positrons. During the Universe expansion, the comoving entropy and baryon number are conserved quantities, hence the ratio $n_B/s_{\gamma,e,\bar{e}}$ is conserved. We have

$$\frac{n_B}{s_{\gamma,e,\bar{e}}} = \left(\frac{n_B}{s_{\gamma,e,\bar{e}}} \right)_{t_0} = \left(\frac{n_B}{s_\gamma} \right)_{t_0} = \left(\frac{n_B}{n_\gamma} \right)_{t_0} \left(\frac{n_\gamma}{s_\gamma} \right)_{t_0}, \quad (5.23)$$

where the subscript t_0 denotes the present day value, and the second equality is obtained by observing that the present day e^\pm -entropy density is negligible compared to the photon entropy density. We can evaluate the ratio by giving the present day baryon-to-photon ratio: $n_B/n_\gamma = 6.05 \times 10^{-10}$ (CMB) [Workman et al. (2022)] and the entropy per particle for a massless boson: $(s/n)_{\text{boson}} \approx 3.602$ [Letessier and Rafelski (2002)].

The total entropy density of photons and electron/positron can be written as

$$s_{\gamma,e,\bar{e}} = \frac{2\pi^2}{45} g_\gamma T_\gamma^3 + \frac{\rho_{e,\bar{e}} + P_{e,\bar{e}}}{T_\gamma} - \frac{\mu_e}{T_\gamma} (n_e - n_{\bar{e}}), \quad (5.24)$$

where $\rho_{e,\bar{e}} = \rho_e + \rho_{\bar{e}}$ and $P_{e,\bar{e}} = P_e + P_{\bar{e}}$ are the total energy density and pressure of electrons/positron respectively. The energy density and pressure in electrons and positrons are given by

$$\frac{\rho_{e,\bar{e}}}{T_\gamma^4} = \frac{g_e}{2\pi^2} M_e^4 \left[\int_1^\infty \frac{u^2 \sqrt{u^2 - 1} du}{\exp(M_e u - b_e) + 1} + \int_1^\infty \frac{u^2 \sqrt{u^2 - 1} du}{\exp(M_e u + b_e) + 1} \right], \quad (5.25)$$

and

$$\frac{P_{e,\bar{e}}}{T_\gamma^4} = \frac{g_e}{6\pi^2} M_e^4 \left[\int_1^\infty \frac{(u^2 - 1)^{3/2} du}{\exp(M_e u - b_e) + 1} + \int_1^\infty \frac{(u^2 - 1)^{3/2} du}{\exp(M_e u + b_e) + 1} \right], \quad (5.26)$$

where we introduce the dimensionless variables as follows:

$$u = \frac{E}{m_e}, \quad M_e = \frac{m_e}{T_\gamma}, \quad b_e = \frac{\mu_e}{T_\gamma}. \quad (5.27)$$

By incorporating Eq.(5.22) and Eq.(5.24), the charge neutrality condition can be expressed as

$$\begin{aligned} & \left[1 + X_p \left(\frac{n_B}{n_\gamma} \right)_{t_0} \left(\frac{n_\gamma}{s_\gamma} \right)_{t_0} \frac{\mu_e}{T_\gamma} \right] \frac{n_e - n_{\bar{e}}}{T_\gamma^3} \\ & = X_p \left(\frac{n_B}{n_\gamma} \right)_{t_0} \left(\frac{n_\gamma}{s_\gamma} \right)_{t_0} \left(\frac{2\pi^2}{45} g_\gamma + \frac{\rho_{e,\bar{e}} + P_{e,\bar{e}}}{T_\gamma^4} \right). \end{aligned} \quad (5.28)$$

Using the Fermi distribution, the number density of electrons over positrons in the early Universe is given by

$$\begin{aligned} n_e - n_{\bar{e}} &= \frac{g_e}{2\pi^2} \left[\int_0^\infty \frac{p^2 dp}{\exp((E - \mu_e)/T_\gamma) + 1} - \int_0^\infty \frac{p^2 dp}{\exp((E + \mu_e)/T_\gamma) + 1} \right] \\ &= \frac{g_e}{2\pi^2} T_\gamma^3 \tanh(b_e) M_e^3 \int_1^\infty \frac{u \sqrt{u^2 - 1} du}{1 + \cosh(M_e u) / \cosh(b_e)}. \end{aligned} \quad (5.29)$$

Substituting Eq.(5.29) into Eq.(5.28) and giving the value of X_p , the charge neutrality condition can be solved to determine μ_e/T_γ as a function of M_e and T_γ .

In Fig. 5.3 (left axis) we solve Eq.(5.28) numerically and plot the electron chemical potential as a function of temperature with the following parameters: proton concentration $X_p = 0.878$ from observation [Workman et al. (2022)] and $n_B/n_\gamma = 6.05 \times 10^{-10}$ from CMB. We can see the value of chemical potential is comparatively small $\mu_e/T \approx 10^{-6} \sim 10^{-7}$ during the BBN temperature range, implying an equal number of electrons and positrons in plasma. From the ratio of electron (positron) number density to baryon density in Fig. 5.3 (right axis) we can see that during the accepted BBN temperature range the Universe was filled with an electron-positron rich plasma. For example when the temperature is around

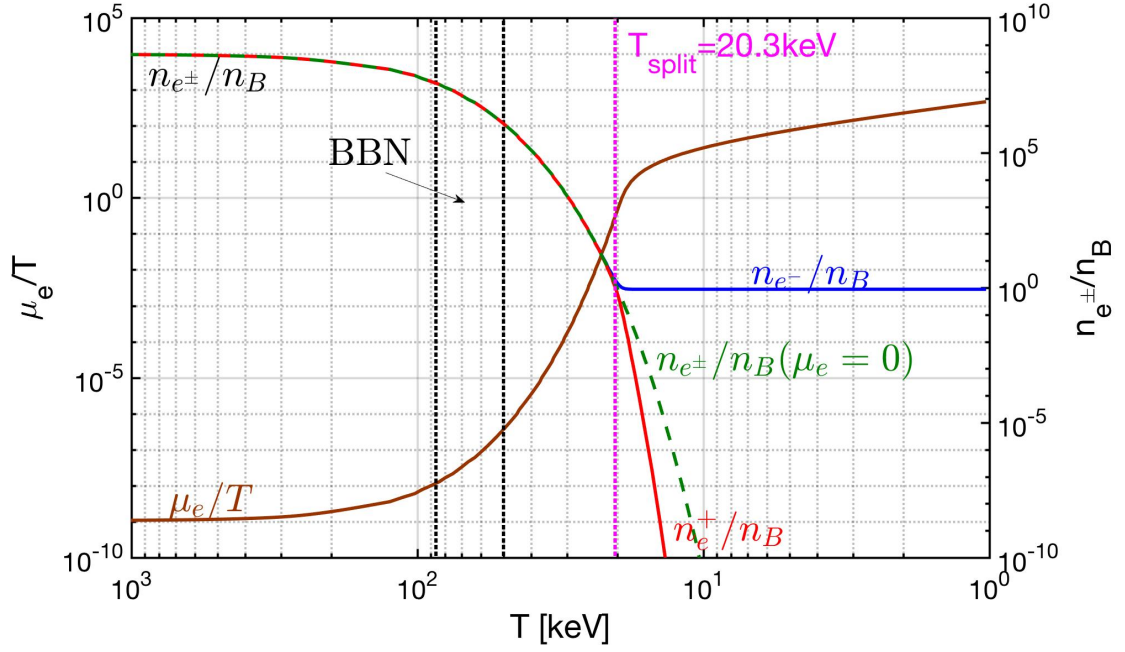


Figure 5.3: Left axis: The chemical potential of an electron as a function of photon temperature $T = T_\gamma$ with $X_p = 0.878$ and $n_B/n_\gamma = 6.05 \times 10^{-10}$. Right axis: the ratio of electron(positron) number density to baryon density as a function of temperature. The blue solid line is the electron density, the red dashed line is the positron density, and the green dotted line is the number density with $\mu_e = 0$. We found that when electron chemical potential $\mu_e \approx T = 0.02$ MeV the positron density decreases because of the annihilation.

$T = 70$ keV the density of electrons and positrons is comparatively large in the early Universe $n_{e^\pm} \approx 10^7 n_B$. Later when the temperature is around $T = 20.3$ keV, the positron density decreases, leading to the transformation of the pair plasma to an electron-proton plasma.

5.3.2 Microscope damping rate of electron-positron plasma

In electron-positron plasma, the major reactions between photons and e^+e^- pairs are inverse Compton scattering, Møller scattering, and Bhabha scattering:

$$e^\pm + \gamma \longrightarrow e^\pm + \gamma, \quad e^\pm + e^\pm \longrightarrow e^\pm + e^\pm, \quad e^\pm + e^\mp \longrightarrow e^\pm + e^\mp. \quad (5.30)$$

The general formula for thermal reaction rate per volume is discussed in [Letessier and Rafelski (2002)] (Eq.(17.16), Chapter 17). For inverse Compton scattering we have

$$R_{e^\pm\gamma} = \frac{g_e g_\gamma}{16 (2\pi)^5} T \int_{m_e^2}^{\infty} ds \frac{K_1(\sqrt{s}/T)}{\sqrt{s}} \int_{-(s-m_e^2)^2/s}^0 dt |M_{e^\pm\gamma}|^2, \quad (5.31)$$

and for Møller and Bhabha reactions we have

$$R_{e^\pm e^\pm} = \frac{g_e g_e}{16 (2\pi)^5} T \int_{4m_e^2}^{\infty} ds \frac{K_1(\sqrt{s}/T)}{\sqrt{s}} \int_{-(s-4m_e^2)}^0 dt |M_{e^\pm e^\pm}|^2, \quad (5.32)$$

$$R_{e^\pm e^\mp} = \frac{g_e g_e}{16 (2\pi)^5} T \int_{4m_e^2}^{\infty} ds \frac{K_1(\sqrt{s}/T)}{\sqrt{s}} \int_{-(s-4m_e^2)}^0 dt |M_{e^\pm e^\mp}|^2, \quad (5.33)$$

where g_i is the degeneracy of particle i , $|M|^2$ is the matrix element for a given reaction, K_1 is the Bessel function of order 1, and s, t, u are Mandelstam variables. The leading order matrix element associated with inverse Compton scattering can be expressed in the Mandelstam variables [Kuznetsova and Rafelski (2012); Kuznetsova et al. (2010)] we have

$$|M_{e^\pm\gamma}|^2 = 32\pi^2 \alpha^2 \left[4 \left(\frac{m_e^2}{m_e^2 - s} + \frac{m_e^2}{m_e^2 - u} \right)^2 - \frac{4m_e^2}{m_e^2 - s} - \frac{4m_e^2}{m_e^2 - u} - \frac{m_e^2 - u}{m_e^2 - s} - \frac{m_e^2 - s}{m_e^2 - u} \right], \quad (5.34)$$

and for Møller and Bhabha scattering we have

$$|M_{e^\pm e^\pm}|^2 = 64\pi^2 \alpha^2 \left[\frac{s^2 + u^2 + 8m_e^2(t - m_e^2)}{2(t - m_\gamma^2)^2} + \frac{s^2 + t^2 + 8m_e^2(u - m_e^2)}{2(u - m_\gamma^2)^2} + \frac{(s - 2m_e^2)(s - 6m_e^2)}{(t - m_\gamma^2)(u - m_\gamma^2)} \right], \quad (5.35)$$

and

$$|M_{e^\pm e^\mp}|^2 = 64\pi^2 \alpha^2 \left[\frac{s^2 + u^2 + 8m_e^2(t - m_e^2)}{2(t - m_\gamma^2)^2} + \frac{u^2 + t^2 + 8m_e^2(s - m_e^2)}{2(s - m_\gamma^2)^2} + \frac{(u - 2m_e^2)(u - 6m_e^2)}{(t - m_\gamma^2)(s - m_\gamma^2)} \right], \quad (5.36)$$

where we introduce the photon mass m_γ to account the plasma effect and avoid singularity in reaction matrix elements.

The photon mass m_γ in plasma is equal to the plasma frequency ω_p , where we have [Kislinger and Morley (1976)]

$$m_\gamma^2 = \omega_p^2 = 8\pi\alpha \int \frac{d^3p_e}{(2\pi)^3} \left(1 - \frac{p_e^2}{3E_e^2}\right) \frac{f_e + f_{\bar{e}}}{E_e}, \quad (5.37)$$

where $E_e = \sqrt{p_e^2 + m_e^2}$. In the BBN temperature range $86 \text{ keV} > T_{BBN} > 50 \text{ keV}$ we have $m_e \gg T$ and considering the nonrelativistic limit for electron-positron plasma, we obtain

$$m_\gamma^2 = \frac{4\pi\alpha}{2m_e} \left(\frac{2m_e T}{\pi}\right)^{3/2} e^{-m_e/T} \cosh\left(\frac{\mu_e}{T}\right). \quad (5.38)$$

In the BBN temperature range, we have $\mu_e/T \ll 1$, which implies the equal number of electrons and positrons in plasma.

To discuss the collisional plasma by the linear response theory, it is convenient to define the average relaxation rate for the electron-positron plasma as follows:

$$\kappa = \frac{R_{e^\pm e^\pm} + R_{e^\pm e^\mp} + R_{e^\pm \gamma}}{\sqrt{n_e - n_{e^+}}} \approx \frac{R_{e^\pm e^\pm} + R_{e^\pm e^\mp}}{\sqrt{n_e - n_{e^+}}}, \quad (5.39)$$

where the density function $\sqrt{n_e - n_{e^+}}$ in the Boltzmann limit is given by

$$\sqrt{n_e - n_{e^+}} = \frac{g_e}{2\pi^3} T^3 \left(\frac{m_e}{T}\right)^2 K_2(m_e/T). \quad (5.40)$$

In Fig. 5.4, we show the reaction rates for Møller reaction, Bhabha reaction, and inverse Compton scattering as a function of temperature. For temperatures $T > 12.0 \text{ keV}$, the dominant reactions in plasma are Møller and Bhabha scatterings between electrons and positrons. Thus in the BBN temperature range, we can neglect the inverse Compton scattering. The total relaxation rate is approximately constant $\kappa = 10 \sim 12 \text{ keV}$ during the BBN. For $T < 20.3 \text{ keV}$ the relaxation rate κ decreases rapidly because of positron annihilation. At this temperature, the composition of plasma begins to change from an electron-positron plasma to an electron-baryon plasma.

From static to damped dynamic screening

At present, the observation of light element (e.g. D, ^3He , ^4He , and ^7Li) abundances produced in Big-Bang nucleosynthesis (BBN) offers a reliable probe of the early

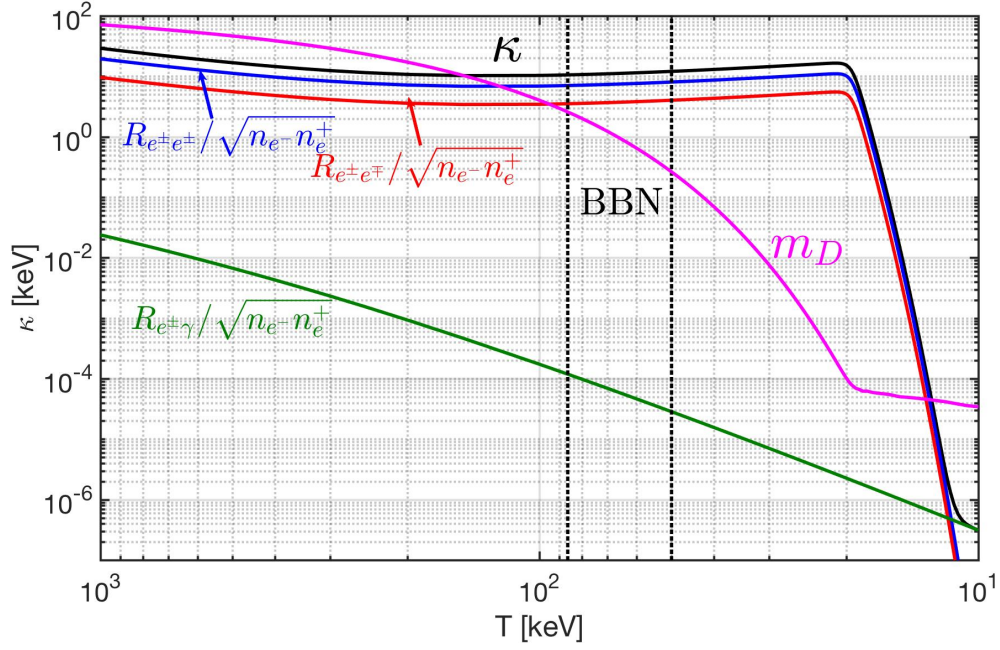


Figure 5.4: The relaxation rate κ as a function of temperature in nonrelativistic electron-positron plasma. For comparison, we show reaction rates for Møller reaction $e^- + e^- \rightarrow e^- + e^-$ (blue line), Bhabha reaction $e^- + e^+ \rightarrow e^- + e^+$ (red line), and inverse Compton scattering $e^- + \gamma \rightarrow e^- + \gamma$ (green line) respectively. It shows that the dominant reactions during BBN are the Møller and Bhabha scatterings between electrons and positrons. The total relaxation rate Eq.(5.39) is shown in the black line. It shows that we have $\kappa = 10 \sim 12$ keV during the BBN temperature range. For comparison, the Debye mass $m_D = \omega_p \sqrt{m_e/T}$ (purple line) is shown as a function of temperature.

Universe before the recombination. Much effort of the BBN study is currently being made to reconcile the discrepancies and tensions between theoretical predictions and observations of light element abundances, e.g. ${}^7\text{Li}$ problem [Pitrou et al. (2018); Fields (2011)]. Current models assume that the Universe was essentially void of anything but reacting light nucleons and electrons needed to keep the local baryon density charge-neutral, a situation similar to the experimental environment where empirical nuclear reaction rates are obtained.

The electron-positron plasma influences light element abundances through electromagnetic screening of the nuclear potential. The electron cloud surrounding the

charge of an ion screens other nuclear charges far from its own radius and reduces the Coulomb barrier. In nuclear reactions, the reduction of Coulomb barrier makes the penetration probability easier and enhance the thermonuclear reaction rates. In this case, the modification of the nuclei interaction due to the plasma screening effect may plays a key role in the formation of light element in the BBN.

The enhancement factor of thermonuclear reaction rates and screening potential are calculated by Salpeter in 1954 [Salpeter (1954)], which describes the static screening effects for the thermonuclear reactions. In an isotropic and homogeneous plasma the Coulomb potential of a point-like particle with charge Ze at rest is modified into [Salpeter (1954)]

$$\phi_{\text{stat}}(r) = \frac{Ze}{4\pi\epsilon_0 r} e^{-m_D r}, \quad (5.41)$$

where m_D is the Debye mass. After that it has been exploited widely in BBN for static screening [Salpeter and van Horn (1969); Famiano et al. (2016)].

Subsequently, the study of dynamical screening for moving ions has been taken into account [Carraro et al. (1988); Gruzinov (1998); Hwang et al. (2021)]. When a test charge moves with a velocity that is enough to react with the background charge in plasma, the Coulomb potential is modified by the dynamical effect. However, the applications focus on the weakly interacting electron-positron plasma only.

In our separate work [Grayson et al. (2023)] we use the linear response theory adapted by C.Grayson to describe the inter nuclear potential in electron-positron plasma during BBN. We improve the prior efforts by evaluation and inclusion of the collision damping rate due to scattering in the dense plasma medium and provide an approximate analytic formula that can be readily used to estimate the effect of screening on internuclear potential. For comprehensive discussion and the application of the damped dynamic screening see [Grayson et al. (2023)].

5.3.3 Magnetization of the electron-positron plasma

In the present-day Universe, we have magnetic fields [Giovannini (2004); Kronberg (1994a,b)] at various scales and strengths both within galaxies and in deep

extra-galactic space far away from matter sources. Current observations suggest the upper and lower bounds for the Extra-Galactic Magnetic Field (EGMF) are given by [Neronov and Vovk (2010); Taylor et al. (2011); Pshirkov et al. (2016); Jedamzik and Saveliev (2019); Vernstrom et al. (2021)]

$$10^{-8}\text{G} > B_{\text{EGFM}} > 10^{-16}\text{G} . \quad (5.42)$$

The origin for EGMF today is currently unknown; different models are considered in lectures [Widrow et al. (2012); Vazza et al. (2021)]. In our work [Rafelski et al. (2023)], we investigate the hypothesis that the observed EGMF are primordial in nature, predating even the recombination epoch. Under this hypothesis, the first best candidate is the electron-positron plasma. This is because for the temperature range $200\text{ keV} > T > 20\text{ keV}$, we still have relatively large quantity of both e^\pm in the the early Universe plasma. In addition, electrons and positrons have the largest magnetic moments in nature, are likely to have been magnetized in the early Universe due to spin orientation. These provide the possibility origins for a primordial magnetic field.

As the Universe undergoes the isentropic expansion, the temperature gradually decreases as $T \propto 1/a(t)$, where $a(t)$ represents the scale factor. The assumption is made that the magnetic flux is conserved over comoving surfaces, implying that the primordial relic field is expected to dilute as $B \propto 1/a(t)^2$ [Rafelski et al. (2023)]. Combining these cosmological redshift relations, we can introduce a dimensionless cosmic magnetic scale that remains unchanged during the evolution of the Universe

$$b \equiv \frac{eB}{T^2} = \left(\frac{eB}{T^2} \right)_{t_0} = b_0 = \text{const.} \quad 10^{-3} > b_0 > 10^{-11} . \quad (5.43)$$

The upper and lower bounds for b_0 are estimated by using the present day EGMF observations Eq. (5.42) and the present CMB temperature $T_0 = 2.7\text{ K} \approx 2.3 \times 10^{-4}\text{ eV}$ [Aghanim et al. (2020b)]. As b_0 is a constant of expansion, this means the contemporary small bounded values of may have once represented large magnetic fields in the early Universe and require detailed study in a different epoch of the Universe. Therefore, correctly describing the dynamics of this e^\pm plasma is of interest when considering the origin of extra-galactic magnetic fields (EGMF).

In the following, we will demonstrate that fundamental quantum statistical analysis can lead to further insights on the behavior of magnetized plasma, and show that the e^\pm plasma is overall paramagnetic and yields a positive overall magnetization, which is contrary to the traditional assumption that matter-antimatter plasma lack significant magnetic responses. For more detailed discussion of electron-positron plasma magnetization, please see [Steinmetz et al. (2023a)].

Electron-positron partition function

To study the statistical behavior of the e^\pm system in a magnetic field, we utilize the general Fermion partition function [Elze et al. (1980)]

$$\ln \mathcal{Z} = \sum_{\alpha} \ln (1 + e^{-\beta(E-\eta)}) , \quad (5.44)$$

where $\beta = 1/T$, α is the set of all quantum numbers in the system, and η is the generalized chemical potential. In the case of a magnetized e^\pm system, we consider it as a system of four quantum species: Particles and antiparticles, and spin aligned and anti-aligned. Taken together, we consider a system where electrons and positrons can be spin aligned or anti-aligned with the magnetic field B and the partition function of the system can be written as

$$\ln \mathcal{Z}_{tot} = \frac{2eBV}{(2\pi)^2} \sum_{\sigma}^{\pm 1} \sum_s^{\pm 1/2} \sum_{n=0}^{\infty} \int_0^{\infty} dp_z [\ln (1 + \Upsilon(x) e^{(\sigma\eta_e + s\eta_s)/T} e^{-\beta E_n^s})] , \quad (5.45)$$

where n is the principle quantum number for the Landau levels. The parameter η_e is the electron chemical potential and η_s is the spin chemical potential [Steinmetz et al. (2023a)]. The parameter $\Upsilon(x)$ is the fugacity of the Fermi gas. In this thesis we will focus on the case $\Upsilon(x) = 1$ and $\eta_s = 0$, we leave the general case $\Upsilon(x) \neq 1$ and $\eta_s \neq 0$ for future work.

In the following, we will retain $\Upsilon(x) = 1$ and consider the case $\eta_s/T \ll 1$ for the first approximation. Then the partition function becomes

$$\ln \mathcal{Z}_{tot} = \frac{2eBV}{(2\pi)^2} \sum_s^{\pm 1/2} \sum_{n=0}^{\infty} \int_0^{\infty} dp_z \left[\ln (1 + e^{-\beta(E_n^s - \eta_e)}) + \ln (1 + e^{-\beta(E_n^s + \eta_e)}) \right]. \quad (5.46)$$

Considering the e^\pm plasma in a uniform magnetic field B pointing along the z -axis, the energy E_n^\pm of electron/positron system can be written as [Rafelski et al. (2023)]

$$E_n^\pm = \sqrt{p_z^2 + \tilde{m}_\pm^2 + 2eBn}, \quad \tilde{m}_\pm^2 = m_e^2 + eB \left(1 \mp \frac{g}{2}\right), \quad (5.47)$$

where the \pm script refers to spin aligned and anti-aligned eigenvalues. The parameter g is the gyro-magnetic (g -factor) of the particle.

To simplify the partition function, we consider the expansion of the logarithmic function as follows:

$$\ln(1+x) = \sum_{k=1}^{\infty} \frac{(-1)^{k+1}}{k} x^k, \quad \text{for } |x| < 1. \quad (5.48)$$

Then the partition function of electron/positron system can be written as

$$\begin{aligned} \ln \mathcal{Z}_{tot} &= \frac{2eBV}{(2\pi)^2} \sum_{n=0}^{\infty} \int_0^{\infty} dp_z \sum_{k=1}^{\infty} \frac{(-1)^{k+1}}{k} \left[e^{k\beta\mu_e} + e^{-k\beta\mu_e} \right] e^{-k\beta E_n^\pm} \\ &= \frac{2eBV}{(2\pi)^2} \sum_{n=0}^{\infty} \sum_{k=1}^{\infty} \frac{(-1)^{k+1}}{k} \left[2 \cosh(k\beta\mu_e) \right] \int_0^{\infty} dp_z e^{-k\beta E_n^\pm}. \end{aligned} \quad (5.49)$$

Using the general definition of Bessel function:

$$K_\nu(\beta m) = \frac{\sqrt{\pi}}{\Gamma(\nu - 1/2)} \frac{1}{m} \left(\frac{\beta}{2m} \right)^{\nu-1} \int_0^{\infty} dp p^{2\nu-2} e^{-\beta E} \quad \text{for } \nu > 1/2, \quad (5.50)$$

the integral over dp_z can be written as

$$\begin{aligned} \int_0^{\infty} dp_z e^{-k\beta E_n^\pm} &= \frac{\Gamma(1/2)}{\sqrt{\pi}} \sqrt{\tilde{m}_\pm^2 + 2eBn} K_1 \left(k \sqrt{\tilde{m}_\pm^2 + 2eBn/T} \right) \\ &= \sqrt{\tilde{m}_\pm^2 + 2eBn} K_1 \left(k \sqrt{\tilde{m}_\pm^2 + 2eBn/T} \right). \end{aligned} \quad (5.51)$$

In this case, the partition function becomes

$$\begin{aligned} \ln \mathcal{Z}_{tot} &= \frac{2eBV}{(2\pi)^2} \sum_{n=0}^{\infty} \sum_{k=1}^{\infty} \frac{(-1)^{k+1}}{k} \left[2 \cosh(k\beta\mu_e) \right] \sqrt{\tilde{m}_\pm^2 + 2eBn} K_1 \left(k \sqrt{\tilde{m}_\pm^2 + 2eBn/T} \right) \\ &= \frac{2eBTV}{(2\pi)^2} \sum_{k=1}^{\infty} \frac{(-1)^{k+1}}{k^2} \left[2 \cosh(k\beta\mu_e) \right] \sum_{n=0}^{\infty} W_1^\pm(n), \end{aligned} \quad (5.52)$$

where we introduce the function $W_1^\pm(n)$ as follows

$$W_1^\pm(n) \equiv \frac{k \sqrt{\tilde{m}_\pm^2 + 2eBn}}{T} K_1 \left(k \sqrt{\tilde{m}_\pm^2 + 2eBn/T} \right). \quad (5.53)$$

Considering the Euler-Maclaurin formula to replace the sum over Landau levels, we have

$$\begin{aligned} \sum_{n=0}^{\infty} W_1^{\pm}(n) &= \int_0^{\infty} dn W_1^{\pm}(n) + \frac{1}{2} \left[W_1^{\pm}(\infty) + W_1^{\pm}(0) \right] \\ &\quad + \frac{1}{12} \left[\left. \frac{\partial W_1^{\pm}}{\partial n} \right|_{\infty} - \left. \frac{\partial W_1^{\pm}}{\partial n} \right|_0 \right] + R, \end{aligned} \quad (5.54)$$

where R is the error remainder which is defined by integrals over Bernoulli polynomials which is small and can be neglected [Elze et al. (1980)]. Using the properties of Bessel function we have

$$\frac{\partial W_1^{\pm}}{\partial n} = -\frac{k^2 e B}{T^2} K_0 \left(k \sqrt{\tilde{m}_{\pm}^2 + 2eBn/T} \right), \quad W_1^{\pm}(\infty) = 0, \quad (5.55)$$

$$\int_a^{\infty} dx x^2 K_1(x) = a^2 K_2(a), \quad (5.56)$$

then we obtain

$$\begin{aligned} \sum_{n=0}^{\infty} W_1^{\pm}(n) &= \left(\frac{T^2}{k^2 e B} \right) \left[\left(\frac{k \tilde{m}_{\pm}}{T} \right)^2 K_2(k \tilde{m}_{\pm}/T) \right] + \frac{1}{2} \left[\left(\frac{k \tilde{m}_{\pm}}{T} \right) K_1(k \tilde{m}_{\pm}/T) \right] \\ &\quad + \frac{1}{12} \left[\left(\frac{k^2 e B}{T^2} \right) K_0(k \tilde{m}_{\pm}/T) \right]. \end{aligned} \quad (5.57)$$

Replacing the sum over Landau levels by the integral, the partition function becomes

$$\ln \mathcal{Z}_{tot} = \ln \mathcal{Z}_{free} + \ln \mathcal{Z}_B, \quad (5.58)$$

where we define the partition functions as

$$\ln \mathcal{Z}_{free} = \frac{T^3 V}{2\pi^2} \left[2 \cosh \left(\frac{\eta_e}{T} \right) \right] \sum_{i=\pm} x_i^2 K_2(x_i), \quad x_i = \frac{\tilde{m}_i}{T} \quad (5.59)$$

$$\ln \mathcal{Z}_B = \frac{e B T V}{2\pi^2} \left[2 \cosh \left(\frac{\eta_e}{T} \right) \right] \sum_{i=\pm} \left[\frac{x_i}{2} K_1(x_i) + \frac{b_0}{12} K_0(x_i) \right]. \quad (5.60)$$

The partition function $\ln(\mathcal{Z}_{free})$ in Eq. (5.59) represents the general form of the Fermi partition function for e^{\pm} with "effective mass" \tilde{m}_{\pm} in our system. When the magnetic field $B = 0$ the function $\ln(\mathcal{Z}_{free})$ will go back to the general form of the Fermi partition function without the external field. The partition function $\ln \mathcal{Z}_B$ gives us the partition with magnetic field effect to the order $\mathcal{O}(eB)$ and $\mathcal{O}(eB)^2$.

In the temperature domain $200 \text{ keV} > T > 20 \text{ keV}$, we have $m_e \gg T$, and it suffices to consider the Boltzmann limit of the quantum distributions. Considering the Boltzmann approximation for non-relativistic electrons and positrons we can rewrite Eq. (5.59) - Eq. (5.60) and obtain

$$\ln \mathcal{Z}_{tot} = \frac{T^3 V}{2\pi^2} \left[2 \cosh\left(\frac{\eta_e}{T}\right) \right] \sum_{i=\pm} \left\{ x_i^2 K_2(x_i) + \frac{b_0}{2} x_i K_1(x_i) + \frac{b_0^2}{12} K_0(x_i) \right\}. \quad (5.61)$$

Given the partition function Eq. (5.61), we can explore the chemical potential and magnetization of e^\pm plasma in the early Universe under the hypothesis of charge neutrality and entropy conservation.

Electron chemical potential under magnetic field

We explore the chemical potential of electron-positron plasma in a uniform magnetic field B in the early Universe under the hypothesis of charge neutrality and entropy conservation. Considering the temperature after neutrino freeze-out, the charge neutrality condition can be written as

$$(n_e - n_{\bar{e}}) = n_p = X_p \left(\frac{n_B}{s_{\gamma,e}} \right) s_{\gamma,e}, \quad X_p \equiv \frac{n_p}{n_B}, \quad (5.62)$$

where n_p and n_B is the number density of protons and baryons respectively. Using the partition function Eq. (5.61), the net number density of electrons in Boltzmann approximation can be written as

$$\begin{aligned} (n_e - n_{\bar{e}}) &= \frac{T}{V} \frac{\partial}{\partial \eta_e} \ln \mathcal{Z}_{tot} \\ &= \frac{T^3}{2\pi^2} [2 \sinh(\eta_e/T)] \sum_{i=\pm} \left[x_i^2 K_2(x_i) + \frac{b_0}{2} x_i K_1(x_i) + \frac{b_0^2}{12} K_0(x_i) \right]. \end{aligned} \quad (5.63)$$

Substituting Eq. (5.63) into the charge neutrality condition Eq. (5.62), we can solve the chemical potential of electron η_e/T numerically. We have

$$\sinh(\eta_e/T) = \frac{2\pi^2}{2T^3} \frac{X_p (n_B/s_{\gamma,e}) s_{\gamma,e}}{\sum_{i=\pm} \left[x_i^2 K_2(x_i) + \frac{b_0}{2} x_i K_1(x_i) + \frac{b_0^2}{12} K_0(x_i) \right]}, \quad (5.64)$$

$$\longrightarrow \frac{2\pi^2 n_p}{2T^3} \frac{X_p (n_B/s_{\gamma,e}) s_{\gamma,e}}{2x^2 K_2(x)}, \quad x = m_e/T, \quad \text{for } b_0 = 0. \quad (5.65)$$

We see in Eq. (5.65) that for the case $b_0 = 0$, the chemical potential agrees with the free particle result in [Grayson et al. (2023)]. In Fig. 5.5 we plot the chemical potential of electron as a function of temperature with different value of b_0 . It shows that the chemical potential is not sensitive to the magnetic field because the small value of $10^{-3} > b_0 > 10^{-11}$ can be neglected in Eq. (5.64).

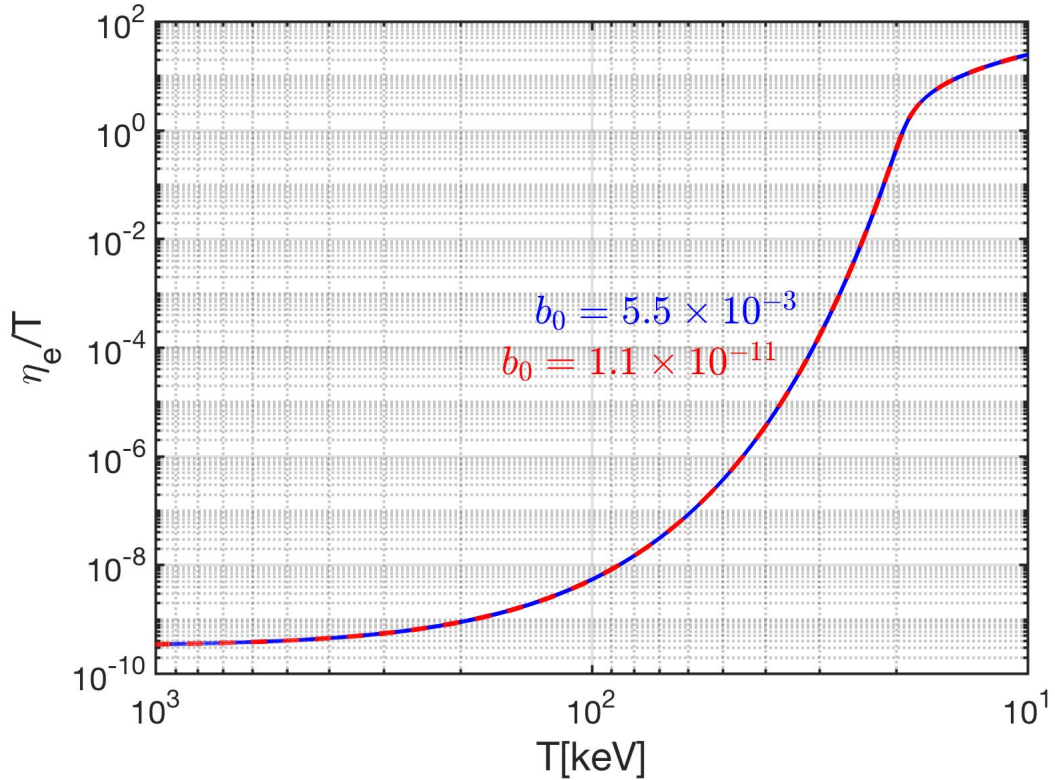


Figure 5.5: The chemical potential of electron as a function of temperature in the magnetic field b_0 with $X_p = 0.878$ and $n_B/n_\gamma = 6.05 \times 10^{-10}$. The red dashed line represents the magnetic field $b_0 = 1.1 \times 10^{-11}$ and blue line labels the magnetic field $b_0 = 5.5 \times 10^{-3}$

Electron-positron magnetization

Considering the magnetized electron-positron partition function Eq. (5.61), it is convenient to introduce the dimensionless magnetization $\overline{\mathcal{M}}$ and the critical field

B_c as follows

$$\overline{\mathcal{M}} \equiv \frac{M}{\mathcal{B}_c} = \frac{1}{\mathcal{B}_c} \left(\frac{T}{V} \frac{\partial \ln \mathcal{Z}_{tot}}{\partial B} \right) \quad \mathcal{B}_c = \frac{m_e^2}{e}. \quad (5.66)$$

Substituting the partition function Eq. (5.61) into Eq. (5.66), the total magnetization $\overline{\mathcal{M}}$ can be broken into the sum of spin parallel $\overline{\mathcal{M}}_+$ and spin anti-parallel $\overline{\mathcal{M}}_-$ magnetization. We have

$$\overline{\mathcal{M}} = \overline{\mathcal{M}}_+ + \overline{\mathcal{M}}_-, \quad (5.67)$$

$$\overline{\mathcal{M}}_{\pm} = \frac{e^2 T^2}{2\pi^2 m_e^2} \left[2 \cosh \left(\frac{\eta_e}{T} \right) \right] \{ c_1(x_{\pm}) K_1(x_{\pm}) + c_0 K_0(x_{\pm}) \}, \quad (5.68)$$

where the coefficients are given by

$$c_1(x_{\pm}) = \left[\frac{1}{2} - \left(\frac{1}{2} \pm \frac{g}{4} \right) \left(1 + \frac{b_0^2}{12x_{\pm}^2} \right) \right] x_{\pm}, \quad c_0 = \left[\frac{1}{6} - \left(\frac{1}{4} \pm \frac{g}{8} \right) \right] b_0. \quad (5.69)$$

Substituting the chemical potential Eq. (5.64) into Eq. (5.67), we can solve the magnetization numerically.

In this thesis we focus on considering the case for $g = 2$. In this case, the electron-positron magnetization can be written as

$$\overline{\mathcal{M}} = \overline{\mathcal{M}}_+ + \overline{\mathcal{M}}_- \quad (5.70)$$

$$\overline{\mathcal{M}}_+ = \frac{e^2 T^2}{\pi^2 m_e^2} \cosh \frac{\eta_e}{T} \left[\frac{1}{2} x_+ K_1(x_+) + \frac{b_0}{6} K_0(x_+) \right], \quad (5.71)$$

$$\overline{\mathcal{M}}_- = -\frac{e^2 T^2}{\pi^2 m_e^2} \cosh \frac{\eta_e}{T} \left[\left(\frac{1}{2} + \frac{b_0^2}{12x_-^2} \right) x_- K_1(x_-) + \frac{b_0}{3} K_0(x_-) \right], \quad (5.72)$$

where x_{\pm} are given by

$$x_+ = \frac{m_e}{T}, \quad x_- = \sqrt{\frac{m_e^2}{T^2} + 2b_0} \quad (5.73)$$

The discussion for the case $g \neq 2$ can be found in [Steinmetz et al. (2023a)].

In Fig. 5.6, we present the magnetization Eq. (5.70) for the case $g = 2$ as a function of temperature. It shows that the magnetization depends on the magnetic scale b_0 and the e^+e^- plasma possesses an overall paramagnetic property, resulting in a positive magnetization $\overline{\mathcal{M}}$. This paramagnetic property is contrary to the

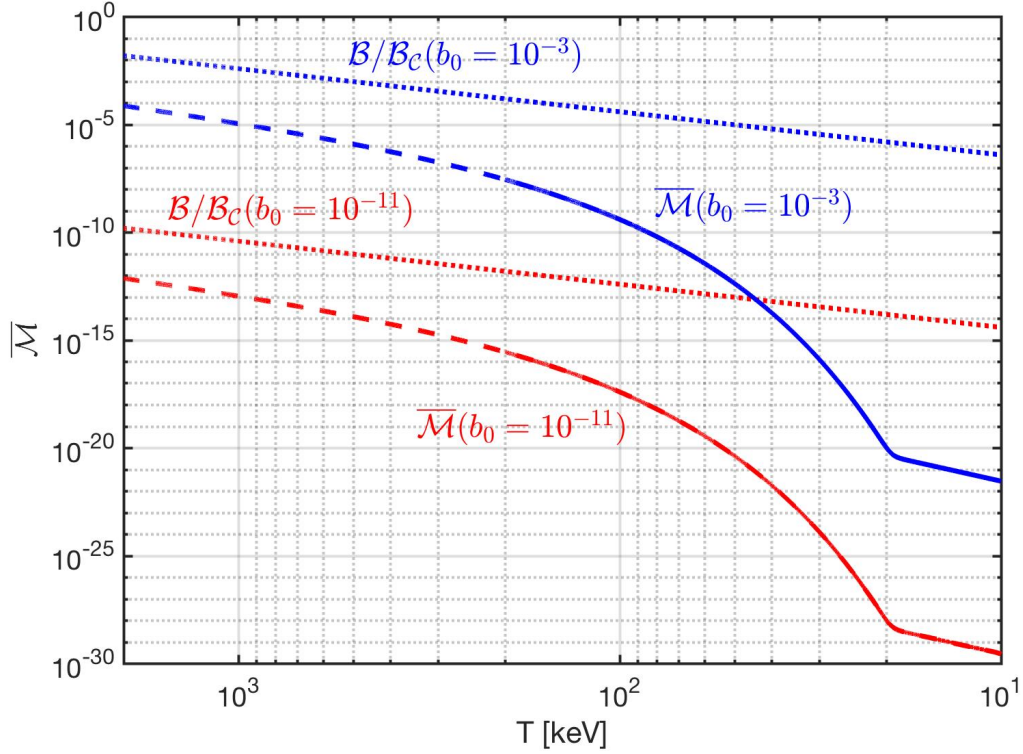


Figure 5.6: The magnetization $\bar{\mathcal{M}} = \mathcal{M}/\mathcal{B}_C$, with $g = 2$, of the primordial e^+e^- plasma is plotted as a function of temperature. The lower (solid red) and upper (solid blue) bounds for cosmic magnetic scale b_0 are included. The external magnetic field strength $\mathcal{B}/\mathcal{B}_C$ is also plotted in for lower (dashed red) and upper (dashed blue) bounds. The spin fugacity is set to unity.

conventional assumption that matter-antimatter plasmas lack significant inherent magnetic responses. However, the magnetization never exceeds the external field under the parameters considered, which shows a lack of ferromagnetic behavior. As the Universe cooled, the dropping magnetization slowed at $T_{\text{split}} = 20.3$ keV, where positrons vanished. Thereafter the remaining electron density diluted with cosmic expansion.

In this section, we have explored the electron-positron plasma considering external and self-magnetization fields without spin potential $\eta_s/T \ll 1$. However the nonzero spin potential $\eta_s \neq 0$ would have an impact on the primordial e^+e^- plasma. In general, the magnetization is also a function of the spin potential η_s , and would

be one important parameter that control the spin direction of primordial gas which allows for magnetization even in the absence of external magnetic fields. For further discussion see [Steinmetz et al. (2023a)].

CHAPTER 6

Outlook: research publications underway

In this chapter, I address the ongoing research projects I hope to complete by the end of year 2023, which include: The low temperature baryogenesis originating in nonequilibrium of bottom flavor; Population of Higgs in the early Universe; Extra neutrino from microscopic processes after freeze-out; and Self-consistent relaxation rate for electron-positron plasma in the early Universe..

6.1 Possibility of bottom-catalyzed low temperature baryogenesis

From the PDG, the observed baryon-to-photon density ratio η today is given by $5.8 \times 10^{-10} \leq \eta \leq 6.5 \times 10^{-10}$ [Tanabashi et al. (2018)] where the $\eta = (6.12 \pm 0.04) \times 10^{-10}$ [Workman et al. (2022)] is used in our calculation. This observed value is the evidence of baryon asymmetry and quantifies the matter-antimatter asymmetry in the Universe. In the past, the small value of the baryon asymmetry could be interpreted as simply due to the initial conditions in the Universe. However, in the current standard cosmological model, the inflation can erase any pre-existing asymmetry between baryons and anti-baryons. In this case, we need baryogenesis to generate of excess of baryon number compared to anti-baryon number in order to create the observed baryon number today.

The precise epoch responsible for the observed matter genesis η in the early Universe has not been established yet. Several mechanisms have been proposed to explain baryogenesis with investigations typically focusing on the temperature range between GUT phase transition $T_G \simeq 10^{16}$ GeV and the electroweak phase transition near $T_W \simeq 130$ GeV [Kuzmin et al. (1985, 1987); Arnold and McLerran (1987); Kolb et al. (1996); Riotto and Trodden (1999); Nielsen and Takanishi (2001); Giudice et al. (2004); Davidson et al. (2008); Morrissey and Ramsey-Musolf (2012)].

In following section we present arguments that the Sakharov conditions [Sakharov (1967)] for matter asymmetry to form also appear during QGP hadronization era near to $T_H \simeq 150 \text{ MeV}$, and show the possibility that bottom catalyzed the baryogenesis.

Overview of Sakharov conditions

In 1967, the Soviet physicist Sakharov first formulated the three conditions necessary to permit baryogenesis in the early Universe [Sakharov (1967)] and in 1991 he refined the three conditions as follows [Sakharov (1990)]:

- Absence of baryonic charge conservation
- Violation of CP-invariance
- Non-stationary conditions in absence of local thermodynamic equilibrium

Since the inflation erases any initial asymmetry between baryons and anti-baryons, the first condition, a violation of baryon number B , must exist to have the present baryon asymmetry. The second Sakharov condition requiring CP violation assures us that we can recognize a universal difference between matter and antimatter, thus one abundance can be enhanced compared to the other.

The third condition, departure from thermal equilibrium, is one of the important prerequisites for matter genesis, this is because it creates the arrow in time for the Universe. In general, the thermal equilibrium implies both chemical (abundance) equilibrium and kinetic (equipartition of energy) equilibrium. The observed baryon and lepton numbers cannot be generated in a full thermal (chemical and kinetic) equilibrium, because even if the required processes are occurring, the net effect is cancelled out by the equal number of back-reactions. We believe that the presence of chemical non-equilibrium is more relevant – kinetic equilibrium is usually established much more quickly and has less impact on the actual particle abundances [Koch et al. (1986); Birrell et al. (2015)].

Chemical non-equilibrium can be achieved by breaking the detailed balance between particle production reaction and annihilation/decay. When the Universe expands and temperature cools down, the production process slows down and is not able to keep up with decay reactions. Then the detailed balance is broken and creates the arrow in time for the Universe. In this case, the third condition of Sakharov can be interpreted as:

- Non-stationary conditions in absence of detailed balance,

where the ideal thermodynamic equilibrium is generalized to the concept of detailed balance.

Is there enough bottom flavor to matter?

Considering that FLRW-Universe evolves conserving entropy, and that baryon and lepton number following on the era of matter genesis is conserved, the current day baryon B to entropy S , B/S -ratio must be achieved during matter genesis. The estimates of present day baryon-to-photon density ratio η allows the determination of the present value of baryon per entropy ratio [Rafelski (2020); Letessier and Rafelski (2002); Fromerth and Rafelski (2002); Fromerth et al. (2012)]:

$$\left(\frac{B}{S}\right)_{t_0} = \eta \left(\frac{n_\gamma}{\sigma_\gamma + \sigma_\nu}\right)_{t_0} = (8.69 \pm 0.05) \times 10^{-11}, \quad (6.1)$$

where the subscript t_0 denotes the present day value, where $\eta = (6.12 \pm 0.04) \times 10^{-10}$ [Tanabashi et al. (2018)] is used in calculation. Here we consider that the Universe today is dominated by photons and free-streaming low mass neutrinos [Birrell et al. (2014a)], and σ_γ and σ_ν are the entropy density for photons and neutrinos, respectively.

In chemical equilibrium the ratio of bottom quark (pair) density n_b^{th} to entropy density $\sigma = S/V$ just above quark-gluon hadronization temperature $T_H = 150 \sim 160$ MeV is $n_b^{th}/\sigma = 10^{-10} \sim 10^{-13}$ (see Fig. 2.1). By studying the bottom density per entropy near to the hadronization temperature and comparing it to the baryon-per-entropy ratio B/S we found there is sufficient abundance of bottom quarks for the proposed matter genesis mechanism to be relevant.

Non-stationary conditions in absence of detailed balance

We have demonstrated that the bottom quark nonequilibrium occurs near to QGP phase transition around the temperature $T = 0.3 \sim 0.15$ GeV in Fig. 2.4 and Fig. 2.6. We demonstrate that the competition between weak interaction decay and the strong interaction fusion processes is responsible for driving the bottom quark departure from the equilibrium in the early Universe. In all cases we see prolonged non-equilibrium which provides the arrow of time for baryogenesis.

Violation of CP -invariance

In general, violation of CP asymmetry can occur in the amplitudes of hadron decay. The weak interaction CP violation arises from the components of Cabibbo-Kobayashi-Maskawa (CKM) matrix associated with quark-level transition amplitude and CP -violating phase.

Given that the non-equilibrium of bottom flavor arises at relatively low QGP temperature, the bottom quark decay occurs from preformed B_x meson states, $x = u, d, s, c$ [Karsch et al. (1988); Brambilla et al. (2010); Aarts et al. (2011); Brambilla et al. (2018); Bazavov et al. (2018); Offler et al. (2019)]. These decays violate aside of the CP symmetry, see for example [Aaij et al. (2020b,a)]. The exploration of the here interesting CP symmetry breaking in $B_c(b\bar{c})$ decay is in progress [Tully (2019); Amhis et al. (2021); Tanabashi et al. (2018)]. Present measurements of CP -violation suggest that the CP asymmetry parameter is around $\delta_{CP} \approx 10^{-3}$ [Tanabashi et al. (2018)].

Nonequilibrium bottom and baryon asymmetry

The off equilibrium phenomenon of bottom quark around the temperature range $T = 0.3 \sim 0.15$ GeV can provide the non-chemical equilibrium condition for baryogenesis to occur in the primordial-QGP hadronization era. Furthermore, let us consider the scenario where all bottom quarks are confined within B_c^\pm meson. In this case, the decay of charged mesons in the primordial-QGP can be a source of CP violation.

However, it remains uncertain whether the decay of B_c^\pm mesons contributes to baryon violation. Our postulation is as follows: the baryon asymmetry is produced by the bottom quark disappearance via the irreversible decay of B_c^\pm meson during the off-equilibrium process. Once a baryon symmetry exists in universe, it will also produce the asymmetry between leptons and anti-leptons which is similar to the baryon asymmetry by the $L = B$.

The heavy B_c^\pm meson decay into multi-particles in plasma is associated with the irreversible process. This is because after decay the daughter particles can interact with plasma and distribute their energy to other particles and reach equilibrium with the plasma quickly. In this case the energy required for the inverse reaction to produce B_c^\pm meson is difficult to overcome and therefore we have an irreversible process for multi-particle decay in plasma.

The rapid B_c^\pm decay and bottom reformation speed at picosecond scale assures that there are millions of individual microscopic processes involving bottom quark production and decay before and during the hadronization epoch of QGP. In this case, we have an Urca process for the bottom quark, i.e. a cycling reaction that produces the bottom quark which subsequently disappears via the B_c^\pm meson decay. The Urca process is a fundamental physical process and has been studying the realms of in astrophysics and nuclear physics. In our case, for bottom quark as a example: at low temperature, the number of bottom quark cycling can be estimated as

$$C_{\text{cycle}}|_{T=0.2\text{GeV}} = \frac{\tau_H}{\tau_{B_c}} \approx 2 \times 10^7, \quad (6.2)$$

where the lifespan of B_c^\pm is $\tau_{B_c} \approx 0.51 \times 10^{-12}$ sec and at temperature $T = 0.2$ GeV the Hubble time is $\tau_H = 1/H = 1.272 \times 10^{-5}$ sec. The Urca process plays a significant role by potentially amplifying any small and currently unobserved violation of baryon number associated with the bottom quark. The small baryon asymmetry is enhanced by the Urca-like process with cycling τ_H^*/τ_* in the early Universe. This amplification would be crucial for achieving the required strength for today's observation.

Full understanding of the possibility for baryogenesis to occur in primordial-

QGP hadronization still requires a detailed study of the relation between baryon asymmetry and irreversible process; we are working on it now. Here, our interest is to show that our results provide a strong motivation to explore the physics of baryon nonconservation involving the bottomonium mesons or/and bottom quarks in thermal environment.

6.2 Population of Higgs in the early Universe

In our earlier study, the bottom (b) quark abundance depends on the competition between the strong interaction fusion and weak interaction decay rates. This lead to the off equilibrium phenomenon of the bottom quark near the hadronization temperature. The same idea can be applied to other heavy particles in QGP. In following we focus on the Higgs abundance first and develop methods for future detailed study.

Considering the temperature range $10 \text{ GeV} > T > 1 \text{ GeV}$ in the early Universe, the number density of the Higgs can be written as

$$n_H = \frac{\Upsilon_H}{2\pi^2} T^3 \left(\frac{m_H}{T} \right)^2 K_2(m_H/T), \quad (6.3)$$

where Υ_H is the Higgs fugacity parameter, and $m_H = 125 \text{ GeV}$ is the mass of Higgs. In the temperature range we consider here, we have $m_H \gg T$ which allows us to consider the Boltzmann limit for the calculation of Higgs number density. Using constant baryon-per-entropy ratio, the density between Higgs and baryon asymmetry (u, d quark-antiquark asymmetry) can be written as

$$\frac{n_H}{(n_B - n_{\bar{B}})} = \frac{n_H}{s_{tot}} \left(\frac{s_{tot}}{n_B - n_{\bar{B}}} \right) = \frac{n_H}{s_{tot}} \left(\frac{s_{\gamma,\nu}}{n_B - n_{\bar{B}}} \right)_{t_0}, \quad (6.4)$$

where the present day value of baryon per entropy ratio is given by Eq. (1.34). The entropy density in QGP can be written as

$$s_{tot} = \frac{2\pi^2}{45} g_*^s T_\gamma^3, \quad g_*^s = \sum_{i=\text{g},\gamma} g_i \left(\frac{T_i}{T_\gamma} \right)^3 + \frac{7}{8} \sum_{i=l^\pm, \nu, u, d} g_i \left(\frac{T_i}{T_\gamma} \right)^3, \quad (6.5)$$

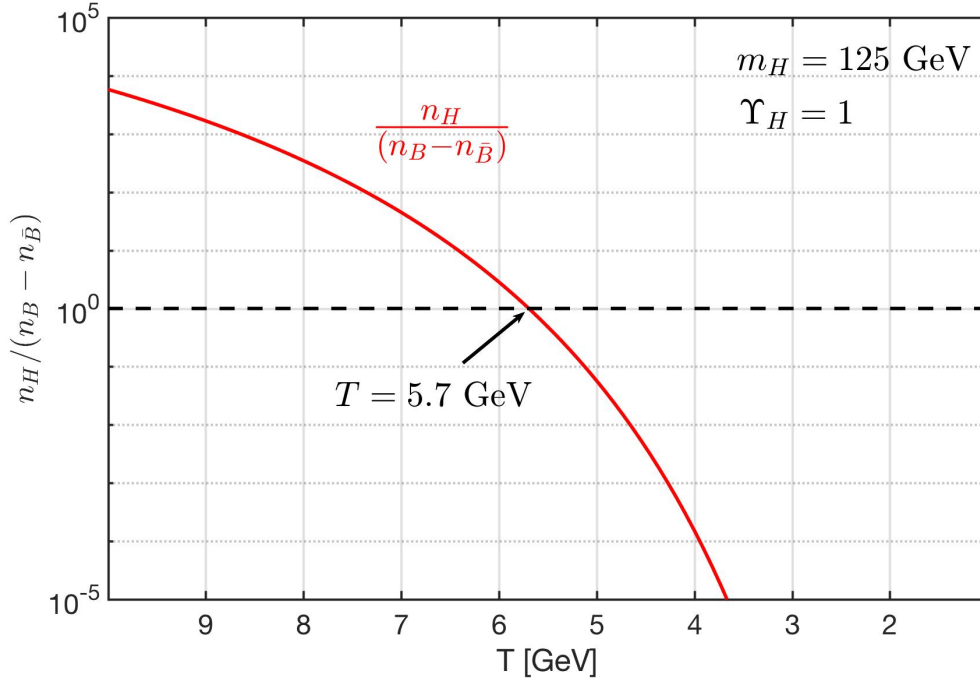


Figure 6.1: The density ratio between Higgs and baryon asymmetry as a function of temperature with condition $\Upsilon_H = 1$. It shows that the $n_H = (n_B - n_{\bar{B}})$ at temperature $T = 5.7$ GeV.

where we consider the massless particles in QGP only as a first estimation. In Fig. 6.1, we plot the density ratio between Higgs and baryon asymmetry for the case $\Upsilon_H = 1$. It shows that at temperature $T = 5.7$ GeV, the ratio is equal to one, i.e., $n_H = (n_B - n_{\bar{B}})$ which means that the Higgs abundance could influence baryon evolution because the Higgs number density is comparable to the baryon number density. This result motivated us to examine the Higgs boson and to study its dynamic abundance in detail during the QGP epoch.

In the QGP epoch, the dominant production of the Higgs boson is the bottom fusion reaction:

$$b + \bar{b} \longrightarrow H, \quad (6.6)$$

which is the inverse decay process of $H \rightarrow b + \bar{b}$. On the other hand, Higgs abundance

disappears via the W, Z decay channel as follows:

$$H \longrightarrow WW^*, ZZ^* \longrightarrow \text{anything}. \quad (6.7)$$

where W^*, Z^* represent the virtual bosons. Once Higgs decays into the W and Z bosons, the short lifespan of W, Z mean they decay into multi-particles and reequilibrate with the plasma quickly. In this case the energy required for the inverse decay reaction to produce the Higgs boson is difficult to overcome in the temperature we are interested in. Similar to the case of bottom quark we studied, the competition between the production and decay of Higgs require the dynamic study of the particle abundance in the early Universe. We aim to apply the knowledge from our study of bottom quark to the Higgs boson, and to examine all other possible sources for Higgs production in QGP and developing methods for future study before the end of year 2023.

6.3 After neutrino freeze-out: Extra neutrinos from microscope processes

After neutrinos chemical freeze-out, the number of neutrinos is independently conserved. However, the presence of electron-positron rich plasma until $T = 20$ keV permits the reaction $\gamma\gamma \rightarrow e^-e^+ \rightarrow \nu\bar{\nu}$ to occur even after neutrinos decouple from the cosmic plasma. This suggests the small amount of extra neutrinos can be produced until temperature $T = 20$ keV and can modify the free streaming distribution and the effective number of neutrinos. In this section, we examine the possible source of extra neutrino from electron-positron plasma and develop methods for future detailed study.

Considering that neutrinos decouple at $T_f = 2$ MeV and become free streaming after freeze-out. The presence of electron-positron plasma environment from $2 \text{ MeV} > T > 0.02 \text{ MeV}$ can allow the following weak reaction to occur:

$$\gamma + \gamma \longrightarrow e^- + e^+ \longrightarrow \nu + \bar{\nu}. \quad (6.8)$$

Given the thermal reaction rate per volume $R_{\gamma\gamma \rightarrow e\bar{e}}$ for reaction $\gamma\gamma \rightarrow e\bar{e}$ and $R_{e\bar{e} \rightarrow \nu\bar{\nu}}$ for reaction $e\bar{e} \rightarrow \nu\bar{\nu}$, then the thermal reaction rate per volume for $\gamma\gamma \rightarrow e^-e^+ \rightarrow$

$\nu\bar{\nu}$ can be written as

$$R_{\gamma\rightarrow e\rightarrow\nu} = R_{\gamma\gamma\rightarrow e\bar{e}} \left(\frac{R_{e\bar{e}\rightarrow\nu\bar{\nu}}}{R_{\gamma\gamma\rightarrow e\bar{e}} + R_{e\bar{e}\rightarrow\nu\bar{\nu}}} \right) \approx R_{e\bar{e}\rightarrow\nu\bar{\nu}} \quad (6.9)$$

In Fig. 6.2 we plot the thermal reaction rate per volume for relevant reactions as a function of temperature $2 \text{ MeV} > T > 0.05 \text{ MeV}$. It shows that the dominant reaction for the process $\gamma\gamma \rightarrow e^-e^+ \rightarrow \nu\bar{\nu}$ is the $e\bar{e} \rightarrow \nu\bar{\nu}$ and can be approximated $R_{\gamma\rightarrow e\rightarrow\nu} = R_{e\bar{e}\rightarrow\nu\bar{\nu}}$ in the temperature we are interested in.

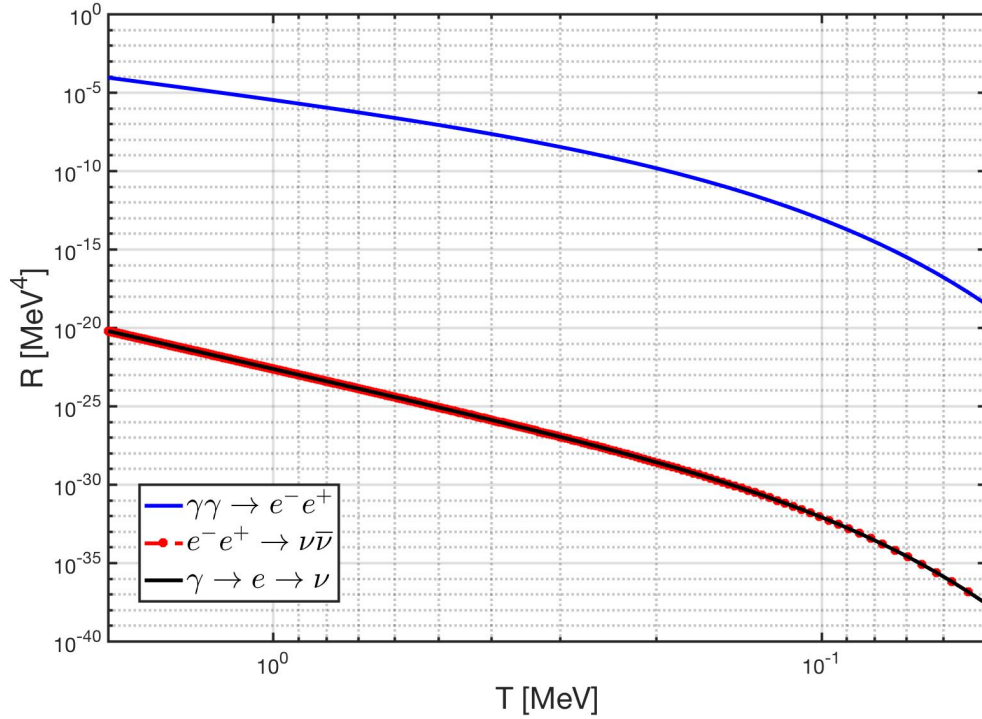


Figure 6.2: The thermal reaction rate per volume as a function of temperature $2 \text{ MeV} > T > 0.05 \text{ MeV}$. The dominant reaction for the process $\gamma\gamma \rightarrow e^-e^+ \rightarrow \nu\bar{\nu}$ is the $e\bar{e} \rightarrow \nu\bar{\nu}$ and we have $R_{\gamma\rightarrow e\rightarrow\nu} = R_{e\bar{e}\rightarrow\nu\bar{\nu}}$.

Given the thermal reaction rate, the dynamic equation describing the relic neutrino abundance after freeze-out can be expressed as:

$$\frac{dn_\nu}{dt} + 3Hn_\nu = R_{e\bar{e}\rightarrow\nu\bar{\nu}}(T_{\gamma,e^\pm}) - R_{\nu\bar{\nu}\rightarrow e\bar{e}}(T_\nu), \quad (6.10)$$

where n_ν is the number density of neutrinos and H is the Hubble parameter. The parameter T_{γ, e^\pm} is the equilibrium temperature between photons and e^\pm and T_ν is the temperature for free-streaming neutrinos:

$$T_\nu = \frac{a(t_f)}{a(t)} T_f, \quad (6.11)$$

where T_f is the neutrino freezeout temperature. After neutrinos decoupled from the cosmic plasma, we have $T_\nu \neq T_{\gamma, e^\pm}$. This is because the conservation of entropy, after freezeout, the relic neutrino entropy is conserved independently and the entropy from e^\pm annihilation flows solely into photons and reheats the photons' temperature. However, after neutrino freezeout, extra entropy from electron-positron plasma can still flow into the free-streaming neutrino sector via the reaction $\gamma\gamma \rightarrow e^-e^+ \rightarrow \nu\bar{\nu}$. To describe this novel situation, kinetic theory for entropy production needs to be adapted, a topic we will address in the future. Here we neglect this extra entropy and consider the standard scenario for first approximation.

In Fig. 6.3 we plot the temperature ratio $T_\nu/T_{\gamma, e^\pm}$, the rate ratio $R_{\nu\bar{\nu} \rightarrow e\bar{e}}/R_{e\bar{e} \rightarrow \nu\bar{\nu}}$ and $(R_{e\bar{e} \rightarrow \nu\bar{\nu}} - R_{\nu\bar{\nu} \rightarrow e\bar{e}})/R_{e\bar{e} \rightarrow \nu\bar{\nu}}$ as a function of temperature. It shows that after neutrino freezeout, the back reaction $\nu\bar{\nu} \rightarrow e\bar{e}$ becomes smaller compared to the reaction $e\bar{e} \rightarrow \nu\bar{\nu}$ as the temperature cools down. This is because as T_ν cools down, the density of relic neutrinos becomes so low and their energy becomes too small to interact. However, the hot and rich electron-positron plasma can still annihilate into neutrino pairs without any difficulties.

Solving the dynamic equation of neutrino abundance Eq.(6.10), the general solution can be written as

$$n_\nu(T) = n_{\text{relic}}(T) + n_{\text{extra}}(T), \quad T = T_{\gamma, e^\pm}, \quad (6.12)$$

where n_{relic} represents the relic neutrino number density and n_{extra} is the extra number density from the e^\pm annihilation. The relic neutrino density is given by

$$n_{\text{relic}} = n_\nu^0 \exp\left(-3 \int_{t_i}^t dt' H(t')\right) = n_\nu^0 \exp\left(3 \int_{T_i}^T \frac{dT'}{T'} (1 + \mathcal{F})\right), \quad (6.13)$$

$$n_\nu^0 = g_\nu \frac{3\zeta(3)}{4\pi^2} T_i^3, \quad F = \frac{T}{3g_s^*} \frac{dg_s^*}{dT}, \quad (6.14)$$

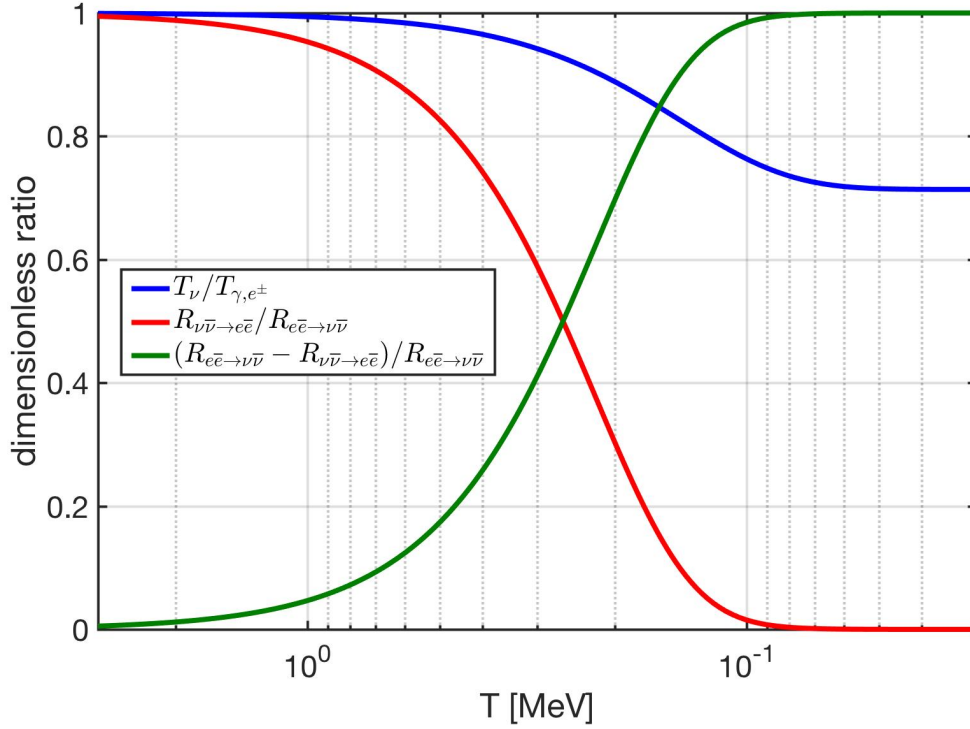


Figure 6.3: The temperature ratio $T_\nu/T_{\gamma,e^\pm}$ (blue line), the rate ratio $R_{\nu\bar{\nu}\rightarrow e\bar{e}}/R_{e\bar{e}\rightarrow\nu\bar{\nu}}$ (red line) and $(R_{e\bar{e}\rightarrow\nu\bar{\nu}} - R_{\nu\bar{\nu}\rightarrow e\bar{e}})/R_{e\bar{e}\rightarrow\nu\bar{\nu}}$ (green line) as a function of temperature. It shows that the reaction $\nu\bar{\nu} \rightarrow e\bar{e}$ is small compare to the reaction $e\bar{e} \rightarrow \nu\bar{\nu}$ as temperature cooling down.

where T_i is the initial temperature and g_s^* is the entropy degrees of freedom. The extra neutrino density can be written as

$$n_{\text{extra}} = -\exp\left(3\int_{T_i}^T \frac{dT'}{T'}(1+\mathcal{F})\right) \times \int_{T_i}^T \frac{dT'}{T'} \frac{R_{e\bar{e}}(T') - R_{\nu\bar{\nu}}(T'_\nu)}{H(T')} (1+\mathcal{F}) \exp\left(-3\int_{T_i}^{T'} \frac{dT''}{T''}(1+\mathcal{F})\right). \quad (6.15)$$

In Fig. 6.4 we plot the ratio between $n_{\text{extra}}/n_{\text{relic}}$ as a function of temperature with different neutrino freeze-out temperature T_f . It shows that the number of extra neutrinos depends strongly on the parameter T_f . This is because the freeze-out temperature determines the timing of the entropy transfer between e^\pm and photon,

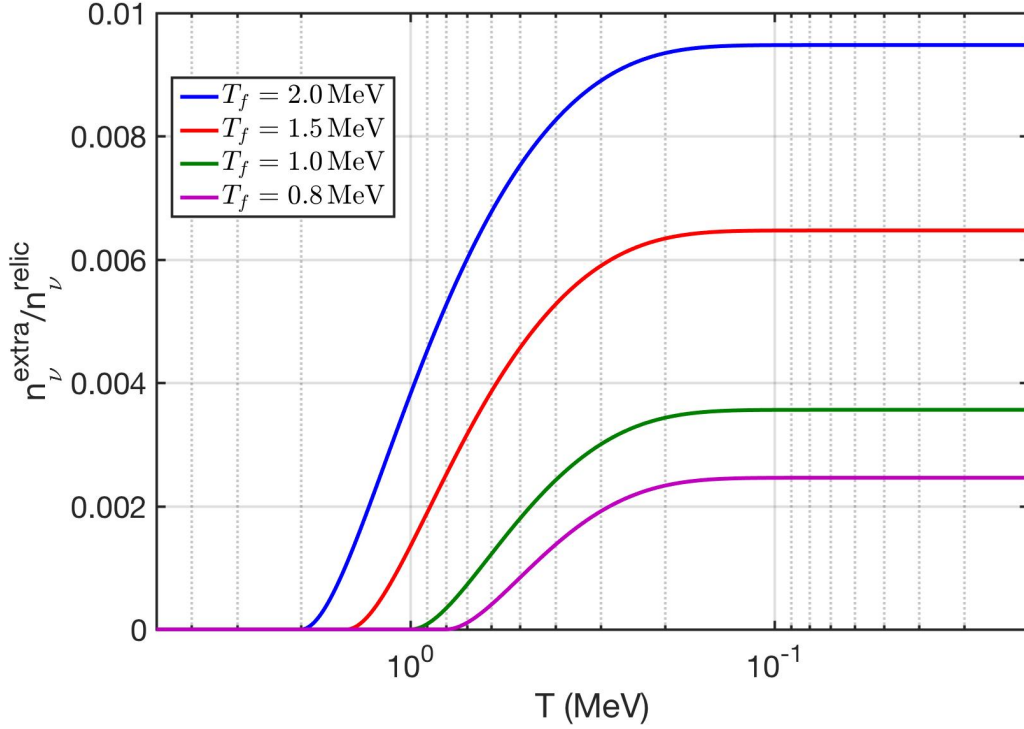


Figure 6.4: the ratio between n_{extra}/n_{relic} as a function of temperature with different neutrino freezeout temperature T_f . It shows that the higher freezeout temperature T_f the higher number of extra neutrinos can be produced.

which subsequently affects the evolution of temperature ratio between neutrinos and photons in the early Universe. The temperature ratio affects the rate ratio between $\nu\bar{\nu} \rightarrow e\bar{e}$ and $e\bar{e} \rightarrow \nu\bar{\nu}$, because once the neutrino is too cold and the back reaction $\nu\bar{\nu} \rightarrow e\bar{e}$ can not maintain the balance, the e^\pm annihilation starts to feed the extra neutrinos to the relic neutrino background.

In addition to the annihilation of electron-positron pairs, there are other sources that can contribute to the presence of extra neutrinos in the early Universe. These additional sources include particle physics phenomena and plasma effects: neutrinos from charged leptons μ^\pm, τ^\pm decay, neutrinos from the π^\pm decay, and neutrino radiation from massive photon decay in electron-positron rich plasma. All of these potential sources of extra neutrinos can impact the distribution of freely streaming

neutrinos and the effective number of neutrinos. Understanding these effects is crucial to comprehending how the neutrino component influences the expansion of the Universe, as well as the potential implications for large-scale structure formation and the spectrum of relic neutrinos.

6.4 The e^\pm plasma relaxation rate: Self-consistence approach

In electron-positron plasma, the photon mass appears as m_γ^2 in the transition matrices for Møller and Bhabha reactions, which is one of important parameters in the calculation of the relaxation rate in e^\pm plasma. When evaluating Møller and Bhabha scattering, we include the temperature-dependent mass of the photon obtained in plasma theory without damping. In general, the effective mass of the photon depends on the property of the plasma. Considering the linear response theory, the dispersion relation for the photon in nonrelativistic e^\pm plasma is given by [Formanek et al. (2021)]

$$w^2 = |k|^2 + \frac{w}{w + i\kappa} w_{pl}^2, \quad (6.16)$$

where w_{pl} is the plasma frequency and κ is the average collision rate of e^\pm plasma. The effective plasma frequency in damped plasma can be solved by considering the case $|k|^2 = 0$ [Formanek et al. (2021)]

$$w_\pm = -i\frac{\kappa}{2} \pm \sqrt{w_{pl}^2 - \frac{\kappa^2}{4}}. \quad (6.17)$$

It shows that the plasma frequency in damped plasma w_\pm is a function of κ . In this case, the effective photon mass in damped plasma is also a function of the scattering rate. We have

$$m_\gamma = w_\pm(w_{pl}, \kappa) = m_\gamma(w_{pl}, \kappa), \quad (6.18)$$

where the photon mass $m_\gamma = w_+$ for the underdamped plasma $w_{pl} > \kappa/2$, and $m_\gamma = w_-$ for overdamped plasma $w_{pl} < \kappa/2$. Eq. (6.18) shows that computed damping strength κ is the dominant scale for collisional plasma and it is also the main parameter determining the photon mass in plasma.

Substituting the effective photon mass Eq. (6.18) into the definition of the average relaxation rate Eq. (5.39), we obtain the self-consistent equation for damping rate κ as

$$\begin{aligned} \kappa & \left[\frac{g_e}{2\pi^3} T^3 \left(\frac{m_e}{T} \right)^2 K_2(m_e/T) \right] \\ & = \frac{g_e g_e}{32\pi^4} T \int_{4m_e^2}^{\infty} ds \frac{s(s-4m_e^2)}{\sqrt{s}} K_1(\sqrt{s}/T) \left[\sigma_{e^\pm e^\pm}(s, w_{pl}, \kappa) + \sigma_{e^\pm e^\mp}(s, w_{pl}, \kappa) \right], \end{aligned} \quad (6.19)$$

where the cross sections depend on the parameter w_{pl} and κ , and the variable κ appears on both sides of the equation so we need solve the equation numerically to determine the κ value that satisfies this condition.

Depending on the nature of the plasma (overdamped or underdamped plasma), we can establish the photon mass in collision plasma based on two distinct conditions as follows:

- Case 1. The plasma frequency is larger than the collision rate $w_{pl} > \kappa/2$, we have

$$m_\gamma = w_+ = -i \frac{\kappa}{2} + \sqrt{w_{pl}^2 - \frac{\kappa^2}{4}}. \quad (6.20)$$

- Case 2. The plasma frequency is smaller than the collision rate $w_{pl} < \kappa/2$, we have

$$m_\gamma = w_- = -i \left(\frac{\kappa}{2} + \sqrt{\frac{\kappa^2}{4} - w_{pl}^2} \right). \quad (6.21)$$

In Fig. 6.5 it shows that during the BBN temperature range $50 \leq T \leq 86$ keV, the plasma frequency is smaller than the collision rate $w_{pl} < \kappa/2$. In this case, the effective photon mass in collision plasma during BBN epoch is given by Eq.(6.21).

To calculate the cross section for Møller and Bhabha scattering we need to include the imaginary photon mass in the calculation of transition matrix elements. In general, the real part of photon mass in the calculation includes the effective photon-electron/positron scattering in plasma, and the imaginary part of photon mass contributes to the decay width of massive photon in plasma. To estimate

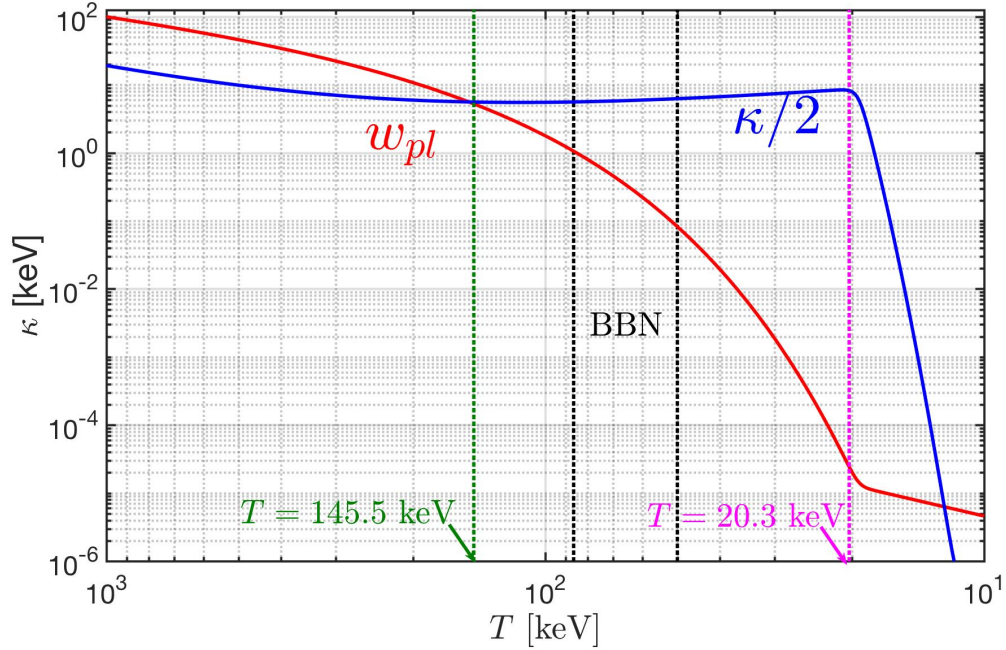


Figure 6.5: The relaxation rate $\kappa/2$ (blue line) as a function of temperature in nonrelativistic electron-positron plasma. For comparison, we show the plasma frequency ω_{pl} in the red line. It shows that for $T > 145.5$ MeV, the plasma frequency is larger than the collision rate $w_{pl} > \kappa/2$; for temperature $T < 145.5$ MeV, we have $\kappa/2 > w_{pl}$. For temperature $T < 20.3$ keV, the composition of plasma is changed to electron and proton, which is beyond our current study because of unequal numbers of electrons and positrons.

the effect of photon mass on the damping rate κ , we first consider the effective mass corresponding to photon-electron/positron scattering in plasma, and leave the photon decay for future study.

For BBN temperature $50 \leq T \leq 86$ keV, we have $w_{pl} < \kappa$ and the effective photon mass can be approximated as

$$\begin{aligned}
 m_\gamma^2 = w_- w_-^* &= \left(\frac{\kappa}{2} + \sqrt{\frac{\kappa^2}{4} - w_{pl}^2} \right)^2 = \frac{\kappa^2}{2} \left[\left(1 - \frac{2w_{pl}^2}{\kappa^2} \right) + \sqrt{1 - \frac{4w_{pl}^2}{\kappa^2}} \right] \\
 &= \frac{\kappa^2}{2} \left[\left(1 - \frac{2w_{pl}^2}{\kappa^2} \right) + \left(1 - \frac{2w_{pl}^2}{\kappa^2} + \dots \right) \right] \approx \kappa^2.
 \end{aligned} \tag{6.22}$$

where we consider the limit $w_{pl}^2/\kappa^2 \ll 1$ and effective photon mass is equal to the

average collision rate in plasma $m_\gamma^2 \approx \kappa$.

Substituting the photon mass $m_\gamma^2 = \kappa^2$ for overdamping plasma into the relaxation rate of electron-positron Eq. (6.19), and introducing the following dimensionless variables

$$x = \sqrt{s}/T, \quad a = m_\gamma/T = \kappa/T, \quad b = m_e/T, \quad (6.23)$$

then the relaxation rate of electron-positron can be written as

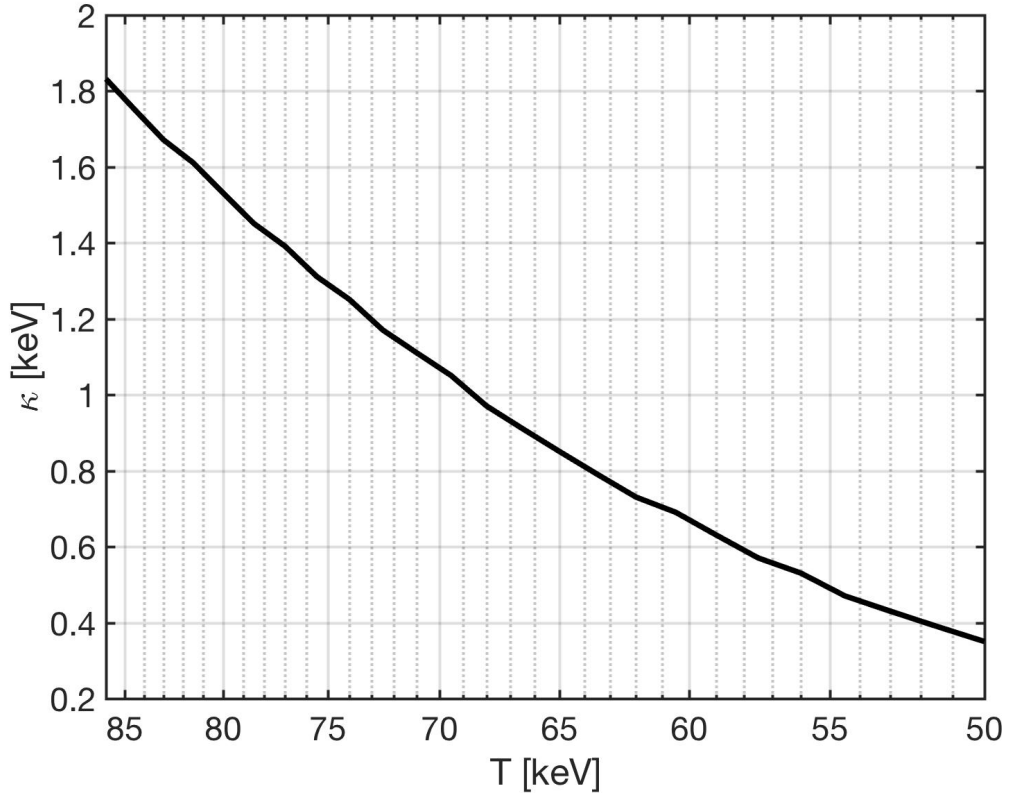


Figure 6.6: The relaxation rate κ that satisfies Eq.(6.24) as a function of temperature $50 \leq T \leq 86$ keV. It shows that for overdamping plasma, we have $m_\gamma^2 = \kappa^2$, and $\kappa = 1.832$ keV when $T = 86$ keV and $\kappa = 0.350$ keV when $T = 50$ keV. The minor fluctuations are a result of the restricted numerical precision.

$$\left[\frac{g_e}{2\pi^2} T^4 \left(\frac{m_e}{T} \right)^2 K_2(m_e/T) \right] \left(\frac{\kappa}{T} \right) = \frac{g_e^2 \alpha^2}{8\pi^3} T^4 \int_{2b}^{\infty} dx K_1(x) [\mathcal{F}_{e^\pm e^\pm}(x, \kappa/T) + \mathcal{F}_{e^\pm e^\mp}(x, \kappa/T)], \quad (6.24)$$

where the functions $\mathcal{F}_{e^\pm e^\pm}$ and $\mathcal{F}_{e^\pm e^\mp}$ are given by

$$\mathcal{F}_{e^\pm e^\pm}(x, a = \kappa/T) = \left\{ 2 \left[3a^2 + 4b^2 + \frac{4(b^4 - a^4)}{x^2 - 4b^2 + 2a^2} \right] \ln \left(\frac{a^2}{x^2 - 4b^2 + a^2} \right) + \frac{(x^2 - 4b^2)(8b^4 + 2a^4 + 3a^2x^2 + 2x^4 - 4b^2(2x^2 + a^2))}{a^2(x^2 - 4b^2 + a^2)} \right\} \quad (6.25)$$

and

$$\mathcal{F}_{e^\pm e^\mp}(x, a = \kappa/T) = \left\{ \frac{2x^2(a^2 + x^2) - 4b^4}{x^2 - a^2} \ln \left(\frac{a^2}{x^2 - 4b^2 + a^2} \right) + \frac{(x^2 - 4b^2)(3x^2 + 4b^2 + 2a^2)}{(x^2 - a^2)} + \frac{x^6 - 12b^4x^2 - 16b^6}{3(x^2 - a^2)^2} + \frac{(x^2 - 4b^2)(8b^4 + 2a^4 + 3a^2x^2 + 2x^4 - 4b^2(2x^2 + a^2))}{a^2(x^2 - 4b^2 + a^2)} \right\}. \quad (6.26)$$

To determine the κ that satisfies Eq. (6.24), we can solve it numerically. In Fig. 6.6, we plot the relaxation rate κ that satisfies Eq. (6.24) as a function of temperature $50 \text{ keV} \leq T \leq 86 \text{ keV}$. It shows that during the BBN temperature range, we have overdamping electron/positron plasma $w_{pl} < \kappa$, and the effective photon mass $m_\gamma^2 = \kappa^2$. The relaxation rate $\kappa = 1.832 \sim 0.350 \text{ keV}$ during the BBN temperature range, which is smaller than the relaxation rate without damping photon mass (See Fig. 5.4, where the relaxation rate $\kappa = 10 \sim 12 \text{ keV}$ during the BBN temperature).

Our first estimation implies that the relaxation rate is sensitive to the photon mass in damped plasma. To address the self-consistent evaluation of damping rate in plasma requires the development of a well-defined, self-consistent approach, where both damping and photon properties in plasma are determined in a mutually consistent manner. We aim to include the full photon mass effect (both real and imaginary parts) in the study and improve our calculation for the next step to complete the project.

CHAPTER 7

Summary and conclusion

We have studied the evolution of the early Universe from the QGP epoch to the e^\pm plasma $300 \text{ MeV} > T > 0.02 \text{ MeV}$. Our effort focuses on understanding how the plasma state impacts and modifies elementary interactions between particles and thus the properties of the early Universe. In the QGP epoch, we investigate the heavy-quark bottom and charm near the QGP hadronization temperature $300 \text{ MeV} > T > 150 \text{ MeV}$. We show that the faster quark-gluon pair fusion keeps the charm quarks in chemical equilibrium up until hadronization. After hadronization, charm quarks form heavy mesons that decay quickly into multi-particles and causes charm quarks to vanish from inventory of particles in the Universe. For the bottom quarks, the quark production rate competes with bottom decay rate as a function of temperature. When the Universe's temperature is near to the QGP phase transition $300 \text{ MeV} > T > 150 \text{ MeV}$, the bottom quark breaks the detail balance and disappearance from particle inventory provides the arrow in time and which can be the 'sweet-spot' for Sakharov conditions.

After hadronization, the free quarks and gluons become confined within baryon/mesons and the Universe becomes hadronic-matter dominated. In the temperature range $150 \text{ MeV} > T > 20 \text{ MeV}$, the Universe is rich in physics phenomena involving strange mesons and (anti)baryons including (anti)hyperon abundances. Considering the inventory of the Universe with strange mesons and baryons, the antibaryons disappear from the Universe at temperature $T = 38.2 \text{ MeV}$. Strangeness can be produced by the inverse decay reactions via weak, electromagnetic, and strong interactions in the early Universe until $T \approx 13 \text{ MeV}$. For $T > 20 \text{ MeV}$, the strangeness is dominantly present in the meson. For $20 > T > 13 \text{ MeV}$, the strangeness can present in the hyperons and anti-strangeness in kaon keeping symmetry $s = \bar{s}$. Below the temperature $T < 13 \text{ MeV}$ a new regime opens up in which

the tiny residual strangeness abundance in hyperons and is governed by weak decays with no reequilibration with mesons.

When the temperature in the Universe is about $T \approx 10$ MeV, the main ingredients that control the Universe evolution are: photons, neutrinos, electrons and positrons. The massive meson, baryon, and μ^\pm and τ^\pm are also present, but their small number density can be neglected when considering the energy density of the Universe expansion. For temperature $10 \text{ MeV} > T > 2 \text{ MeV}$ the Universe is controlled by the weak interaction between neutrinos and matter. We explore the neutrino coherent and incoherent scatterings with matter and apply them to study the neutrino freeze-out (incoherent scattering) in the early Universe and long wavelength cosmic neutrino-atom scattering (coherent scattering). After neutrino freeze-out $T_f \approx 2 \text{ MeV}$, it becomes free-streaming and the number of neutrinos is independently conserved. We investigate the relation between the lepton number L and the effective number of neutrinos N_ν^{eff} , and explore the impact of a large cosmological lepton asymmetry on the Universe evolution. Instead of $B \simeq |L|$, we found that $0.4 \leq |L| \leq 0.52$ and $B \simeq 1.33 \times 10^{-9} |L|$ reconciles the CMB and current epoch results for the Hubble expansion parameter.

Considering the temperature after neutrino freeze-out: $2 \text{ MeV} > T > 0.02 \text{ MeV}$, the cosmic plasma is dominated by the photon, electrons and positrons. The massive μ^\pm abundance disappears at $T_{\text{disappear}} = 4.195 \text{ MeV}$ as soon as the muon decay rate becomes faster than muon production rate. The muon-baryon density ratio at muon persistence temperature is equal to $n_\mu^\pm/n_B(T_{\text{disappear}}) \approx 0.911$, which implies that the muon abundance could influence baryon evolution because muon number density is comparable to the baryon number density.

We demonstrate that the presence of rich electron-positron plasma can last until temperature $T = 20.3 \text{ keV}$ by calculating the chemical potential of electrons in the universe that maintains charge neutrality and entropy conservation. We evaluate the microscope damping rate with temperature dependent photon mass in electron-positron plasma which is one important variable to study the inter-nuclear electromagnetic potentials in damped plasma. Finally we examine the magnetization

process within dense electron-positron plasma and show that it has paramagnetic properties when subjected to an external field. Our study of magnetization can provide insights to understand the magnetized plasma and the possible origin of primordial magnetic field and developing methods for future detailed study.

Looking forward, we will refine our understanding of the evolution of the early Universe by studying the topics that follow. For electron-positron plasma: we will improve our calculation on the damping rate κ and develop a self-consistent approach where both damping and photon properties in plasma are determined in a mutually consistent manner. For the neutrino sector: we will examine the sources of extra neutrino and entropy transfer from microscope process after neutrino freezeout in details. By studying these phenomena, we aim to enhance our understanding of the role of neutrinos in the evolution of universe. For the heavy particle in QGP: we will focus on understanding the behavior of heavy quarks in extreme environments, and refine our study of nonequilibrium bottom and its potential applications on baryogenesis at low temperature. We will also study the dynamic Higgs abundance under the competition between production and decay to understand the departure from equilibrium of Higgs in the early Universe.

In summary, our research offers an initial glimpse into the first hour of the Universe's history, exploring the intricate relationship between fundamental particles and plasma in the early Universe. We hope that the output of our study will be beneficial to all parties concerned while at the same time contribute to the knowledge enhancement in the understanding of the early Universe.

APPENDIX A

Decomposition of Fermi gas into zero and finite temperature components

The most interesting physics of finite temperature Fermi gasses occurs around the Fermi surface, which needs a mathematical tool that can capture the finite temperature behavior of the Fermi-Dirac distribution in an analytic fashion. We provide a novel form of the Fermi distribution that can separate the Fermi gas into zero and finite temperature components analytically which is useful for addressing physics beyond the zero temperature approximation. This is an ongoing research project and will be submitted to *International Journal of Theoretical Physics*.

A novel form of Fermi distribution

We have empirically identified the following novel way to state the form of the Fermi distribution. We obtained this form while seeking to carry out cosmological computations involving shifts in behavior from high to very low-temperature physics.

$$f \equiv \frac{1}{e^{(E-\tilde{\mu})/T} + 1} = \Theta\left(\frac{\tilde{\mu} - E}{T}\right) + e^{-|E-\tilde{\mu}|/T} \left[\frac{1}{2} \operatorname{sgn}\left(\frac{E - \tilde{\mu}}{T}\right) + \frac{1}{2} \tanh\left(\frac{E - \tilde{\mu}}{2T}\right) \right], \quad (\text{A.1})$$

where the Heaviside step function $\Theta(x)$ and sign function $\operatorname{sgn}(x)$ are given by

$$\Theta(x) = \begin{cases} 1, & \text{for } x > 0 \\ 1/2, & \text{for } x = 0 \\ 0, & \text{for } x < 0 \end{cases}, \quad \operatorname{sgn}(x) = \begin{cases} +1, & \text{for } x > 0 \\ 0, & \text{for } x = 0 \\ -1, & \text{for } x < 0 \end{cases}. \quad (\text{A.2})$$

The first term in Eq. (A.1) represents the zero temperature limit of the Fermi distribution, and the finite temperature contributions in square brackets are weighted by a decaying exponential function. One of the benefits of weighting the finite temperature contributions with decaying exponential function is that it can provide a good

asymptotic limit numerically and the numerical evaluations will naturally center around the Fermi surface of the system.

Mathematical proof

We note that the right hand side (RHS) of Eq. (A.1) comprises several non-analytical functions, also called distributions. On first sight it is hard to believe that these cancel to create the analytical Fermi function format seen on the left hand side (LHS). In the following, we will demonstrate that the two sides equal each other. To demonstrate the novel form of the Fermi distribution, it is convenient to introduce the dimensionless variable as follows:

$$x = \frac{E - \tilde{\mu}}{T}. \quad (\text{A.3})$$

With this dimensionless variable, the Fermi function can be written as

$$f(x) = \Theta(-x) + e^{-|x|} \left[\frac{1}{2} \text{sgn}(x) + \frac{1}{2} \tanh\left(\frac{x}{2}\right) \right]. \quad (\text{A.4})$$

We use following properties of the sign function to help simplify the expression:

$$\text{sgn}(x) \equiv \frac{|x|}{x} \equiv \frac{x}{|x|}, \quad \text{sgn}(0) = 0, \quad \text{sgn}(x) = 2\Theta(x) - 1, \quad (\text{A.5})$$

$$\text{sgn}^2(x) \sinh(x) = \sinh(x). \quad (\text{A.6})$$

Since $\sinh(x)$ vanishes at $x = 0$, we don't need to worry about what value to assign to $\text{sgn}^2(x)$ at $x = 0$. Using the properties above, we can replace the step function and exponential function as follows:

$$\Theta(-x) = \frac{1}{2}(1 - \text{sgn}(x)), \quad (\text{A.7})$$

$$e^{-|x|} = \cosh|x| - \sinh|x| = \cosh x - \text{sgn}(x) \sinh x. \quad (\text{A.8})$$

Then the Fermi distribution function can be written as

$$f = \frac{1}{2} + [\cosh x - \text{sgn}(x) \sinh x - 1] \frac{1}{2} \text{sgn}(x) + [\cosh x - \text{sgn}(x) \sinh x] \frac{1}{2} \tanh(x/2). \quad (\text{A.9})$$

Using the properties of the singular function Eq. (A.6), the distribution function can be written as

$$f = f_R + f_I \quad (\text{A.10})$$

$$f_R = \frac{1}{2} (1 - \sinh x + \cosh x \tanh(x/2)) \quad (\text{A.11})$$

$$f_I = \text{sgn}(x) \frac{1}{2} (\cosh x - 1 - \sinh x \tanh(x/2)), \quad (\text{A.12})$$

where f_R and f_I represent the regular and irregular part of the distribution, respectively.

For the irregular part f_I , we use the properties of hyperbolic functions

$$\cosh x - 1 = 2 \sinh^2(x/2), \quad \sinh x = 2 \sinh(x/2) \cosh(x/2). \quad (\text{A.13})$$

Then it can be written as

$$f_I = \text{sgn}(x) \frac{1}{2} [2 \sinh^2(x/2) - 2 \sinh(x/2) \cosh(x/2) \tanh(x/2)] \quad (\text{A.14})$$

$$= \text{sgn}(x) \frac{1}{2} [2 \sinh^2(x/2) - 2 \sinh^2(x/2)] \quad (\text{A.15})$$

$$= 0. \quad (\text{A.16})$$

We show that the irregular part f_I vanishes as an identity. On the other hand, the regular part f_R can be simplified, as shown below:

$$f_R = \frac{1}{2} \left[1 - \frac{1}{2} (e^x - e^{-x}) + \frac{1}{2} (e^x + e^{-x}) \frac{e^x - 1}{e^x + 1} \right] \quad (\text{A.17})$$

$$= \frac{1}{2(e^x + 1)} \left[(e^x + 1) - \frac{1}{2} [(e^x + 1)(e^x - e^{-x}) - (e^x - 1)(e^x + e^{-x})] \right] \quad (\text{A.18})$$

$$= \frac{1}{2(e^x + 1)} [(e^x + 1) - (e^x - 1)] \quad (\text{A.19})$$

$$= f. \quad (\text{A.20})$$

Finally, we consider the LHS and RHS of Eq. (A.1) at $x = 0$. With the singular function properties as given we see that at $x = 0$ both LHS and RHS of Eq. (A.1) are equal to $1/2$, and in the first derivative of the RHS at $x = 0$ the two $\delta(x)$ -terms

$$\frac{d\Theta((\tilde{\mu} - E)/T)}{dE} = -\frac{1}{T} \delta\left(\frac{\tilde{\mu} - E}{T}\right), \quad \frac{d\text{sgn}((E - \tilde{\mu})/T)}{dE} = \frac{2}{T} \delta\left(\frac{E - \tilde{\mu}}{T}\right), \quad (\text{A.21})$$

cancel exactly as required, since there is no $\delta(x)$ on LHS. This encourages us to believe that all of the singular expressions cancel. This completes the demonstration of the exact validity of Eq. (A.1).

Numerical illustration

In Fig. A.1 we plot the exact Fermi-distribution (LHS of Eq. (A.1)) with solid lines and novel form of Fermi-distribution (RHS of Eq. (A.1)) with dashed lines as a function of energy with different parameters. It demonstrates that the LHS and RHS of Eq. (A.1) are equivalent to each other numerically.

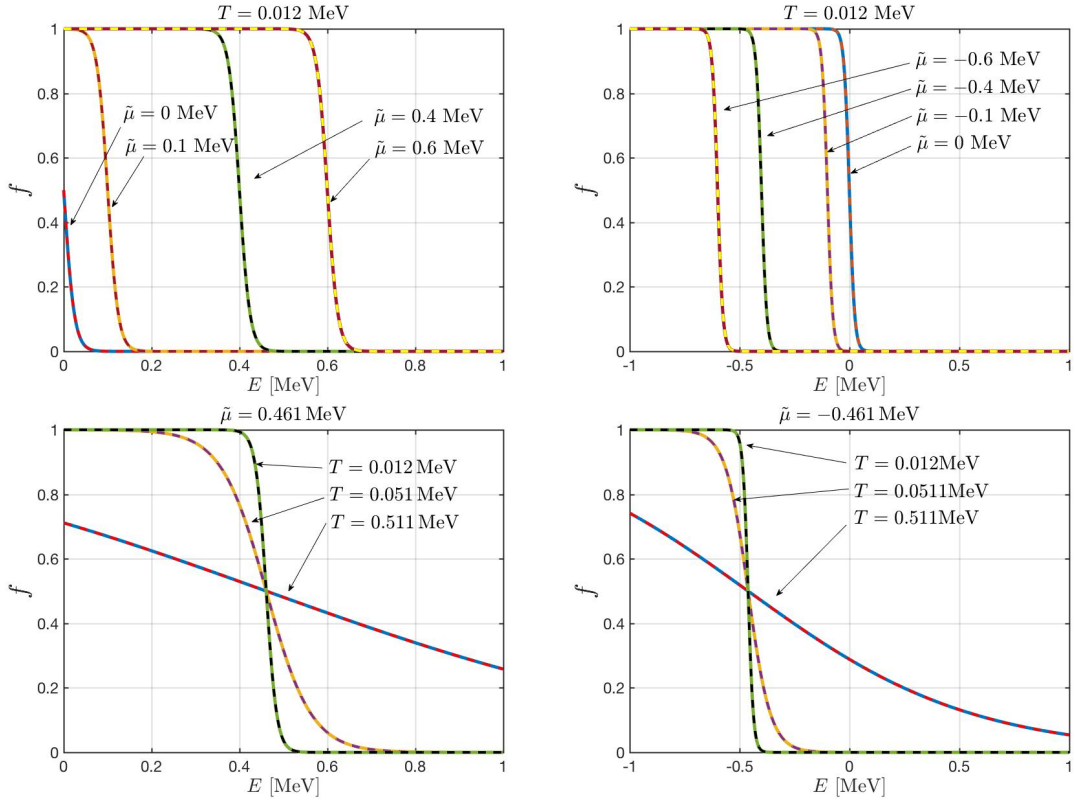


Figure A.1: The exact Fermi-distribution (LHS of Eq. (A.1)) with solid lines and novel form of Fermi-distribution (RHS of Eq. (A.1)) with dashed lines as a function of energy with different parameters. Top: we compare the RHS and LHS of Eq. (A.1) with different chemical potential: $\tilde{\mu} = 0, \pm 0.1, \pm 0.4 \pm 0.6$ MeV at temperature $T = 0.012$ MeV. Bottom: the Fermi distribution with different temperatures $T = 0.511, 0.0511, 0.012$ MeV for chemical potential $\tilde{\mu} = \pm 0.461$ MeV.

To illustrate the zero and finite temperature contribution to the Fermi distribution function, it is convenient to rewrite Eq. (A.1) into the following form

$$f = f_{T=0} + f_{T \neq 0} + \tilde{f}_{T \neq 0} \quad (\text{A.22})$$

where the function are defined as

$$f_{T=0} = \Theta\left(\frac{\tilde{\mu} - E}{T}\right), \quad (\text{A.23})$$

$$f_{T \neq 0} = \frac{1}{2} e^{-|E - \tilde{\mu}|/T} \text{sgn}\left(\frac{E - \tilde{\mu}}{T}\right), \quad \tilde{f}_{T \neq 0} = \frac{1}{2} e^{-|E - \tilde{\mu}|/T} \tanh\left(\frac{E - \tilde{\mu}}{2T}\right) \quad (\text{A.24})$$

In Fig. (A.2) we plot the zero (purple lines, $f_{T=0}$) and finite temperature components of the Fermi distribution as a function of energy choosing in this example the chemical potential $\tilde{\mu} = 0.461$ MeV at temperature $T = 0.02$ MeV and at $T = 0.2$ MeV.

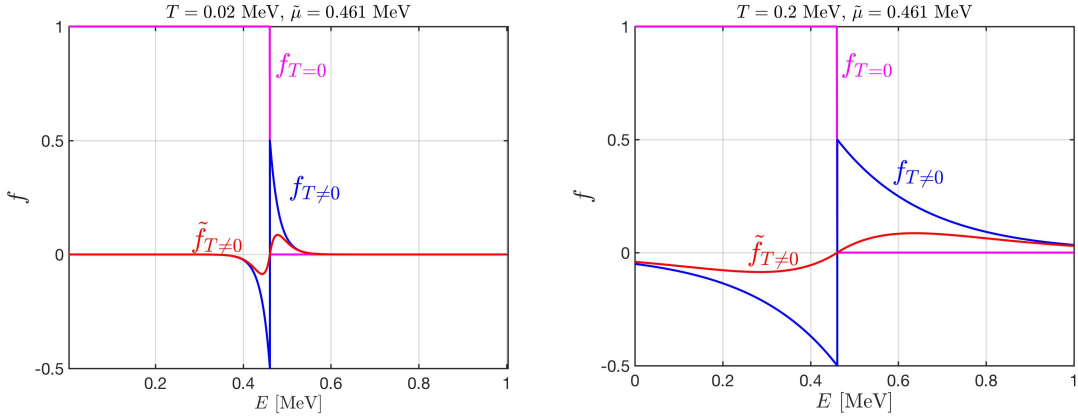


Figure A.2: The zero and finite temperature components of the decomposition here considered for Fermi distribution as a function of energy with chemical potential $\tilde{\mu} = 0.461$ MeV at temperature $T = 0.02$ MeV and $T = 0.2$ MeV. The purple line represents the zero temperature component $f_{T=0}$, and blue and red lines represent the finite temperature components $f_{T \neq 0}$ and $\tilde{f}_{T \neq 0}$ respectively.

This Fig. (A.2) shows that the two finite temperature components $f_{T \neq 0}$ and $\tilde{f}_{T \neq 0}$ are naturally centered around the Fermi surface of the system $E = \tilde{\mu}$. Both finite T always have the same sign, so there is no opportunity generate numerical noise; this can be the case when considering brute force removal of $T = 0$ limit from

the low temperature distribution. The dominant contribution (blue lines, $f_{T \neq 0}$) are containing the decaying exponential function of the Fermi distribution at large argument. The remainder (red lines, $\tilde{f}_{T \neq 0}$) has the shape of a derivative of a finite support representation of delta-function.

REFERENCES

- Aaij, R. et al. (2020a). Measurement of CP observables in $B^\pm \rightarrow DK^\pm$ and $B^\pm \rightarrow D\pi^\pm$ with $D \rightarrow K_S^0 K^\pm \pi^\mp$ decays. *JHEP*, **06**, p. 058. doi:10.1007/JHEP06(2020)058.
- Aaij, R. et al. (2020b). Observation of Several Sources of CP Violation in $B^+ \rightarrow \pi^+ \pi^+ \pi^-$ Decays. *Phys. Rev. Lett.*, **124**(3), p. 031801. doi:10.1103/PhysRevLett.124.031801.
- Aarts, G., C. Allton, S. Kim, M. P. Lombardo, M. B. Oktay, S. M. Ryan, D. K. Sinclair, and J. I. Skullerud (2011). What happens to the Υ and η_b in the quark-gluon plasma? Bottomonium spectral functions from lattice QCD. *JHEP*, **11**, p. 103. doi:10.1007/JHEP11(2011)103.
- Ade, P. A. R. et al. (2014). Planck 2013 results. XVI. Cosmological parameters. *Astron. Astrophys.*, **571**, p. A16. doi:10.1051/0004-6361/201321591.
- Ade, P. A. R. et al. (2016). Planck 2015 results. XIII. Cosmological parameters. *Astron. Astrophys.*, **594**, p. A13. doi:10.1051/0004-6361/201525830.
- Aghanim, N. et al. (2020a). Planck 2018 results. VI. Cosmological parameters. *Astron. Astrophys.*, **641**, p. A6. doi:10.1051/0004-6361/201833910. [Erratum: *Astron. Astrophys.* 652, C4 (2021)].
- Aghanim, N. et al. (2020b). Planck 2018 results. VI. Cosmological parameters. *Astron. Astrophys.*, **641**, p. A6. doi:10.1051/0004-6361/201833910. [Erratum: *Astron. Astrophys.* 652, C4 (2021)].
- Amhis, Y. S. et al. (2021). Averages of b-hadron, c-hadron, and τ -lepton properties as of 2018. *Eur. Phys. J. C*, **81**(3), p. 226. doi:10.1140/epjc/s10052-020-8156-7.
- Anderson, J. and H. Witting (1974). A relativistic relaxation-time model for the Boltzmann equation. *Physica*, **74**(3), pp. 466–488. ISSN 0031-8914. doi:https://doi.org/10.1016/0031-8914(74)90355-3.
- Arnold, P. B. and L. D. McLerran (1987). Sphalerons, Small Fluctuations and Baryon Number Violation in Electroweak Theory. *Phys. Rev. D*, **36**, p. 581. doi:10.1103/PhysRevD.36.581.
- Barenboim, G., W. H. Kinney, and W.-I. Park (2017). Resurrection of large lepton number asymmetries from neutrino flavor oscillations. *Phys. Rev. D*, **95**(4), p. 043506. doi:10.1103/PhysRevD.95.043506.

- Barenboim, G. and W.-I. Park (2017). A full picture of large lepton number asymmetries of the Universe. *JCAP*, **04**, p. 048. doi:10.1088/1475-7516/2017/04/048.
- Bazavov, A., N. Brambilla, P. Petreczky, A. Vairo, and J. H. Weber (2018). Color screening in (2+1)-flavor QCD. *Phys. Rev. D*, **98**(5), p. 054511. doi:10.1103/PhysRevD.98.054511.
- Birrell, J. (2014). *Non-Equilibrium Aspects of Relic Neutrinos: From Freeze-out to the Present Day*. Ph.D. thesis, Arizona U.
- Birrell, J. and J. Rafelski (2015). Quark–gluon plasma as the possible source of cosmological dark radiation. *Phys. Lett. B*, **741**, pp. 77–81. doi:10.1016/j.physletb.2014.12.033.
- Birrell, J., J. Wilkening, and J. Rafelski (2015). Boltzmann Equation Solver Adapted to Emergent Chemical Non-equilibrium. *J. Comput. Phys.*, **281**, pp. 896–916. doi:10.1016/j.jcp.2014.10.056.
- Birrell, J., C.-T. Yang, P. Chen, and J. Rafelski (2013). Fugacity and Reheating of Primordial Neutrinos. *Mod. Phys. Lett. A*, **28**, p. 1350188. doi:10.1142/S0217732313501885.
- Birrell, J., C.-T. Yang, P. Chen, and J. Rafelski (2014a). Relic neutrinos: Physically consistent treatment of effective number of neutrinos and neutrino mass. *Phys. Rev. D*, **89**, p. 023008. doi:10.1103/PhysRevD.89.023008.
- Birrell, J., C.-T. Yang, and J. Rafelski (2014b). Relic Neutrino Freeze-out: Dependence on Natural Constants. *Nucl. Phys. B*, **890**, pp. 481–517. doi:10.1016/j.nuclphysb.2014.11.020.
- Blennow, M., E. Fernandez-Martinez, O. Mena, J. Redondo, and P. Serra (2012). Asymmetric Dark Matter and Dark Radiation. *JCAP*, **07**, p. 022. doi:10.1088/1475-7516/2012/07/022.
- Boehm, C., M. J. Dolan, and C. McCabe (2012). Increasing N_{eff} with particles in thermal equilibrium with neutrinos. *JCAP*, **12**, p. 027. doi:10.1088/1475-7516/2012/12/027.
- Brambilla, N., M. A. Escobedo, J. Ghiglieri, J. Soto, and A. Vairo (2010). Heavy Quarkonium in a weakly-coupled quark-gluon plasma below the melting temperature. *JHEP*, **09**, p. 038. doi:10.1007/JHEP09(2010)038.
- Brambilla, N., M. A. Escobedo, J. Soto, and A. Vairo (2018). Heavy quarkonium suppression in a fireball. *Phys. Rev. D*, **97**(7), p. 074009. doi:10.1103/PhysRevD.97.074009.

- Carraro, C., A. Schafer, and S. E. Koonin (1988). Dynamic Screening of Thermonuclear Reactions. *ApJ*, **331**, p. 565. doi:10.1086/166582.
- Choquet-Bruhat, Y. (2008). *General relativity and the Einstein equations*. OUP Oxford.
- Coc, A., K. A. Olive, J.-P. Uzan, and E. Vangioni (2006). Big bang nucleosynthesis constraints on scalar-tensor theories of gravity. *Phys. Rev. D*, **73**, p. 083525. doi:10.1103/PhysRevD.73.083525.
- Cugnon, J. and R. M. Lombard (1984). K+ PRODUCTION IN A CASCADE MODEL FOR HIGH-ENERGY NUCLEUS NUCLEUS COLLISIONS. *Nucl. Phys. A*, **422**, pp. 635–653. doi:10.1016/0375-9474(84)90369-5.
- Czarnecki, A., W. J. Marciano, and A. Sirlin (2004). Precision measurements and CKM unitarity. *Phys. Rev. D*, **70**, p. 093006. doi:10.1103/PhysRevD.70.093006.
- Davidson, S., E. Nardi, and Y. Nir (2008). Leptogenesis. *Phys. Rept.*, **466**, pp. 105–177. doi:10.1016/j.physrep.2008.06.002.
- Dicus, D. A., E. W. Kolb, A. M. Gleeson, E. C. G. Sudarshan, V. L. Teplitz, and M. S. Turner (1982). Primordial Nucleosynthesis Including Radiative, Coulomb, and Finite Temperature Corrections to Weak Rates. *Phys. Rev. D*, **26**, p. 2694. doi:10.1103/PhysRevD.26.2694.
- Dodelson, S. (2003). *Modern Cosmology*. Academic Press, Amsterdam. ISBN 978-0-12-219141-1.
- Dreiner, H. K., M. Hanussek, J. S. Kim, and S. Sarkar (2012). Gravitino cosmology with a very light neutralino. *Phys. Rev. D*, **85**, p. 065027. doi:10.1103/PhysRevD.85.065027.
- Elmfors, P., K. Enqvist, G. Raffelt, and G. Sigl (1997). Neutrinos with magnetic moment: Depolarization rate in plasma. *Nucl. Phys. B*, **503**, pp. 3–23. doi:10.1016/S0550-3213(97)00382-9.
- Elze, H. T., W. Greiner, and J. Rafelski (1980). The relativistic ideal Fermi gas revisited. *J. Phys. G*, **6**, pp. L149–L153. doi:10.1088/0305-4616/6/9/003.
- Famiano, M. A., A. B. Balantekin, and T. Kajino (2016). Low-lying Resonances and Relativistic Screening in Big Bang Nucleosynthesis. *Phys. Rev. C*, **93**(4), p. 045804. doi:10.1103/PhysRevC.93.045804.
- Fields, B. D. (2011). The primordial lithium problem. *Ann. Rev. Nucl. Part. Sci.*, **61**, pp. 47–68. doi:10.1146/annurev-nucl-102010-130445.

- Formanek, M., S. Evans, J. Rafelski, A. Steinmetz, and C.-T. Yang (2018). Strong fields and neutral particle magnetic moment dynamics. *Plasma Phys. Control. Fusion*, **60**, p. 074006. doi:10.1088/1361-6587/aac06a.
- Formanek, M., C. Grayson, J. Rafelski, and B. Müller (2021). Current-conserving relativistic linear response for collisional plasmas. *Annals Phys.*, **434**, p. 168605. doi:10.1016/j.aop.2021.168605.
- Fornengo, N., C. W. Kim, and J. Song (1997). Finite temperature effects on the neutrino decoupling in the early universe. *Phys. Rev. D*, **56**, pp. 5123–5134. doi:10.1103/PhysRevD.56.5123.
- Freedman, D. Z., D. N. Schramm, and D. L. Tubbs (1977). The Weak Neutral Current and Its Effects in Stellar Collapse. *Ann. Rev. Nucl. Part. Sci.*, **27**, pp. 167–207. doi:10.1146/annurev.ns.27.120177.001123.
- Fromerth, M. J., I. Kuznetsova, L. Labun, J. Letessier, and J. Rafelski (2012). From Quark-Gluon Universe to Neutrino Decoupling: $200 < T < 2\text{MeV}$. *Acta Phys. Polon. B*, **43**(12), pp. 2261–2284. doi:10.5506/APhysPolB.43.2261.
- Fromerth, M. J. and J. Rafelski (2002). Hadronization of the quark Universe. *arXiv astro-ph/0211346*.
- Fukugita, M. and S. Yazaki (1987). Reexamination of Astrophysical and Cosmological Constraints on the Magnetic Moment of Neutrinos. *Phys. Rev. D*, **36**, p. 3817. doi:10.1103/PhysRevD.36.3817.
- Giovannini, M. (2004). The Magnetized universe. *Int. J. Mod. Phys. D*, **13**, pp. 391–502. doi:10.1142/S0218271804004530.
- Giudice, G. F., A. Notari, M. Raidal, A. Riotto, and A. Strumia (2004). Towards a complete theory of thermal leptogenesis in the SM and MSSM. *Nucl. Phys. B*, **685**, pp. 89–149. doi:10.1016/j.nuclphysb.2004.02.019.
- Giunti, C. and C. W. Kim (2007). *Fundamentals of Neutrino Physics and Astrophysics*. Oxford University Press. ISBN 978-0-19-850871-7.
- Giunti, C. and A. Studenikin (2009). Neutrino electromagnetic properties. *Phys. Atom. Nucl.*, **72**, pp. 2089–2125. doi:10.1134/S1063778809120126.
- Grayson, C., C. T. Yang, M. Formanek, and J. Rafelski (2023). Electron–positron plasma in BBN: Damped-dynamic screening. *Annals Phys.*, **458**, p. 169453. doi:10.1016/j.aop.2023.169453.
- Griffiths, D. (2008). *Introduction to elementary particles*. ISBN 978-3-527-40601-2.

- Gruzinov, A. V. (1998). Dynamic screening and thermonuclear reaction rates. *Astrophys. J.*, **496**, p. 503. doi:10.1086/305349.
- Heckler, A. F. (1994). Astrophysical applications of quantum corrections to the equation of state of a plasma. *Phys. Rev. D*, **49**, pp. 611–617. doi:10.1103/PhysRevD.49.611.
- Hwang, E., D. Jang, K. Park, M. Kusakabe, T. Kajino, A. B. Balantekin, T. Maruyama, C.-M. Ryu, and M.-K. Cheoun (2021). Dynamical screening effects on big bang nucleosynthesis. *JCAP*, **11**, p. 017. doi:10.1088/1475-7516/2021/11/017.
- Jedamzik, K. and A. Saveliev (2019). Stringent limit on primordial magnetic fields from the cosmic microwave background radiation. *Physical review letters*, **123**(2), p. 021301. doi:10.1103/PhysRevLett.123.021301.
- Karsch, F., M. T. Mehr, and H. Satz (1988). Color Screening and Deconfinement for Bound States of Heavy Quarks. *Z. Phys. C*, **37**, p. 617. doi:10.1007/BF01549722.
- Kislinger, M. B. and P. D. Morley (1976). Collective Phenomena in Gauge Theories. 1. The Plasmon Effect for Yang-Mills Fields. *Phys. Rev. D*, **13**, p. 2765. doi:10.1103/PhysRevD.13.2765.
- Koch, P., B. Muller, and J. Rafelski (1986). Strangeness in Relativistic Heavy Ion Collisions. *Phys. Rept.*, **142**, pp. 167–262. doi:10.1016/0370-1573(86)90096-7.
- Kolb, E. W., A. D. Linde, and A. Riotto (1996). GUT baryogenesis after preheating. *Phys. Rev. Lett.*, **77**, pp. 4290–4293. doi:10.1103/PhysRevLett.77.4290.
- Kolb, E. W. and M. S. Turner (1990a). *The early universe*. CRC Press.
- Kolb, E. W. and M. S. Turner (1990b). *The Early Universe*, volume 69. ISBN 978-0-201-62674-2. doi:10.1201/9780429492860.
- Kronberg, P. P. (1994a). Extragalactic magnetic fields. *Rept. Prog. Phys.*, **57**, pp. 325–382. doi:10.1088/0034-4885/57/4/001.
- Kronberg, P. P. (1994b). Extragalactic magnetic fields. *Reports on Progress in Physics*, **57**(4), p. 325. doi:10.1088/0034-4885/57/4/001.
- Kuzmin, V. A., V. A. Rubakov, and M. E. Shaposhnikov (1985). On the Anomalous Electroweak Baryon Number Nonconservation in the Early Universe. *Phys. Lett. B*, **155**, p. 36. doi:10.1016/0370-2693(85)91028-7.
- Kuzmin, V. A., V. A. Rubakov, and M. E. Shaposhnikov (1987). Anomalous Electroweak Baryon Number Nonconservation and GUT Mechanism for Baryogenesis. *Phys. Lett. B*, **191**, pp. 171–173. doi:10.1016/0370-2693(87)91340-2.

- Kuznetsova, I., D. Habs, and J. Rafelski (2008). Pion and muon production in e-, e+, gamma plasma. *Phys. Rev. D*, **78**, p. 014027. doi:10.1103/PhysRevD.78.014027.
- Kuznetsova, I., D. Habs, and J. Rafelski (2010). Thermal reaction processes in a relativistic QED plasma drop. *Phys. Rev. D*, **81**, p. 053007. doi:10.1103/PhysRevD.81.053007.
- Kuznetsova, I. and J. Rafelski (2010a). Unstable Hadrons in Hot Hadron Gas in Laboratory and in the Early Universe. *Phys. Rev. C*, **82**, p. 035203. doi:10.1103/PhysRevC.82.035203.
- Kuznetsova, I. and J. Rafelski (2010b). Unstable hadrons in hot hadron gas: In the laboratory and in the early Universe. *Phys. Rev. C*, **82**, p. 035203. doi:10.1103/PhysRevC.82.035203.
- Kuznetsova, I. and J. Rafelski (2012). Electron-Positron Plasma Drop Formed by Ultra-Intense Laser Pulses. *Phys. Rev. D*, **85**, p. 085014. doi:10.1103/PhysRevD.85.085014.
- Letessier, J. and J. Rafelski (2002). *Hadrons and Quark-Gluon Plasma*. Oxford University Press. ISBN 978-1-00-929075-3, 978-0-511-53499-7, 978-1-00-929070-8, 978-1-00-929073-9. doi:10.1017/9781009290753.
- Letessier, J. and J. Rafelski (2008). Hadron production and phase changes in relativistic heavy ion collisions. *Eur. Phys. J. A*, **35**, pp. 221–242. doi:10.1140/epja/i2007-10546-7.
- Lewis, R. R. (1980). Coherent detector for low-energy neutrinos. *Phys. Rev. D*, **21**, pp. 663–668. doi:10.1103/PhysRevD.21.663.
- Mangano, G., G. Miele, S. Pastor, and M. Peloso (2002). A Precision calculation of the effective number of cosmological neutrinos. *Phys. Lett. B*, **534**, pp. 8–16. doi:10.1016/S0370-2693(02)01622-2.
- Mangano, G., G. Miele, S. Pastor, T. Pinto, O. Pisanti, and P. D. Serpico (2005). Relic neutrino decoupling including flavor oscillations. *Nucl. Phys. B*, **729**, pp. 221–234. doi:10.1016/j.nuclphysb.2005.09.041.
- Mangano, G., G. Miele, S. Pastor, T. Pinto, O. Pisanti, and P. D. Serpico (2006). Effects of non-standard neutrino-electron interactions on relic neutrino decoupling. *Nucl. Phys. B*, **756**, pp. 100–116. doi:10.1016/j.nuclphysb.2006.09.002.
- Morgan, J. A. (1981). Cosmological upper limit to neutrino magnetic moments. *Phys. Lett. B*, **102**, pp. 247–250. doi:10.1016/0370-2693(81)90868-6.

- Morrissey, D. E. and M. J. Ramsey-Musolf (2012). Electroweak baryogenesis. *New J. Phys.*, **14**, p. 125003. doi:10.1088/1367-2630/14/12/125003.
- Mukhanov, V. (2005). *Physical Foundations of Cosmology*. Cambridge University Press, Oxford. ISBN 978-0-521-56398-7. doi:10.1017/CBO9780511790553.
- Neronov, A. and I. Vovk (2010). Evidence for strong extragalactic magnetic fields from Fermi observations of TeV blazars. *Science*, **328**(5974), pp. 73–75. doi:10.1126/science.1184192.
- Niculescu, G. (2013). A heuristic approach to the detection of solar neutrinos. *Journal of Physics G: Nuclear and Particle Physics*, **40**, p. 055201. doi:10.1088/0954-3899/40/5/055201.
- Nielsen, H. B. and Y. Takanishi (2001). Baryogenesis via lepton number violation in anti-GUT model. *Phys. Lett. B*, **507**, pp. 241–251. doi:10.1016/S0370-2693(01)00357-4.
- Offler, S., G. Aarts, C. Allton, J. Glesaaen, B. Jäger, S. Kim, M. P. Lombardo, S. M. Ryan, and J.-I. Skullerud (2019). News from bottomonium spectral functions in thermal QCD. *PoS, LATTICE2019*, p. 076. doi:10.22323/1.363.0076.
- Papavassiliou, J., J. Bernabeu, and M. Passera (2006). Neutrino-nuclear coherent scattering and the effective neutrino charge radius. *PoS, HEP2005*, p. 192. doi:10.22323/1.021.0192.
- Patrignani, C. et al. (2016). Review of Particle Physics. *Chin. Phys. C*, **40**(10), p. 100001. doi:10.1088/1674-1137/40/10/100001.
- Pitrou, C., A. Coc, J.-P. Uzan, and E. Vangioni (2018). Precision big bang nucleosynthesis with improved Helium-4 predictions. *Phys. Rept.*, **754**, pp. 1–66. doi:10.1016/j.physrep.2018.04.005.
- Pshirkov, M. S., P. G. Tinyakov, and F. R. Urban (2016). New limits on extragalactic magnetic fields from rotation measures. *Phys. Rev. Lett.*, **116**(19), p. 191302. doi:10.1103/PhysRevLett.116.191302.
- Rafelski, J. (2020). Discovery of Quark-Gluon-Plasma: Strangeness Diaries. *Eur. Phys. J. ST*, **229**(1), pp. 1–140. doi:10.1140/epjst/e2019-900263-x.
- Rafelski, J. and J. Birrell (2014). Traveling Through the Universe: Back in Time to the Quark-Gluon Plasma Era. *J. Phys. Conf. Ser.*, **509**, p. 012014. doi:10.1088/1742-6596/509/1/012014.
- Rafelski, J., J. Birrell, A. Steinmetz, and C. T. Yang (2023). A short survey of matter-antimatter evolution in the primordial universe.

- Rafelski, J., J. Letessier, and G. Torrieri (2001). Strange hadrons and their resonances: A Diagnostic tool of QGP freezeout dynamics. *Phys. Rev. C*, **64**, p. 054907. doi:10.1103/PhysRevC.64.054907. [Erratum: Phys.Rev.C 65, 069902 (2002)].
- Rafelski, J. and C. T. Yang (2021). The muon abundance in the primordial Universe. *Acta Phys. Polon. B*, **52**, p. 277. doi:10.5506/APhysPolB.52.277.
- Rafelski, J. and C. T. Yang (2022). Reactions Governing Strangeness Abundance in Primordial Universe. *EPJ Web Conf.*, **259**, p. 13001. doi:10.1051/epjconf/202225913001.
- Riess, A. G., S. Casertano, W. Yuan, L. Macri, J. Anderson, J. W. MacKenty, J. B. Bowers, K. I. Clubb, A. V. Filippenko, D. O. Jones, et al. (2018a). New parallaxes of galactic cepheids from spatially scanning the hubble space telescope: Implications for the hubble constant. *The Astrophysical Journal*, **855**(2), p. 136.
- Riess, A. G. et al. (2018b). Milky Way Cepheid Standards for Measuring Cosmic Distances and Application to Gaia DR2: Implications for the Hubble Constant. *Astrophys. J.*, **861**(2), p. 126. doi:10.3847/1538-4357/aac82e.
- Riotto, A. and M. Trodden (1999). Recent progress in baryogenesis. *Ann. Rev. Nucl. Part. Sci.*, **49**, pp. 35–75. doi:10.1146/annurev.nucl.49.1.35.
- Sajjad Athar, M., A. Fatima, and S. K. Singh (2023). Neutrinos and their interactions with matter. *Prog. Part. Nucl. Phys.*, **129**, p. 104019. doi:10.1016/j.ppnp.2022.104019.
- Sakharov, A. D. (1967). Violation of CP Invariance, C asymmetry, and baryon asymmetry of the universe. *Pisma Zh. Eksp. Teor. Fiz.*, **5**, pp. 32–35. doi:10.1070/PU1991v034n05ABEH002497.
- Sakharov, A. D. (1990). Baryon asymmetry of the universe. pp. 65–80. doi:10.1070/PU1991v034n05ABEH002504.
- Salpeter, E. E. (1954). Electron screening and thermonuclear reactions. *Austral. J. Phys.*, **7**, pp. 373–388. doi:10.1071/PH540373.
- Salpeter, E. E. and H. M. van Horn (1969). Nuclear Reaction Rates at High Densities. *ApJ*, **155**, p. 183. doi:10.1086/149858.
- Schroedter, M., R. L. Thews, and J. Rafelski (2000). B_c meson production in nuclear collisions at RHIC. *Phys. Rev. C*, **62**, p. 024905. doi:10.1103/PhysRevC.62.024905.

- Sehgal, L. M. and M. Wanninger (1986). Atomic Effects in Coherent Neutrino Scattering. *Phys. Lett. B*, **171**, pp. 107–112. doi:10.1016/0370-2693(86)91008-7.
- Smith, P. F. (1984). Coherent neutrino scattering—Relativistic and nonrelativistic. *II Nuovo Cimento A (1965-1970)*, **83**, pp. 263–274. doi:10.1007/BF02902601.
- Steinmetz, A., C. T. Yang, and J. Rafelski (2023a). Antimatter origin of cosmic magnetism: A first look. (*in preparation*).
- Steinmetz, A., C. T. Yang, and J. Rafelski (2023b). Matter-antimatter origin of cosmic magnetism.
- Tanabashi, M. et al. (2018). Review of Particle Physics. *Phys. Rev. D*, **98**(3), p. 030001. doi:10.1103/PhysRevD.98.030001.
- Taylor, A. M., I. Vovk, and A. Neronov (2011). Extragalactic magnetic fields constraints from simultaneous GeV–TeV observations of blazars. *Astronomy & Astrophysics*, **529**, p. A144. doi:10.1051/0004-6361/201116441.
- Tully, A. M. (2019). *Doubly charmed B decays with the LHCb experiment*. Ph.D. thesis, Cambridge U. doi:10.17863/CAM.44796.
- Vazza, F. et al. (2021). Magnetogenesis and the Cosmic Web: A Joint Challenge for Radio Observations and Numerical Simulations. *Galaxies*, **9**(4), p. 109. doi:10.3390/galaxies9040109.
- Vernstrom, T., G. Heald, F. Vazza, T. J. Galvin, J. L. West, N. Locatelli, N. Fornengo, and E. Pinetti (2021). Discovery of magnetic fields along stacked cosmic filaments as revealed by radio and X-ray emission. *Monthly Notices of the Royal Astronomical Society*, **505**(3), pp. 4178–4196. doi:10.1093/mnras/stab1301.
- Vogel, P. and J. Engel (1989). Neutrino Electromagnetic Form-Factors. *Phys. Rev. D*, **39**, p. 3378. doi:10.1103/PhysRevD.39.3378.
- Wang, B., C. A. Bertulani, and A. B. Balantekin (2011). Electron screening and its effects on Big-Bang nucleosynthesis. *Phys. Rev. C*, **83**, p. 018801. doi:10.1103/PhysRevC.83.018801.
- Weber, J. (1988). Apparent observation of abnormally large coherent scattering cross sections using keV and MeV range antineutrinos, and solar neutrinos. *Phys. Rev. D*, **38**, pp. 32–39. doi:10.1103/PhysRevD.38.32.
- Widrow, L. M., D. Ryu, D. R. G. Schleicher, K. Subramanian, C. G. Tsagas, and R. A. Treumann (2012). The First Magnetic Fields. *Space Sci. Rev.*, **166**, pp. 37–70. doi:10.1007/s11214-011-9833-5.

- Wolfenstein, L. (1978). Neutrino oscillations in matter. *Phys. Rev. D*, **17**, pp. 2369–2374. doi:10.1103/PhysRevD.17.2369.
- Workman, R. L. et al. (2022). Review of Particle Physics. *PTEP*, **2022**, p. 083C01. doi:10.1093/ptep/ptac097.
- Yang, C. T., J. Birrell, and J. Rafelski (2018a). Lepton Number and Expansion of the Universe.
- Yang, C. T., J. Birrell, and J. Rafelski (2018b). Temperature Dependence of the Neutron Lifespan.
- Yang, C. T. and J. Rafelski (2020). Possibility of bottom-catalyzed matter genesis near to primordial QGP hadronization.
- Yang, C. T. and J. Rafelski (2022). Cosmological strangeness abundance. *Phys. Lett. B*, **827**, p. 136944. doi:10.1016/j.physletb.2022.136944.